Prediction of emissions from combustion systems using 0D and 1D reacting flow models

Technische Universiteit Delft

TU Delft

Prediction of emissions from combustion systems using 0D and 1D reacting flow models

Chemical Reactor Network modeling

B. Rosati

TU Delft

Prediction of emissions from combustion systems using 0D and 1D reacting flow models

Chemical Reactor Network modeling

by

B. Rosati

to obtain the degree of Master of Science
at the Delft University of Technology,
to be defended publicly on Monday December 14, 2015 at 10:00 AM.

Student number:	4259343	
Project duration:	November 15, 2014 – December 14, 2015	
Thesis committee:	Prof. dr. D.J.E.M. Roekaerts,	TU Delft, supervisor
	Dr. A. Gangoli Rao,	TU Delft, co-supervisor
	Dr. A. Bhat,	Honeywell, co-supervisor
	Dr. H. B. Eral,	TU Delft

Faculty of Mechanical, Maritime and Materials Engineering (3mE).
Process & Energy Department. Delft University of Technology

TU Delft Delft University of Technology

Abstract

Emission prediction is a complex problem involving the coupling between the flow field and chemistry. Most of the time CFD is the preferred modeling approach, yielding predictions with varying degrees of accuracy. But because of a high computational cost, CFD investigations are often limited to the use of reduced chemical mechanisms. In this work the specific features of chemical reactor networks are exploited to build a fast and reliable emission estimator. The main advantage of this modeling approach is a much lower computational cost than CFD, hence offering the potential for relatively fast predictions while allowing the use of detailed chemistry.

This methodology has been applied to three different combustion systems, with mixed results. It may not be the most suitable modeling technique to obtain emissions from a lifted jet flame, but a successful estimator has been designed for flameless furnaces. It is based solely on analytical sub–models, giving it the potential to predict the emissions from any type of flameless furnace installation. For three different experimental setups, the correct trends were reproduced as well as the right order of magnitude for NO_x and CO emissions, if not within experimental measurements uncertainty. Finally the emissions from a lean-premixed gas turbine combustor burning cryogenic fuel have been successfully modeled and this investigation has brought out the major sensitivities of this system.

Lastly, despite some promising results, several developments have been suggested to improve the accuracy and stability of the flameless furnace estimator. The combustor estimator, for one, can be used as basis to investigate the behavior of the more comprehensive hybrid combustion system it has originally been designed for: the dual combustion chamber of the AHEAD hybrid engine (Advanced Hybrid Engines for Aircraft Development).

Keywords: Emissions, Reactor networks, Flameless combustion, Strong–Jet / Weak–Jet, Lean-premixed combustion.

Contents

List of Figures

List of Tables

1

Introduction

1.1. Energy & Environment

Along with the development of the modern society we live in, the use of combustion has democratized following a rapid industrialization and improvements in the standard of living. Today's very energy intensive society is burning more and more fuel, both domestically and industrially, for many purposes: heating, cooking, lighting, transport are a few examples. On a global scale energy consumption has been rising [1], driven by an always increasing world population and the quick development of heavily populated countries (China, India). This phenomenon led inevitably to increased emissions of pollutants into the atmosphere : carbon dioxide and monoxide (CO_2 and CO), nitrogen oxides (NO_x), sulfur oxides (SO_x) or other gases of anthropogenic origin contributing to global warming or ozone layer depletion (CFCs, PFCs, HFCs...).

Fortunately for more than two decades energy and environmental issues have become of prime concern. The Montreal protocol designed to protect the ozone layer entered into force in 1989. The 1992 UN Conference on Environment and Development — a.k.a. the Rio Summit — can be considered another major landmark in the growing environmental concern. Its objective was to establish international initiatives for the preservation of the global environment [2]. This conference resulted in the adoption in 1997 of the Kyoto protocol for the reduction of greenhouse gases (GHGs) emissions, acknowledging anthropogenic global warming. The most important and well known GHG is probably carbon dioxide which accounts for almost 70% of global GHG emissions [3]. The mitigation of combustion-generated CO_2 is thus vital, but other GHGs are just as dangerous despite representing only a fraction of the total GHG emissions: methane (CH_4), nitrous oxide (N_2O)... [4]. The first period of commitment of the signatory nations under the Kyoto protocol was from 2008 to 2012.

In order to reverse the observed trend on the environment, but also pushed by the upcoming inevitable shortage in fossil fuels, an increasing interest has been developed in improving combustion technologies. Historically the first focus was on increasing the energy efficiency after the energy crisis in the 1970s [5]. New designs appeared including flue gas heat recycling using recuperating or regenerating techniques. Such systems decreased significantly fuel consumption and as a byproduct CO_2 emissions as well. However other pollutants like NO_x and SO_x hadn't received yet the attention the popular carbon dioxide did, and with the appearance of new regulatory standards accounting for it, it turned out these new technologies emitted particularly high levels of NO_x. The growing awareness of nitrogen oxides impact on the environment led to more and more stringent environmental laws and thus stimulated the research for new, low-NO_x combustion technologies. To answer both challenges, various combustion methods have been developed since the 1980s combining high efficiency and low emissions : re-burning, oxy-combustion, staged combustion e.g. In the 1990s, a new revolutionary technique offering great potential was discovered : flameless combustion. It combines the advantages of high energy efficiency from flue gas recirculation to very low NO_x emissions. Finally the fields of alternative fuels and hybrid combustion technologies have also been investigated.

1.2. Design & Modeling

The current interest for low-emissions combustion systems brings the interrogation on which tools are available to obtain the potential emissions of a new system being designed? Prediction of emissions from combustion systems is not a trivial subject as it involves greatly the coupling between flow field and chemistry. Different models have been developed, with different degrees of accuracy, but in most cases CFD has been the preferred modeling approach : turbulence models are used for flow turbulence closure and turbulence – combustion interaction models are used for closure of the reaction source terms. The turbulent combustion models often lead to high computational cost so reduced chemical mechanism have to be used to keep it ”reasonable”. Despite yielding predictions of rather good quality, this approach has several weaknesses. First one can wonder what are the inaccuracies introduced in the predictions by the turbulence and the turbulent combustion models. Second, the same question arises concerning the use of reduced chemistry. And finally, the simulation time necessary to obtain these predictions is more of the order of day(s) than hours. There is a clear need for fast and reliable estimates of emissions from combustion systems.

An alternative modeling method is to use Chemical Reactor Network modeling (CRN) for which the modeling philosophy is different than CFD. Computational Fluid Dynamics requires fine spatial discretization, that combined with the closure models and the fluid dynamics equations prevents the use of detailed chemistry (in case of a reacting flow) for computational cost reasons. CRN modeling is the inverse : the direct coupling between the flow field and the chemistry is described using 0D and 1D reactors. The type of flow field in a local domain is assumed known (e.g. perfectly mixed) and the characteristics of the overall system are obtained by creating a network of the submodels for the local flow domains. Mass and energy flows link the reactors, and their values are obtained from any available information on the flow field : previous CFD modeling, experiments, correlations... The resulting discretization of the flow field is rougher than for any CFD study, but the main advantage of such networks (in terms of computational cost) is that they allow the use of a complete and detailed chemistry models. Depending on the fuel used, a complete system of reactions can vary from 20 to thousands of reactions. On the other hand, the use of previous CFD or costly experiments to calibrate carefully a CRN balances the pros. Furthermore some tools to generate a reactor network from a CFD–obtained flow field exist, but manually creating a reactor network without this kind of basis is still very empirical. In short, both modeling approaches can complement one another, but a nicely calibrated reactor network offers the possibility of fast and reliable emission predictions with the potential to vary a lot of parameters.

1.3. Thesis objectives

The main objective of this work is to make use of the CRN modeling approach to build a fast and reliable emission estimator. This fast estimator will also be able to vary numerous parameters to allow for sensitivity analysis and ”simplification limit” investigation: to what extent can the combustion system be simplified in the reactor network while keeping consistent results with CFD and experiments?

To achieve this, CRN modeling is applied on three different systems to predict their emissions:

- a lifted jet flame ;
- a furnace with multiple regenerative flameless combustion burners : the 300kW furnace of the Process & Energy Department at TU Delft (3mE faculty) ;
- the dual combustion chamber of the AHEAD engine, a european project [6] in which the Flight Performance & Propulsion Department of TU Delft (aerospace faculty) is involved.

To generate and simulate the reactor networks, the open-source software Cantera [7] is used. Cantera is a suite of object-oriented software tools for problems involving chemical kinetics, thermodynamics and transport processes. It is a C++ based code, with interfaces for C++, Matlab® and Python. The Python interface is used.

1.4. Thesis outline

In the following chapter, the results of literature studies on the main physical phenomena involved are presented : emissions, chemical mechanisms , flameless combustion and jet modeling. Chapter 3 deals with the modeling of the first combustion system, the lifted jet flame, while the two other systems are discussed in Chapter 4 and 5. More precisely, in Chapter 5 only the modeling and results of the first chamber of the dual combustion system are presented. Finally, Chapter 6 concludes on the work.

2

Literature : scientific background

2.1. Emissions

In the scope of this master thesis work, the emission predictions will focus on two compounds : carbon monoxide and nitrogen oxides.

2.1.1. Carbon monoxide (CO)

Impact on health and environment

Carbon monoxide is a toxic gas emitted by combustion processes. Its colorless and odorless characteristics make it extremely dangerous since it is well known CO can have severe health effects on humans. The toxicity of carbon monoxide lies in the fact it prevents the human body from using oxygen: it forms a strong bond with the hemoglobin molecule, forming carboxyhemoglobin ($COHb$), and thus taking the place of oxygen molecules [8][9]. This inhibits oxygenation of organs and tissues. Additionally, the presence of $COHb$ also alters the liberation of oxygen from its hemoglobin carrying molecule, reducing even further the oxygenation of the body. Eventually, at high enough levels, CO exposure causes death.

Unlike CO_2, carbon monoxide is not known as a direct contributor to Earth's climate. However it still plays an indirect role in climate change. CO is only a weak direct greenhouse gas, but it impacts the concentration of major greenhouse gases [10]: it readily reacts with OH forming CO_2 which at the same time increases the concentration of CH_4 because the removal of methane from the atmosphere commonly happens through its reaction with OH. Finally, CO can also lead to the production of tropospheric ozone (O_3) interacting with NO_x.

Formation process

The complete combustion of hydrocarbons produces carbon dioxide and water. Carbon monoxide emissions are a result of incomplete combustion. Hydrocarbon oxidation can simplistically be characterized by a two-step global mechanism : the first step consists in rapid oxidation into CO and H_2O, followed by the final oxidation of CO into CO_2 [11] :

$$C_xH_y + \left(\frac{x}{2} + \frac{y}{4}\right)O_2 \rightarrow xCO + \frac{y}{2}H_2O \tag{2.1}$$

$$CO + \frac{1}{2}O_2 \rightarrow CO_2 \tag{2.2}$$

This representation is however not sufficient to provide an understanding of the factors influencing the complete oxidation of CO to CO_2. It is well known that this step is slow, but the presence of even small amounts of hydrogen–containing species can tremendously increase this oxidation rate. In most cases, water is the predominant hydrogen–containing compound and the final oxidation of CO can be described by these four steps [12]:

$$CO + O_2 \rightarrow CO_2 + O \tag{2.3}$$

$$O + H_2O \rightarrow OH + OH \tag{2.4}$$

$$CO + OH \rightarrow CO_2 + H \tag{2.5}$$

$$H + O_2 \rightarrow OH + O \tag{2.6}$$

Reaction (2.3) does not contribute significantly to the formation of CO_2 and rather serves as chain initiating step. The predominant reaction leading to CO_2 (rate–controlling reaction) is equation (2.5), which also serves as chain propagating step. It produces H radicals that react with oxygen in (2.6) to produce OH and O radicals, which in turn feed back into the oxidation step (2.5) and reaction (2.4). Equation (2.5) is the most important step in this mechanism and a detailed kinetic analysis can be found in [11]. It highlights two major influences on CO oxidation : an insufficient amount of oxygen (fuel rich conditions) or an insufficient residence time at high temperatures tend to produce more CO. For this reason, it can happen that NO_x control strategies lowering peak flame temperatures increase CO emissions. Finally, at very high temperatures ($> 2000K$), dissociation of carbon dioxide (the reverse reaction of (2.2)) can also participate in the formation of CO.

2.1.2. Nitrogen oxides (NO_x)

In addition to carbon monoxide and dioxide, combustion systems can produce nitrogen oxides through the reaction of molecular nitrogen contained either in the fuel or in the air. The nitrogen oxides family regroups a variety of compounds [13] among which the most relevant to combustion systems are: nitric oxide (NO), nitric dioxide (NO_2) and nitrous oxide (N_2O) also known as "laughing gas". These are also the main nitrogen oxides found in the atmosphere. The first two compounds are commonly grouped together and referred to as NO_x while N_2O is not included in the definition since it is in majority being produced naturally [14]. Additionally, fractions higher than 90% of the NO_x in the exhaust of a combustion system is NO [14]. The oxidation of NO to NO_2 occurs later in low–temperature regions [12].

Impact on health and environment

Nitrogen oxides cause a wide variety of health and environmental issues [13][15]. NO_x reacts with other substances in the air to form nitric acid (HNO_3), partly responsible for acid rain. NO_x is also responsible for the undesirable formation of photochemical smog (tropospheric ozone, ground–level ozone) when it reacts with volatile organic compounds in the presence of sunlight. Smog impairs visibility and causes respiratory problems. N_2O is a known and powerful greenhouse gas, which also contributes to the depletion of stratospheric ozone.

NO_x formation processes

Because of its role in combustion and the subsequent impacts, the chemical kinetics of NO_x formation have received detailed attention [16]. Different pathways have been identified and their relative importance varies depending on the combustion conditions.

Thermal NO or Zel'dovich mechanism: This pathway consists in the oxidation of atmospheric nitrogen via the following mechanism known as the extended Zel'dovich mechanism [17]

$$N_2 + O \underset{k_{1,r}}{\overset{k_{1,f}}{\rightleftharpoons}} NO + N \tag{2.7}$$

$$N + O_2 \underset{k_{2,r}}{\overset{k_{2,f}}{\rightleftharpoons}} NO + O \tag{2.8}$$

$$N + OH \underset{k_{3,r}}{\overset{k_{3,f}}{\rightleftharpoons}} NO + H \tag{2.9}$$

The values of the rate constants can be found in [18][11]. The rate limiting reaction in the formation of NO is the forward (2.7) because of its high activation energy. This route has then a high temperature dependence, hence the name. As a basic rule of thumb, it is considered that this pathway becomes

active and significant at temperatures above $1800K$. Under simplifying assumptions an expression for the global rate of NO formation along this pathway can be derived [12]: it confirms a high dependence on temperature (independtly of fuel type) as well as highlights an increasing rate of formation with an increasing oxygen concentration. This explains the benefits of flameless combustion as low–NO_x combustion systems.

Prompt NO or Fenimore mechanism: This route is intimately linked to the combustion chemistry of hydrocarbons and depends on local combustion conditions rather than on temperature. Fenimore [19] discovered that some NO was rapidly produced in the flame zone of laminar premixed flames long before the characteristic time of the thermal NO. This rapid formation of NO was termed ”prompt”. Because prompt NO is formed in the presence of CH radicals (among others), its formation is favored in fuel rich zones and its importance is significant at low temperatures and small residence times (before the thermal pathway activates). The actual general scheme involves a complex sequence of reactions coupled with fuel chemistry, but ignoring the chemistry leading to CH radicals the Fenimore mechanism can simplistically be written as follows [12]:

$$CH + N_2 \rightleftharpoons HCN + N \tag{2.10}$$

$$C + N_2 \rightleftharpoons CN + N \tag{2.11}$$

where reaction (2.10) is the rate limiting step. For equivalence ratios less than about 1.2, the conversion of hydrogen cyanide HCN into NO follows this sequence:

$$HCN + O \rightleftharpoons NCO + H \tag{2.12}$$

$$NCO + H \rightleftharpoons NH + CO \tag{2.13}$$

$$NH + H \rightleftharpoons N + H2 \tag{2.14}$$

$$N + OH \rightleftharpoons NO + H \tag{2.15}$$

Fuel NO: Some fuels contain nitrogen in their molecular structure (e.g. coal can contain bound nitrogen up to 2% in mass). The thermal decomposition of the nitrogen-bound compounds of the fuel in the reaction zone leads to the creation of radicals, mainly hydrogen cyanide HCN and ammonia NH_3 [12][18][20]. These radicals are in turn subject to a double competitive reaction path : they are oxidized into NO in the presence of oxygen, but they can also contribute to reduce NO into N_2.

N_2O–Intermediate: As its name indicates, this route forms NO from molecular N_2 via nitrous oxide. The favorable conditions under which this pathway is significant are high pressures, lean mixture and low temperatures [12][20]. These characteristics make this route particularly important for the recent gas turbine designs, but also for systems using flameless combustion [18]. Malte and Pratt [21] proposed first a mechanism for the N_2O–intermadiate route which under its simplest form can be written:

$$N_2 + O + M \rightleftharpoons N_2O + M \tag{2.16}$$

$$N_2O + O \rightleftharpoons NO + NO \tag{2.17}$$

NNH pathway: This route introduced by Bozzelli and Dean [22] is significant at low temperatures, and particularly for hydrogen–enriched or hydrogen flames. It is also significant in the presence of abundant O radicals, e.g. in lean–premixed flames. NO formation through the NNH pathway occurs mostly through:

$$NNH + O \rightleftharpoons NO + NH \tag{2.18}$$

$$NNH + O \rightleftharpoons N_2O + H \tag{2.19}$$

with subsequent oxidation of NH and N_2O in the presence of O and H radicals. NNH is formed previously via the equilibrium:

$$N_2 + H \rightleftharpoons NNH \tag{2.20}$$

obviously favored when hydrogen is easily available. Additional experimental evidence of this mechanism has been reported in [23] and [24].

NO_x **reburning:** In fuel rich conditions NO can be reduced by CH_i radicals to form species like HCN and other products (O, OH, H_2O) which in turn can form NO or N_2 [18][20].

NO **oxidation into** NO_2**:** In the atmosphere, NO oxidizes into NO_2. Usually most of the NO_x emissions from combustion systems are NO (≈90%) but NO_2 is still present in the exhaust. For some combustion systems (gas turbines e.g.) NO_2 can even represent a more significant amount of the NO_x emissions, up to 50% [11]. The elementary reactions responsible for NO_2 formation prior to exhaust are the following [12]:

$$NO + HO_2 \rightleftharpoons NO_2 + OH \quad (formation) \tag{2.21}$$

$$NO_2 + H \rightleftharpoons NO + OH \quad (destruction) \tag{2.22}$$

$$NO_2 + O \rightleftharpoons NO + O_2 \quad (destruction) \tag{2.23}$$

where the HO_2 radical is formed by the three–body reaction:

$$H + O_2 + M \rightleftharpoons HO_2 + M \tag{2.24}$$

The HO_2 radicals are formed in relatively low temperature regions. NO_2 destruction reactions (2.22) and (2.23) are active at high temperatures. This explains the formation of NO_2 in post–flame regions.

NO_x control strategies

The thorough understanding of NO_x formation and destruction processes gained over the years led to the design of low–emissions combustion systems. One can now understand why the attempts to reach higher fuel efficiency by preheating the combustion air before injection led to high NO_x emissions: it caused increased flame temperatures which activate the thermal NO pathway. An overview of NO_x control methods is given by Szegö [8]: he chose to classify them into combustion modification and post–combustion techniques.

Common examples of the first category may be air staging, fuel staging, fuel reburning, flue gas recirculation, lean–premixed combustion or flameless combustion. All these techniques ultimately lead to a decreased peak temperature, therefore preventing thermal NO_x formation. Some of the drawbacks are the appearance of flame stability problems and incomplete combustion products like carbon monoxide. An alternative method in this first category is oxy–combustion : the idea is to prevent NO_x formation by reducing the molecular nitrogen concentration. Theoretically, operating with pure O_2 would eliminate all nitrogen from the process and consequently prevent any NO_x formation. However there are practical problems to this pure oxygen combustion: the temperature levels reached are higher than with air which can become an issue in terms of thermal resistance of the combustor materials, it is also hard to prevent air (and thus N_2) infiltration into the system and economically, pure oxygen is very expensive making this technique less attractive. It is also obvious that using nitrogen–containing fuel in such systems defeats their purpose. Post–combustion treatment methods also exist, the most common being NO removal via Selective Non–Catalytic Reduction (SNCR) and Selective Catalytic Reduction (SCR).

All these techniques can be combined to achieve further NO_x abatement. It is not uncommon to combine flue gas recirculation and staging methods in furnaces and boilers, but a perfect example is the dual combustion chamber of the AHEAD engine project (see chapter 5): a first lean–premixed combustion chamber using Liquefied Natural Gas (LNG) or Liquefied H_2 (LH2) as a fuel (cryogenic fuel), followed by a reheating under flameless conditions using kerosene or biofuel as fuel.

2.1.3. Quantification of emissions

In order to allow comparisons between different systems or between different conditions on the same system, the ”raw” predictions or measurements are corrected.

From wet to dry basis

To convert the mole fraction (concentration) of component i from wet to dry basis, the following formula is used:

$$X_{i,dry} = \frac{X_{i,wet}}{1 - X_{H_2O,wet}} \tag{2.25}$$

A more complicated way to express the same conversion can be found in [12], based on reactants composition rather than products concentration.

Correction to a reference O_2 content

Concentrations corrected to a particular level of oxygen in the product stream are used in practice to remove the effect of various degrees of dilution, so that true comparisons of emission levels can be made [12].

Assuming air is composed of 21% O_2 and 79% N_2 (in volume), the stoichiometric or lean combustion of one mole of fuel can be written as:

$$C_xH_y + aO_2 + 3.76aN_2 \rightarrow xCO_2 + \frac{y}{2}H_2O + bO_2 + 3.76aN_2 + trace\ species \tag{2.26}$$

To correct a measured concentration or to convert from one O_2 level to another the following equation applies [12]:

$$X_{i,O_2\ level\,2} = X_{i,O_2\ level\,1}\frac{N_{mix,O_2\ level\,1}}{N_{mix,O_2\ level\,2}} \tag{2.27}$$

where for wet concentrations,

$$N_{mix,wet} = 4.76\left[\frac{x + \left(1 + X_{O_2,wet}\right)y/4}{1 - 4.76X_{O_2,wet}}\right] + \frac{y}{4} \tag{2.28}$$

and for dry concentrations,

$$N_{mix,dry} = 4.76\left[\frac{x + \left(1 - X_{O_2,dry}\right)y/4}{1 - 4.76X_{O_2,dry}}\right] - \frac{y}{4} \tag{2.29}$$

Emission Index

Emission levels are expressed in many different ways : parts–per–million (by volume) is the most usual but in some specific fields of industry, rather unusual units can be used. Another common way of reporting emissions is the so–called emission index. The emission index (EI) for species i is the ratio of the mass of species i to the mass of fuel burned by the process [12]:

$$EI_i = \frac{m_{i,emitted}}{m_{fuel,burned}} \tag{2.30}$$

In terms of unit, the EI is dimensionless, but to avoid working with very small numbers units like g/kg are commonly used. The EI is particularly useful because it expresses the amount of pollutant formed per mass of consumed fuel, regardless of any dilution of the product stream or efficiency of the combustion process. It can be interpreted as a measure of the efficiency of a specific combustion process in producing a specific pollutant.

For some of the combustion systems that will be modeled, the EI of NO_x is used ($EINO_x$). Following the definition, it represents the mass of NO_x produced per kg of fuel but with a subtlety: because eventually NO is oxidized into NO_2 in the atmosphere, the fraction of NO in the exhaust stream is considered as NO_2 mass–wise. For our applications the following formula is used :

$$EINO_x = \frac{\left(X_{NO,exhaust} + X_{NO_2,exhaust}\right)\frac{MW_{NO_2}}{MW_{exhaust}}\dot{m}_{exhaust}}{\dot{m}_{fuel}} \times 1000 \quad [g/kg] \tag{2.31}$$

where MW_i is the molar mass of species i or of composition i.

2.2. Chemical mechanisms

CRN modeling and chemical mechanisms are intertwined concepts: the former would not be possible without the latter. For instance with Cantera, every simulation involves one or more phases of matter which have to be defined prior to simulation. Phases are defined using models implementing their thermodynamic properties, transport properties or the reaction rates in the phase(s) present. The chemical elements and species involved in a (non–)reacting phase must also be defined, and interface properties between phases might also be needed. All these sub–models are gathered into an input file

(.cti file for Cantera) that uses a specific syntax. The submodel containing the chemical kinetics data and the reactions that can occur in the phase is a chemical mechanism. The Cantera documentation [7] includes a guide to its input file format: how are the thermodynamic variables defined and computed, how to specify elements and species or how to implement a specific set of reactions between those species.

However generating a chemical mechanism is no easy task and its own research field has been developed. This resulted in the publication of numerous chemical mechanisms, more or less detailed, sometimes designed for a specific need, other times designed for a more general purpose. Popular softwares used for CRN modeling (Cantera, CHEMKIN [25]) include default chemical mechanisms (more correctly default input files built around some chemical mechanisms) in their libraries published by various organizations or research groups [26]. Two of them will be used in the following work and are briefly presented below.

2.2.1. GRI-Mech 3.0

GRI–Mech 3.0 (or GRI–3.0) is the most recent chemical mechanism developed by the Gas Research Institute [27] to model natural gas combustion, including full NO_x chemistry (thermal, prompt, N_2O–intermediate, reburn...). It is a compilation of 325 reactions involving 53 species, including hydrocarbons not higher than C_3. A particular feature of GRI–Mech 3.0 is that it has been optimized as a whole towards targets related to methane and natural gas combustion. While it includes reactions involving other hydrocarbons constituents of natural gas (ethane, propane...), the optimization targets did not include any data related to those fuels [28]. Consequently it is recommended that GRI–Mech 3.0 should not be used to model combustion of pure fuels like methanol, propane, ethylene and acetylene even though those species are present in the GRI–Mech 3.0 species list. The conditions for which GRI–Mech 3.0 has been optimized are roughly:

- $1000\,K$ to $2500\,K$;
- $10\,Torr$ to $10\,atm$;
- equivalence ratios from 0.1 to 5 for premixed systems.

The GRI–3.0 mechanism is considered one of the best when it comes to CH_4/NO_x chemistry for natural gas combustion and it is widely used. It will be used in this work for the emissions modeling of the lifted jet flame system and of the flameless furnace.

2.2.2. $C2\_NO_x$ Mechanism

The $C2\_NO_x$ mechanism was developed by Reaction Design. It describes the oxidation of hydrogen, methane and ethane over a broad range of temperature and pressure and includes the same full NO_x chemistry as GRI–3.0 with additions for low and intermediate temperature ranges as well as pressure–dependent NO_x–hydrocarbon reactions. It includes 99 chemical species involved in 693 elementary reactions [29]. Of particular interest for the following study is the pressure dependence of the mechanism and its capability to model hydrogen oxidation based on recent kinetic studies (O'Conaire mechanism): it will be used in the emissions estimator for the cryo–combustion chamber of the AHEAD engine project.

2.3. Flameless combustion

To meet the challenges of a rising fuel consumption while the reserves are limited and of increased emissions into the environment, new combustion strategies have been investigated, beyond what may be called "conventional combustion". Some of them have already been mentioned, including one particular technique that will be explained with detail in this section : flameless combustion.

2.3.1. One technology, different names

An effective method to improve fuel efficiency is to preheat the reactants (or only the oxidizer stream) without mixing reactants and products streams, using heat recovery methods. It is also an effective method for the combustion of low–calorific fuels [2]. This process has originally been named "Excess Enthalpy Combustion" [30] and later more generally "Heat Recirculating Combustion" [31]. The maximum temperature and overall temperature rise throughout the process in heat–recirculating combustion

is determined by the amount of recycled heat. The main drawback of such systems is the increased NO_x emissions due to the higher temperature levels. In the 1990's it has been discovered that significant reductions in NO_x are possible even with high levels of air preheat: if the reactants are diluted with the products prior to combustion, in a high enough temperature environment. During this discovery period, several names were given to this process by different research groups across the world : FLOX® (for "Flameless Oxidation") in Germany [32][33], HiTAC (for "High Temperature Air Combustion") in Japan [2], MILD Combustion (for "Moderate and Intense Low–oxygen Dilution Combustion") in Italy [34]. Other names for the same technology can also be found: "Direct Fuel Injection", "Colorless (Distributed) Combustion" [5], "Diluted Combustion" [35]. All these terminologies refer to either the burner design or a characteristic of the process. It also means that there is no rigorous framework for the definition of this combustion process, and there is no common agreement on which terminology to adopt to this day. Following previous work from TU Delft [5][36], the term used in this work is "Flameless Combustion" in reference to the distinctive property of this combustion technique.

2.3.2. Theory and characteristics

The flameless combustion strategy is based on Exhaust Gas Recirculation (EGR) pushed to the extreme: the fuel and oxidizer streams are highly diluted with recirculating flue gas before they mix which results in a significant reduction in the local oxygen concentration by increasing the inert content (N_2, CO_2, H_2O) of the combustion mixture. This in turn slows the combustion kinetics which participates to the expansion of the reaction zone compared to conventional combustion. Because the heat is released progressively to a larger volume, it creates a more uniform temperature distribution with reduced peak temperatures over the reaction zone: such characteristics can drastically reduce NO_x emissions by limiting the thermal NO production.

In practice, exhaust gas recirculation and the dilution of the reactants streams (a process also called "inertization" or "vitiation") can be achieved by separately injecting the fuel and combustion air at high velocities in a hot and confined environment: the comburant jets can entrain large quantities of the surrounding flue gas (hot and rich in inerts) before they mix. A schematic of this process can be seen in figure 2.1. However, this high–momentum injection creates high strain rates in the jets and thus flame extinction could be expected [5][36]. Also, because the heat release is proportional to the local amount of oxygen available locally [37], the chemical process may not self–sustain. For these reasons, to ensure stable combustion in flameless mode, the temperature of the surroundings in which the fuel and oxidizer are injected should be higher than the self–ignition temperature of the fuel/air mixture. Consequently, after sufficicent inertization the comburant streams contain the thermal energy needed for the mixture to spontaneously ignite. To help overcome this flame stability issue, flue gas heat recuperation or regeneration can be applied in parallel to EGR in order to preheat the air/oxidizer stream. For instance the multiburner flameless furnace of TU Delft is equipped with regenerative burners. This also has the desirable consequence to increase the thermal efficiency and thus decrease the overall CO_2 emissions. However, air preheating is not a necessary condition for flameless combustion [38].

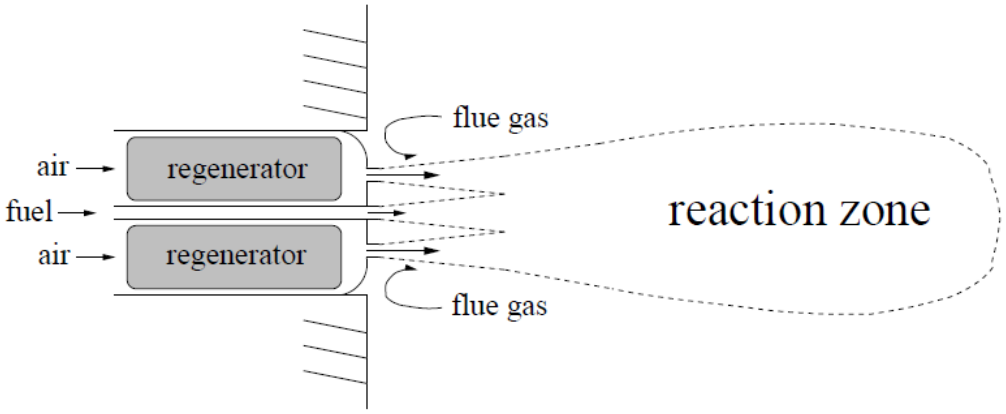

Figure 2.1: Schematic representation of the flameless combustion technique principle (from [5])

This particularity for the reactants injection is an extremely important feature of flameless combustion: its stability domain is strongly related to the mixing of fresh reactants with flue gases. Either mixing of the reactants has to be retarded until they are sufficiently diluted, or the temperature of the reactants has to remain below their auto–ignition temperature until enough dilution has occured [39]. The distance between fuel and oxidizer injections and the relative injection momentum ratio of both jets are intimately linked because they govern the distance at which both jets mix and hence their respective dilution with hot products.

Exhaust gas recirculation is the most important feature of the flameless combustion process as it affects greatly the reaction zone. The resulting area and volume of the reaction zone is substantially larger than that of conventional combustion, which can be characterized by their flame front [33][40]. Under flameless conditions, combustion reactions are distributed in a large volume instead of being concentrated into a thin, convoluted and stretched layer: there is no flame front. EGR also depresses the formation of the species responsible for the luminous emissions from the flames during conventional combustion [8][41]. This causes what may be the most striking characteristic of flameless combustion: there is no visible flame, hence the name ”flameless”. This is illustrated in figure 2.2 where heavy fuel oil is burned in conventional and flameless conditions: a significant difference in visual aspect is noticeable.

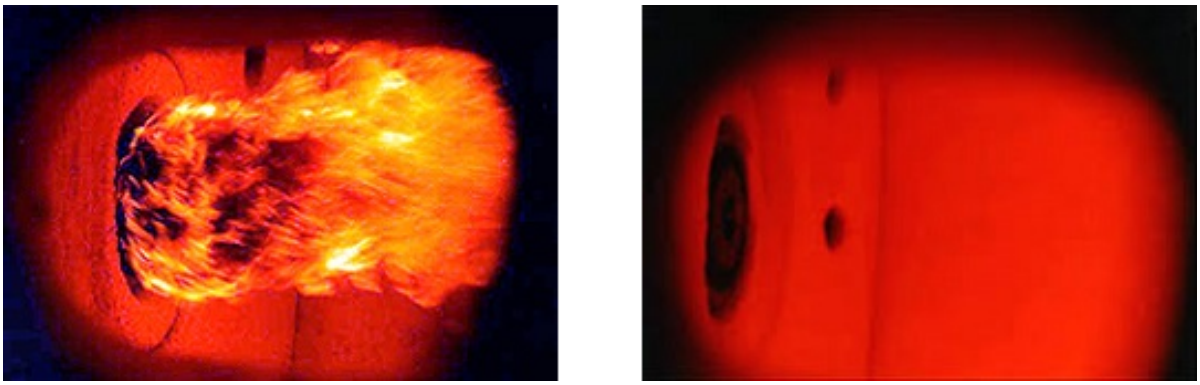

Figure 2.2: Conventional (left) and flameless (right) combustion of heavy fuel oil. Burner power $100\ kW_{th}$. Oxidizer left: standard atmospheric air ($21\%\ O_2$) preheated at $250°C$. Oxidizer right: vitiated air ($12\%\ O_2$) preheated at $500°C$ (from [35])

The inertization/vitiation process induces a mass effect dilution: the heat generated in the enlarged reaction zone [5] is distributed over more mass than for conventional combustion. This combined with an increased heat capacity (boosted by the presence of inert species) yields a rather uniform temperature field across the whole reaction zone, decreasing peak temperatures and displaying small temperature fluctuations [2][32] (see figures 2.3 and 2.4). In the case of ordinary combustion, a very strong temperature gradient is located near the burner exit in the flame zone with a clear peak temperature region in the same vicinity. In contrast, in highly preheated and diluted combustion, a far more uniform temperature field is observed with limited temperature gradients. Temperature fluctuations also decrease drastically between conventional and flameless combustion. Finally, species concentrations profiles show a great homogeneity as well [42][43]: in the absence of flame fronts no sharp gradients of concentrations are present. It is also worth mentioning that combustion under flameless conditions is complete resulting in only trace amounts of CO.

This explains why flameless combustion systems emit very low levels of NO_x: the main route for NO_x production in conventional systems is the thermal route triggered by high temperatures reached inside the flame. Flameless combustion prevents the activation of the thermal pathway (no high peak temperatures, small temperature fluctuations and low oxygen availability locally), effectively abating NO_x emissions.

The high level of temperature and combustion homogeneity inside the flameless combustion volume is evidenced in a flameless furnace installation at the International Flame Research Foundation (figure 2.5). The constant wall temperature along the whole furnace testifies for the absence of a main reaction zone close to the burner exit associated with strong gradients and heat release in a limited volume, characteristic of conventional combustion. However, figure 2.5 also highlights another characteristic of flameless combustion: it produces a high (and uniform) radiative heat flux compared to the same

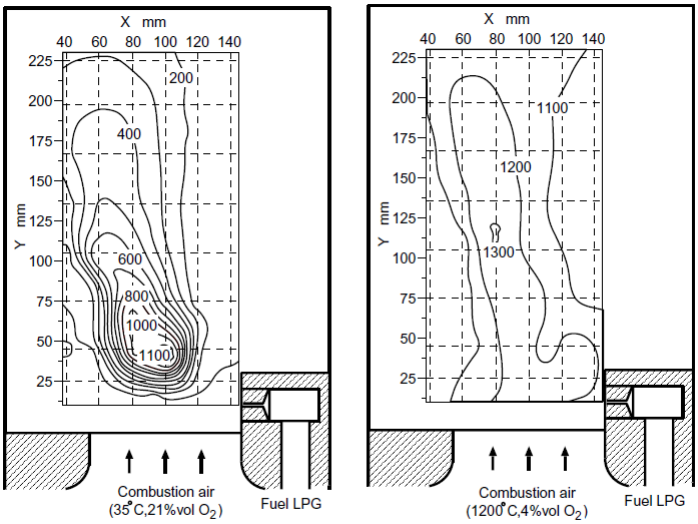

(a) Low temperature/normal air (b) High temperature/low oxygen conc. air

Figure 2.3: Temperature field comparison between conventional and flameless combustion (from [2])

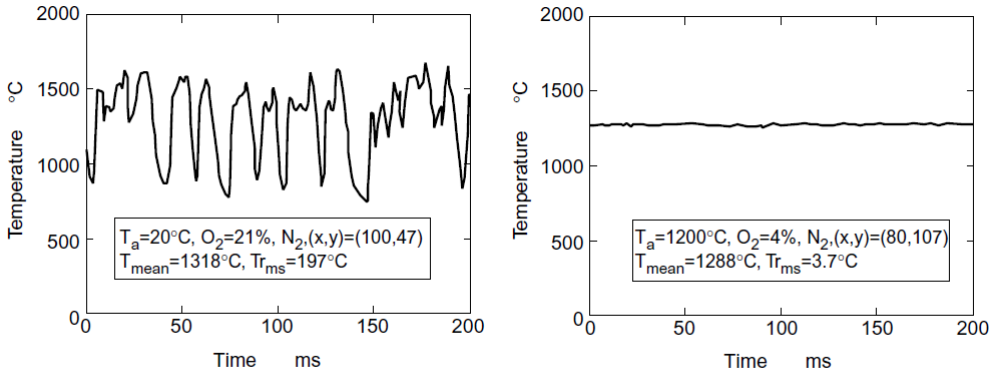

(a) Low temperature/normal air (b) High temperature/low oxygen conc. air

Figure 2.4: Temperature fluctuation comparison between conventional and flameless combustion (from [2])

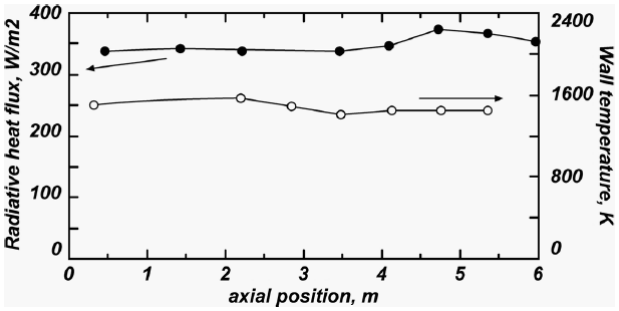

Figure 2.5: Radiative heat flux (left axis) and wall temperature (right axis) profiles in a flameless combustion furnace (from [44])

furnace with conventional burners [20][44].

The temperature and concentrations homogeneities displayed are consequences of the distributed volumetric combustion mode that is flameless combustion, in opposition to a flame front combustion mode. These characteristic often lead to the statement that combustion systems operating under flameless conditions work in almost ”well–stirred” conditions [34][43][45]. This is encouraging with respect to the modeling method and objectives of this work.

Finally, Wünning and Wünning [32] also reported that flameless combustion resulted in much lower noise levels than conventional combustion.

2.3.3. Desirable consequences of flameless combustion

Inherent characteristics of flameless combustion have desirable consequences in several aspects:

- flameless combustion shows great fuel flexibility and is not limited to the use of rich gaseous fuels such as natural gas. It can be applied as well with lean gaseous mixtures (such as biogas [46] or fuel gases recovered from industrial processes) or with liquid and even solid fuel (flameless pulverized coal combustion e.g.). The use of low calorific value (LCV) fuels is possible because of the auto–ignition temperature requirement [44][47] ;
- the same characteristic is also a great advantage in terms of safety. For a continuous process running constantly above the auto–ignition temperature, the risk of flame extinction or explosion is absent [33][47] which renders unnecessary the use of flame anchoring devices or pilot flames. Flameless combustion is sustained only thanks to appropriate conditions of temperature and mixing of fresh reactants with burned gases ;
- flameless combustion is ”material–friendly”. It induces lower thermal stresses on the burners and combustion chambers potentially increasing their lifetime. Homogeneous temperature profiles and relatively low maximum temperatures are of great interest when it comes to wear or treatment of materials [44] ;
- the pollution abatement potential of flameless combustion is threefold [44]: not only the formation of pollutants is suppressed (*clean combustion*) but they are also destroyed if they are present in the comburant streams (*cleaning combustion*). It is the case for organic species containing C, H or N atoms which can be oxidized or reduced into CO_2, H_2O or N_2. For inorganic species, no similar process is possible, but they can be released in a form less noxious or easier to separate because of their interaction either with the right diluent species, or with the combustion products, or even because of a specific chemical reaction catalyzed in just the right temperature interval. This is possible thanks to the adjustable narrow operating temperature range of flameless combustion. For this reason, it can also be called *cleanable combustion*.

2.3.4. Operation and stability domain

Wünning and Wünning [32] tried to characterize the operating domain of flameless combustion and its stability by relating their recirculation rate parameter K_v to their furnace temperature (figure 2.6). They defined K_v as the ratio of recirculated exhaust gases to the inlet comburant streams total mass flow rate:

$$K_v = \frac{\dot{m}_{e,recirculated}}{\dot{m}_{air,inlet} + \dot{m}_{fuel,inlet}} \tag{2.32}$$

They identified three combustion regimes:

- a region of stable conventional flames, with or without preheating at low K_v ;
- a region of unstable transitional behaviour, for slightly higher K_v and above the auto–ignition temperature ;
- a flameless combustion region, above the auto–ignition temperature and with a high enough K_v. It is clear that the flameless combustion processes evolve in a temperature and concentration range well outside the critical limits for conventional flame stabilization, largely thanks to the widening of the flammability limits under flameless conditions.

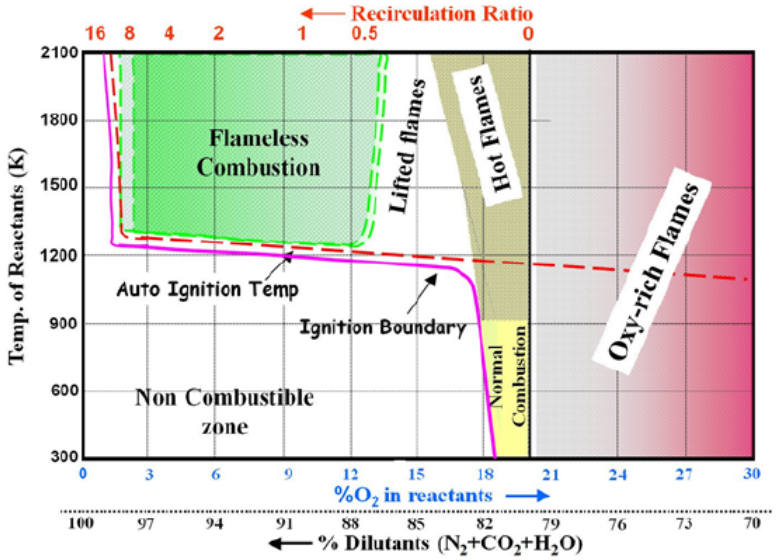

Figure 2.6: Stability diagram for different combustion regimes (from [48])

A good understanding of the operating domain of flameless combustion can be derived from using K_v but this parameter has two drawbacks: first, practically it is not easy to quantify the amount of recirculated flue gas, and second K_v is by no means a universal parameter. The threshold value from which flameless combustion can be sustained is known to vary depending on the fuel [8].

Nevertheless, it is possible to state that the phenomenon governing the stability of flameless combustion is the mixing of fresh reactants with burned hot gases.

2.3.5. Burner and furnace technology

Because flameless combustion represents such an excellent trade–off between fuel efficiency, pollutant abatement and potential to use the current combustion configurations with only slight modifications (burner retro–fitting), this strategy has spread rapidly in several industrial sectors despite the lack of some specific fundamental knowledge that would allow a complete and thorough understanding. Examples are steel, ceramic or glass furnaces [8]. With respect to conventional flames, the benefits of applying flameless combustion include a controlled homogeneous maximum temperature, substantial fuel savings, enhanced thermal efficiency and substantial reductions in pollutant emissions (to be related to decreased costs in pollution abatement devices and process control systems).

In practice, waste heat recovery is often implemented because of its advantages but also because reliable and efficient technology exists. Recuperators transfer energy from a steady flow of flue gas to the combustion air mainly via convective and radiative heat transfer. Regenerators transfer energy to an intermediate storing medium, such as a corrugated steel or ceramic matrix, later used to preheat the combustion air [12]. The multiburner flameless furnace of TU Delft is equipped with 3 pairs of regenerative burners with ceramic honeycomb–type heat exchangers. In each pair the burners are alternatively fired and in standby: during one firing cycle, air flows through the hot regenerator of the first firing burner and is preheated while the exhaust gases flow through the regenerator of the second standby burner at the opposite, storing heat. The temperature of the first regenerator decreases gradually and after the cycle duration the flow direction is reversed creating an alternating flow process. Typical cycle times are $20 - 60s$ [5].

The flameless burner technology for furnaces can be separated in two main configurations. The first configuration consists in a central fuel jet surrounded by a number of air jets. The most known in this category is probably the FLOX® burner developed by WS Wärmprozesstechnik GmbH in Germany [32][33] which can be fitted with a built–in regenerator (REGEMAT®) or recuperator (REKUMAT®). This is the type of burner used in the TU Delft multiburner furnace (REGEMAT® CD 200) (see figure 2.7). The FLOX® burner technology is based on separated high momentum injection of fuel and oxidizer creating strong internal recirculation of flue gases.

Figure 2.7: REGEMAT® CD 200 regenerative burner used in the multiburner flameless furnace of TU Delft (from [36])

The second configuration consists of burners with several fuel jets arranged around a central oxidizer jet. The idea is to delay the mixing between the reactants by positioning the fuel and air nozzles sufficiently apart from each other: as a result air and fuel streams will be diluted before they mix and react. The burners developed at NFK (Nippon Furnace Kogyo) may be the most notable of this category. Because of the high momentum injections and the lean operating equivalence ratios in practice, these technologies result in what is called a Strong Jet/Weak Jet (SJ/WJ) or Weak Jet/Strong Jet configuration, depending on whether the oxidizer stream is central.

Variations of these two main configurations exist, mainly by varying the number of surrounding jets or by injecting the surrounding jets at an angle, converging or diverging with respect to the central jet. However an important design which does not really fit in any of the categories mentioned is the burner developed by the Canadian Gas Research Institute (CGRI burner) in figure 2.8. It is a multiple jet (14) burner where fuel and oxidizer ports are arranged alternatively in a ring pattern, at an angle depending on the port type. It also delays mixing of fuel and oxidizer until both streams have been significantly diluted by entraining flue gases.

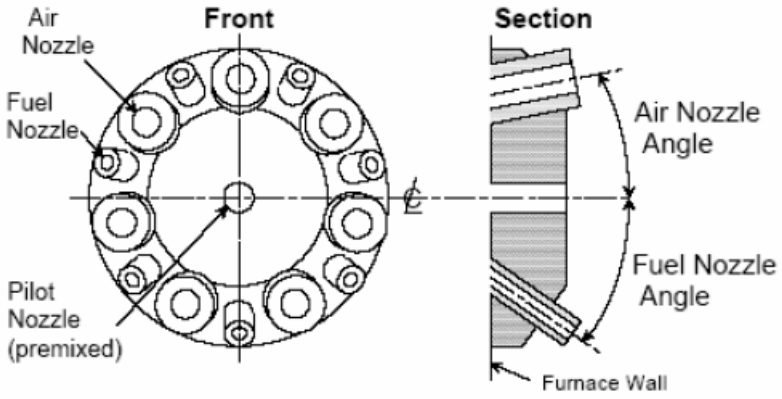

Figure 2.8: Different views of the CGRI burner (from [49])

Finally, one necessary condition to achieve flameless conditions is the temperature of the environment in which the fuel and oxidizer are injected that needs to be above the self–ignition temperature of the mixture. Therefore in the case of furnaces, it is necessary to heat them before flameless combustion can be used. This is usually done using conventional firing techniques, switched off as soon as the threshold is crossed. Some setups use burners that include this capability of switching from conventional to flameless firing, like the REGEMAT® CD 200, which makes their operation easier.

2.4. Jet modeling

Flameless burners technology is based on round turbulent jets injected with high momentum inducing a strong entrainment pattern. The following paragraphs briefly remind the basic physics of a free round jet and present two published jet entrainment models.

2.4.1. Free jet structure

A free jet injected into a quiescent environment is a good approximation of the burner technology in furnaces: high momentum air or fuel is injected into a furnace, containing gases which can be considered at rest. It is also the most basic and most studied configuration for a turbulent free jet. After injection, a round turbulent free jet develops with a general conical shape in three zones: the potential core region (not further than 4-6 port diameters), the transition region and the fully developed region (from 20-40 port diameters after injection). This evolution is due the exchange of momentum with the surrounding fluid.

In the fully developed region, the mean velocity field is well established and documented [50]: the axial velocity of the jet decays inversely proportional with the distance from the injection, and the radial profiles are self–similar (with a Gaussian shape). Often, when the focus is on the far field, the turbulent free jet is approximated to its fully developed region. In this case, no clear boundary of the jet is defined (it is a turbulent flow), but without buoyancy its evolution is statistically axisymmetric. Additionally it spreads linearly, forming a conical shape. Because in the fully developed region the velocity profiles are so well–defined, a common approximation for an effective radius law is to use the half velocity radius: the radius at which the velocity is half the axial velocity. Some researchers [51][52] tried to quantify the evolution of the true effective mean radius using intermittency measurements. Neglecting the virtual origin, the statistical mean radius law is:

$$B = C_s x \tag{2.33}$$

with x the distance from the injection plane and C_s the spreading coefficient. The value of the spreading coefficient depends on how the linear evolution is fitted with experimental data and thus depends on the publication but it usually represents a jet expansion of half angle close to $11°$.

2.4.2. Entrainment models

A turbulent free jet spreads and decays because it exchanges momentum with the surrounding fluid at rest, entraining it. The quantification of jet entrainment has been the focus of several studies, leading to the publication of various entrainment models. Two of them that will be used in this work are presented below.

The Ricou & Spalding model

Using their original experimental setup, Ricou and Spalding [53] determined the entrainment rate of free non-reacting jets with different densities into quiescent air. They found and reported that, *in the fully developed region*, the mass flow rate of the jet increases proportionally with the distance downstream from the point of injection:

$$\frac{\dot{m}}{\dot{m}_0} = C_e \frac{x}{d^*} \tag{2.34}$$

where $\dot{m}_0$ is the initial jet mass flow, d^* is the equivalent source diameter and includes the densities difference between jet and surroundings and C_e is the entrainment coefficient. The equivalent source diameter is defined as:

$$d^* = \frac{2\dot{m}_0}{\sqrt{\pi \rho_\infty \dot{G}_0}} \tag{2.35}$$

with ρ_∞ the density of the surroundings and $\dot{G}_0$ the initial momentum flux. In case of a top–hat jet exit velocity profile, it reduces to the well–known expression $d^* = d\sqrt{\frac{\rho_0}{\rho_\infty}}$. For momentum–driven free jets into a surrounding at rest (the influence of buoyancy is neglected, no coflow), the entrainment coefficient was determined to be $C_e = 0.32$.

The original reported expression of the model, sometimes used in modern publications is:

$$\frac{\dot{m}}{x\sqrt{\rho_\infty \dot{G}}} = \frac{\dot{m}}{x\sqrt{\rho_\infty \dot{G}_0}} = K_e \tag{2.36}$$

with $K_e = 0.284$. Assuming top–hat jet injection velocity profile, the relationship between K_e and C_e is:

$$K_e = 0.5\sqrt{\pi} C_e \tag{2.37}$$

Advanced entrainment model : Han & Mungal

The Ricou & Spalding model is valid in the fully developed region of a jet and does not allow to find the entrainment coefficient in the near–field of the injection plane. Using almost the same direct measurement method as Ricou and Spalding, Hill [54] resolved the entrainment rate at different axial positions. His (local) entrainment rate is defined as:

$$C_{el} = \frac{d^*}{\dot{m}_0}\frac{d\dot{m}}{dx} \tag{2.38}$$

He found that the local entrainment coefficient increases from a low value near the jet exit up to $C_{el} = 0.32$ within 13 jet diameters downstream (see figure 2.9).

In a more comprehensive parametric study of jet entrainment, Han and Mungal [55] tried to quantify the effects of axial position, heat release, buoyancy and coflow speed on the local entrainment rate. In order to validate their experimental setup, they presented results for a non–reacting pure air jet into air considered at rest: they obtained a similar trend as Hill, the coefficient growing from a low value near the nozzle up to 0.32 after 35 jet diameters downstream (figure 2.9). The difference with Hill's experiments is attributed to the different jet exit configurations: a convergent nozzle (Hill) and a long tube (Han and Mungal).

To put this result into equation, Ayoub [56] interpolated the data using a 6^{th} order polynomial and substituting d^* to d. For $\frac{x}{d^*} < 35$:

$$C_{el}(x) = a\left(\frac{x}{d^*}\right)^6 + b\left(\frac{x}{d^*}\right)^5 + c\left(\frac{x}{d^*}\right)^4 + d\left(\frac{x}{d^*}\right)^3 + e\left(\frac{x}{d^*}\right)^2 + f\left(\frac{x}{d^*}\right) + g \tag{2.39}$$

Interpolation coefficients for the Han & Mungal entrainment model

a	b	c	d	e	f	g
2.5×10^{-10}	-2.6×10^{-8}	1.2×10^{-6}	-3.5×10^{-5}	5×10^{-4}	6.7×10^{-3}	7.9×10^{-2}

For $\frac{x}{d^*} > 35$: $C_{el}(x) = 0.32$, constant and equal to the value of Ricou and Spalding.

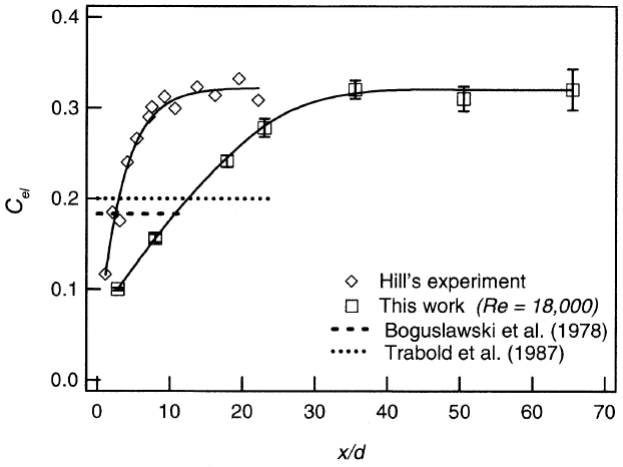

Figure 2.9: Han and Mungal's free jet entrainment coefficient along the axial direction

Han and Mungal also quantified the effects of coflow and heat release — in the case of reacting fluids — on the entrainment constant. The key parameter they introduced is the density weighted velocity ratio between jet and coflow:

$$r = \sqrt{\frac{(\rho_0 u_0^2)}{(\rho_\infty u_\infty^2)}} \tag{2.40}$$

Using this parameter they reported correlations for the asymptotic value of the entrainment rate (fully developed region) for both non–reacting and reacting fluids:

$$\text{Non–reacting (no heat release effect)} : C_{el}^{\infty} = 0.32\left(1 - \mathrm{e}^{(-0.036(r-1))}\right) \tag{2.41}$$

$$\text{Reacting (with heat release)} : C_{el}^{\infty} = 0.13\left(1 - \mathrm{e}^{(-0.036(r-1))}\right) \tag{2.42}$$

Finally they introduced the effect of buoyancy on the entrainment rate using a previously defined parameter:

$$\xi = \left(\frac{\rho_\infty}{\rho_0}\frac{g d_0}{u_0}\right)^{1/3}\frac{x}{d_0} = \mathrm{Ri}^{1/3}\frac{x}{d^*}, \text{ with Ri the Richardson number} \tag{2.43}$$

They found that in the buoyancy–driven region ($\xi > 1$), the local entrainment rate scales best with:

$$C_{el} = 0.090\xi^{3/2} \tag{2.44}$$

The evolution of the local entrainment rate for two reacting jets (that have the same density weighted jet to velocity ratio ($r = 55, 56$) but two different injection Reynolds number ($Re_d = 18000, 9000$ respectively)) is shown in figure 2.10a. For the two same jets the evolution is also plotted against the dimensionless coordinate ξ (figure 2.10b).

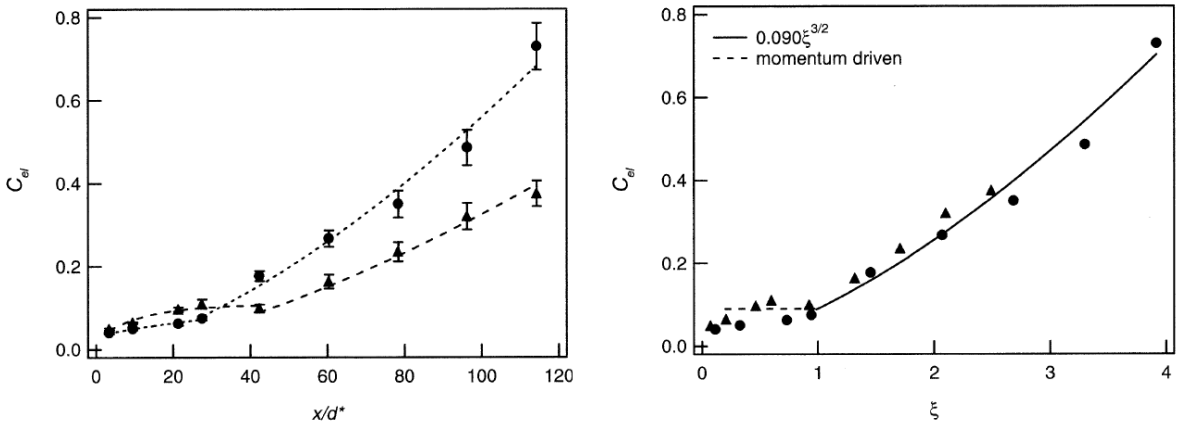

(a) Effect of buoyancy on C_{el}

(b) Using ξ as a coordinate system

Figure 2.10: Effect of buoyancy on jet entrainment

3

Emission modeling of a lifted jet flame

3.1. Introduction

Flameless combustion is a technology that already has a large number of industrial applications although there is a lack of fundamental knowledge of the process that can prevent a more widespread implementation. The design of facilities is assisted by numerical predictions using reliable models that have proven their performance for conventional furnaces. However such models may not work as well to predict the performance of flameless combustion furnaces because the combustion characteristics are different from conventional firing: the flame stabilization mechanisms are expected to be different, as well as the combustion regime given the relative importance of the chemistry time scale (slow kinetics) and the flow time scale (enhanced mixing). To develop accurate models capable of modeling the specifics of flameless combustion, detailed insights of the relevant physical phenomena is needed. Yet, fundamental investigation of the combustion process is impossible with large industrial devices. Open laboratory scale experiments allow access to various quantification and measurement strategies like laser–optical techniques. This is the purpose of several experimental setups to emulate flameless combustion conditions, that would eventually help gain more fundamental knowledge of the physical processes involved. The Delft jet–in–hot–coflow (DJHC) burner is one of those [57], for which the design was inspired by the Adelaïde jet–in–hot–coflow burner [58]. But the experimental system of interest in this chapter is the turbulent jet flame in hot coflow setup reported by Fujimori, Riechelmann and Sato in [59].

Their setup consists of a combustion duct mounted on top of a regenerator. A schematic representation of the combustion duct is displayed in figure 3.1. Methane is injected through a nozzle located at the center of the duct of variable inner diameter D_j ($1\,mm$ or $2\,mm$) and outer diameter $8\,mm$. The regenerative storage heater below the duct preheats the coflowing stream of air injected in the duct over the remaining cross section at a constant flow rate of $333\,Nl/min$. During one cycle in the experiment, the coflow temperature drops from about $1470\,K$ to $1220\,K$ (corresponding to inlet velocities ranging from $6.1\,m/s$ to $5.1\,m/s$). The fuel (methane) is injected at a constant temperature taken as $373\,K$. For each fuel nozzle diameter, several fuel injection rates were investigated:

Fuel injection rates		
$D_j\,[mm]$	1	2
Fuel flow rate $Q_f\,[Nl/min]$	2.0	5.0
	3.0	7.5
	5.0	xxx

Table 3.1: Different fuel injection rates in Fujimori et al. experiments

For the case $D_j = 1\,mm$ and $Q_f = 3.0\,Nl/min$ it yields an average jet exit velocity of $87\,m/s$. The fuel and coflow streams can be pure but also diluted with N_2.

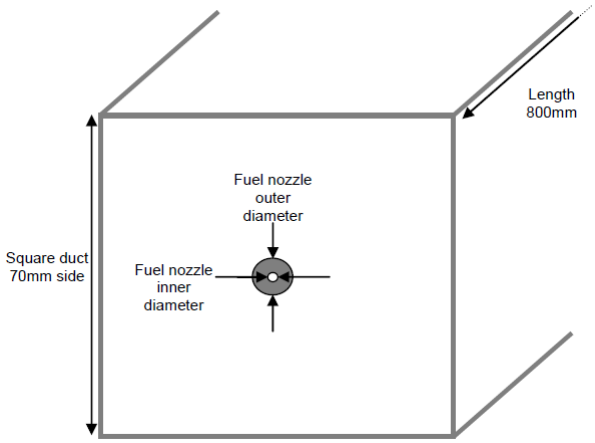

Figure 3.1: Schematic representation of the combustion duct of Fujimori et al. experimental setup

The authors first tried to examine and describe the liftoff characteristics of the jet flame in a hot air coflow which resulted in a relationship of the type $h_{liftoff} = f\left(T_{coflow}\right)$, as illustrated in figure 3.2a. In particular it shows that the air coflow temperature has a strong influence on the liftoff height of such flames.

They presented next their NO_x emission measurements of these flames, in terms of $EINO_x$ $[g/kg]$ (see figure 3.2b). For both fuel diameters, a sudden drop in $EINO_x$ is noticeable for the flames with liftoff. The temperature range in which it happens is different when the nozzle diameter changes.

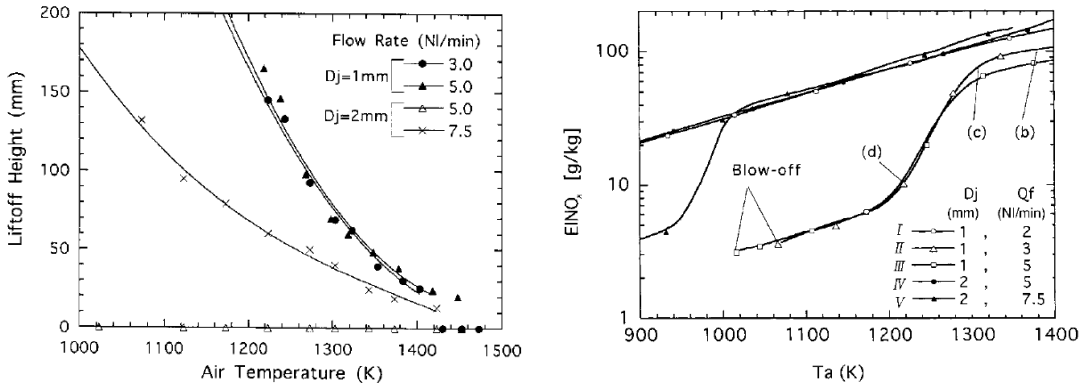

(a) Liftoff height

(b) EINOx

Figure 3.2: Change of liftoff height and evolution of EINOx of pure methane jets with coflowing air temperature (from [59])

The CRN simulations of this chapter aim at reproducing, at least qualitatively, this trend. One case will be simulated:

- $D_j = 1\,mm$;
- $Q_f = 5.0\,Nl/min$;
- pure methane ;
- undiluted air coflow.

Before starting building a reactor network, some additional specific literature will be presented in the next section: a published work from Broadwell and Lutz [60] reporting the development of a 2–reactor model for a jet flame, and a review about diffusion flame stability [61].

3.2. Additional literature

3.2.1. Turbulent jet flame emission modeling : a 2–reactor model

Broadwell and Lutz [60] investigated the possibility of a proper mathematical modeling of a turbulent jet flame, including the chemical reactions occurring. Experimental findings first led to the design of what is called the ”Two–Stage Lagragian model” which is an approximate description of the chemical reactions occurring in turbulent jets and mixing layers. The base of this concept is that turbulent non–premixed jet flames can be described with two regions: a relatively broad and homogeneous zone (”Core”) and a thin mixing layer where fast reactions occur (”Flame sheet”), illustrated in figure 3.3. The surrounding air is entrained radially into the flame sheet where it reacts with the fuel diffusing radially outward from the core.

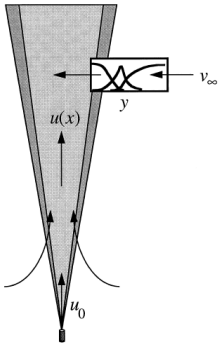

Figure 3.3: Sketch of the TSL model (from [60])

Using mass conservation equations from the TSL model and the same two regions discretization, they newt postulated that this system could be approximated using a 2–reactor model: the homogeneous core and the flame sheet could be seen as Perfectly Stirred Reactors (PSR), while the outward diffusion of fuel from core to sheet and inward diffusion of the resulting combustion products from the sheet could be modeled by convective flows that produce stoichiometric conditions in the flame sheet PSR. A schematic of this configuration is presented figure 3.4. An important input of this model is the flame sheet residence time τ. It is not difficult to imagine that its value is impacted by several parameters and is not constant along the flame: the Reynolds number and buoyancy effects can affect the flame length and distortions, while downstream residence times are supposed to be greatly reduced compared to upstream values. As reported by the authors, assessing these effects on τ is extremely difficult. However, a relatively weak influence of τ on the emission indices allowed them to adopt a simple scaling law for the residence time: $\tau = c\left(\frac{d_0}{u_0}\right)$, where c is set to match the experimental emission index at one condition. They determined a value of $c = 30$, which they used for all their simulations involving different types of fuel: methane, CO/H_2, and hydrogen.

A second input needed by the 2–reactor model is the entrainment of surrounding fluid into the flame sheet. Broadwell and Lutz point out that buoyancy and radiation effects are not negligible on the entrainment intensity and on the final $EINO_x$ values and should ideally be accounted for. They implemented a radiation law from the core region to the surroundings where the radiation flux is ruled by:

$$\dot{Q}_r = \varepsilon\sigma\left(T^4 - T_\infty^4\right) \tag{3.1}$$

with $\sigma = 5.670373 \times 10^{-8}\, W/m^2/K^4$ the Stefan–Boltzmann constant and ε the gray–gas emissivity. The value of ε is taken constant, adjusted to match measured radiant fractions for hydrocarbon fuels.

Buoyancy is accounted for in the jet entrainment model along with the influence of having reacting species: the simple Ricou & Spalding jet entrainment model with a modified entrainment constant C_e is used. A law ruling the evolution of C_e, affected by both buoyancy and heat release by reacting fluids, is needed. Interestingly, a couple years later, Han and Mungal [55] tried to combine their new advanced entrainment laws with the TSL model of Broadwell and Lutz to model the NO_x emissions from a lifted flame in coflow. This combination constitutes the cornerstone of the following reactor network development.

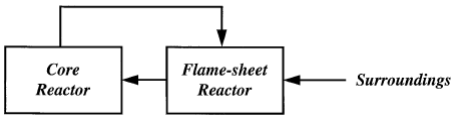

Figure 3.4: Schematic of the 2–reactor model (from [60])

3.2.2. Diffusion flame stability

A review of diffusion flame stability limits can be found in [61]. Analysis of flames phenomena is not trivial because they are the result of balance or mismatch between flow and chemical characteristics locally: flow velocity / flame velocity, characteristic mixing time / characteristic chemical reaction time... Being related to the turbulence–chemistry interaction is what makes flame stability analysis not an easy subject to tackle.

The usual vocabulary to characterize flame stability is threefold:

- liftoff velocity: the mean jet velocity at which the flame lifts above the burner rim ;
- liftoff height: the distance between the base of the lifted flame and the nozzle exit ;
- blow–out velocity: for an already lifted flame, if the jet velocity is increased too much the flame is being pushed in a downstream region where reaction cannot be sustained. The velocity at which the flame first extinguishes is called the blow–out velocity.

Flame extinction can also occur without going through the liftoff stages when the attached flame directly goes out. Finally the flashback event is also part of the stability and safe operation boundary for a burner.

Three stability models for diffusion flames are presented, each having its own characteristics and assumptions not detailed here:

- premixed flame propagation model ;
- laminar flamelet model ;
- large–scale turbulence structural mixing model.

Those theories were derived based on various experimental observations, and were in turn used to derive analytical correlations for the flame stability parameters mentioned above. It appeared that none of them can explain fully the mechanisms of liftoff and blow–out alone, but two dominant theories emerged: the *premixed flame propagation* model yields simple universal correlations for the liftoff height of rather good quality while being poor at predicting the blow–out limits. Inversely, the *large–scale turbulent mixing* model is consistently good at predicting the blow–out velocity but less successful when applied to flame liftoff height prediction.

It is possible to draw one important conclusion from this review: the complexity of the jet flow field of lifted flame systems is very challenging to model, and its interaction with the chemistry adds to the complexity. Linking this conclusion to the objective of this chapter (using CRN modeling to predict emissions from a lifted jet flame in hot coflow), two comments can already be made:

- It seems unfeasible to build a reactor network which can capture and resolve the liftoff height given only the geometrical characteristics and inlet flow rates of the system: the detailed chemistry is available but reaching this objective is hindered by the rough flow field discretization inherent to CRN modeling. Furthermore the turbulence is not modeled, let alone the turbulence–chemistry interaction ;
- On the same trend, good emission predictions using reactor networks at least calls for a decent enough flow pattern modeling. Given the complexity of the lifted jet flame in hot coflow, it might not even be possible to obtain this basic standard.

Keeping in mind these preliminary remarks, a reactor network modeling the lifted jet flame in hot coflow setup of Fujimori et al. is designed, in the hope to capture their experimental results. The design process is detailed in the following section.

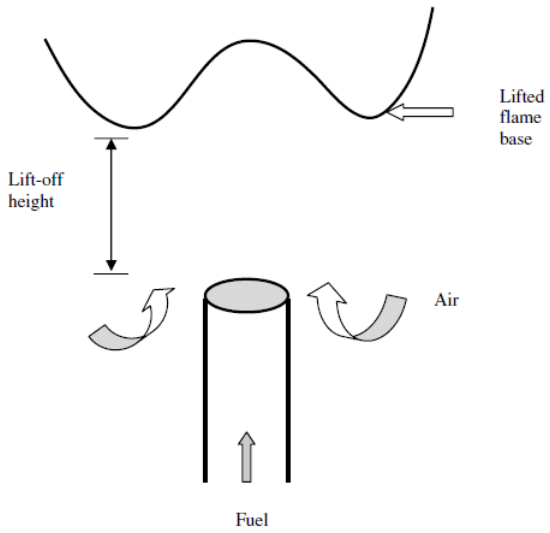

Figure 3.5: Features of a lifted jet diffusion flame (from [61])

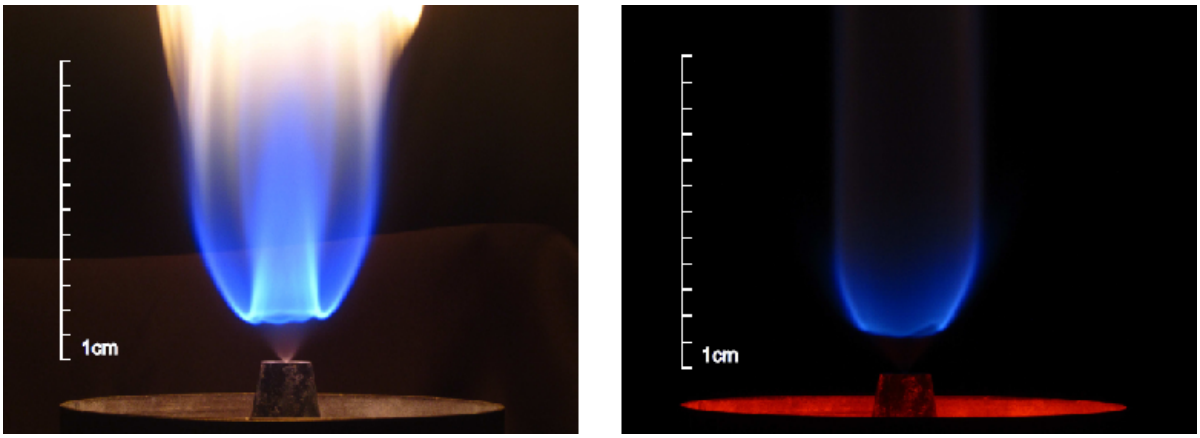

Figure 3.6: Images of lifted jet flames from the DJHC setup [37]

3.3. Reactor network

3.3.1. Architecture

The general architecture of the network is based on the combination of the 2–reactor model reported in 3.2.1 with the advanced entrainment model of Han & Mungal (2.4.2). In parallel the enclosure geometry (3.1) is accounted for, and following the preliminary comments in 3.2.2 the liftoff height is used as model input. Combining these ideas, 4 characteristic regions of the combustion duct are identified and schematically represented in figure 3.7:

1. **Premixing region:** between the fuel injection port and the liftoff height, a round free jet behavior is assumed. The fuel jet entrains surrounding air and expands. Instead of the usual expansion semi–angle ($\approx 11°$, see 2.4.1) for a free jet in still air, an arbitraty value of $9°$ is assumed:

   - the coflow is expected to have a ”channeling” effect, even mild ;
   - it simplifies the network design given the liftoff height data and the combustion duct dimensions while keeping an acceptable value. It is not expected to have a major influence on the emissions.

   A constant volume PSR is used to model this region, which volume is calculated according to the round free jet characteristics just mentioned (a truncated cone of round basis and height $h_{liftoff}$). In this PSR, the fuel stream premixes with a quantity of surrounding coflow defined by the entrainment model. The radius law of this free jet is ruled by:

   $$r = \frac{d_0}{2} + C_s^{premix} x, \text{ where } C_s^{premix} = \tan(9°) = 0.1584. \tag{3.2}$$

2. **Ignition region:** located just after the premixing region, it starts at the liftoff height. Physically, ignition occurs in this region. It is modeled using the 2–reactor pattern, implemented with two constant volume PSRs. The streamwise extent of this region ($L_{pattern}$) is governed by the equivalence ratio imposed in the flame sheet reactor. Inside this reactor, the entrained coflow and the corresponding core fluid mix and ignite: a streamwise position exists at which the available mass flow through the core reactor is not enough to reach the target equivalence ratio in the flame sheet, before ignition.

   In parallel, because the available coflow is in limited amount (enclosed system), there is an axial position at which the coflow has been entrained in full into the main jet stream according to the entrainment law. At this position (x_{max}) the main jet boundaries reach the enclosure boundary.

   Between $h_{liftoff}$ and x_{max} the main jet stream is assumed to keep a general expanding conical shape but with a different jet expansion coefficient, calculated with:

   $$C_s^{flame} = \frac{r_{enclosure} - r_{max}^{premix}}{x_{max} - h_{liftoff}} \tag{3.3}$$

   where $r_{enclosure} = \frac{l_{enclosure}}{\sqrt{\pi}}$ is the equivalent radius of the square combustion duct of side $l_{enclosure}$ and r_{max}^{premix} is the jet radius at liftoff height.

   The total volume of the pattern is again calculated assuming a truncated conical shape of height $L_{pattern}$. The volume of the sheet reactor is determined by the flame sheet residence time τ_{sheet}, a model input. The volume of the core reactor is deduced.

3. **Post–ignition region:** this region is located between the axial positions $h_{liftoff} + L_{pattern}$ and x_{max}. In this region the ignited core flow keeps gradually entraining the coflow, and the combustion phenomenon continues. It is modeled using a number of constant volume PSRs (n_{PSR}^{post}) which value is the result of a trade–off between simulation time and independent emission predictions (see appendix B). This parameter is expected to have an extensive impact on the predictions: not enough PSRs won't capture accurately an expected high temperature region where the bulk of the NO_x would be produced ; too many PSRs will result in an unacceptable simulation time but will resolve the high temperature regions and produce an independent NO_x estimation.

The reactors volumes are calculated using the expansion coefficient C_s^{flame} and assuming once again the truncated circular cone shape.

4. **Downstream duct / Exhaust region:** this region starts from x_{max} and extends until the combustion duct exhaust. It is modeled using a single constant volume PSR which volume is the volume of the combustion duct between the corresponding streamwise positions:

$$V_{last} = (L_{enclosure} - x_{max})\, l_{enclosure}^2 \tag{3.4}$$

where $L_{enclosure}$ is the length of the combustion duct.

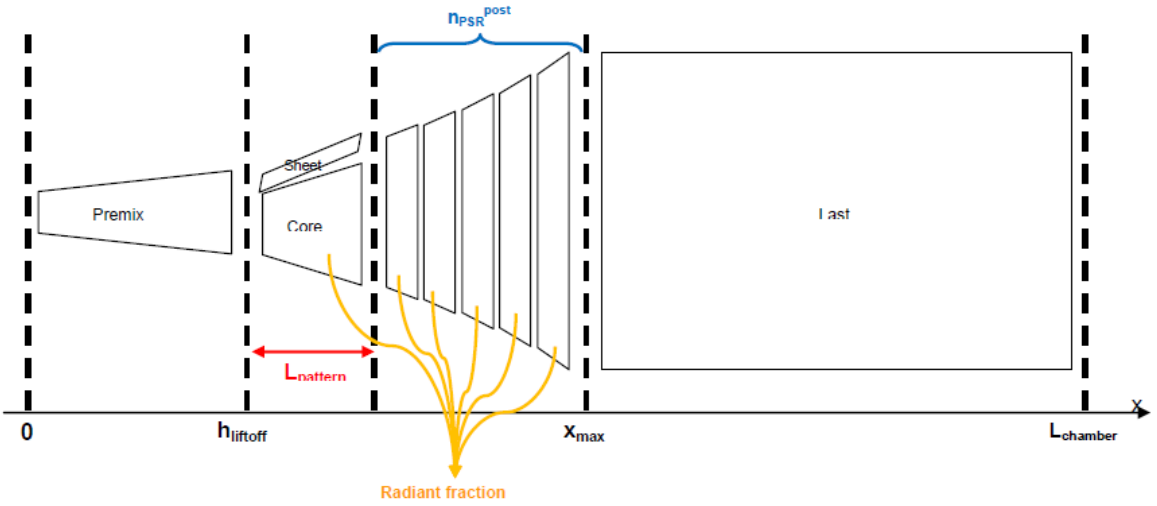

Figure 3.7: Sketch of the combustion duct discretization in 4 regions

Implementing a heat loss model is also necessary. Despite all the efforts made to isolate the experimental setup, it still loses heat to its surroundings. It is assumed that heat loss only occurs from the core reactor and post–ignition reactors to the surrounding coflow, which in turn loses this excess heat instantly to the duct surroundings. This means the coflow temperature remains constant in the region of the combustion duct where it is present. Following the work of Broadwell and Lutz [60] the losses are defined via the radiant fraction:

$$\chi = \frac{\text{Radiative heat loss}}{\text{Heat of combustion}} = \frac{A_{core}\varepsilon\sigma\left(T_{core}^4 - T_{coflow}^4\right) + \sum_{i=1}^{n_{PSR}^{post}} A_i\varepsilon\sigma\left(T_i^4 - T_{coflow}^4\right)}{\phi_m^{fuel} LHV_{fuel}} \tag{3.5}$$

where A is the lateral area of the corresponding reactor and ε the average emissivity of all fluids inside the considered reactors. Because the radiant fraction is user–specified, the model adjusts the emissivity to match this setting given the reactors temperatures and lateral areas.

Finally the pressure in the system is regulated by a system of valves and is virtually maintained constant at $p_{chamber} = 1\,atm$. See appendix A for precisions on the valve coefficient.

A final sketch of the reactor network is displayed in figure 3.8. Diamond–tipped arrows represent heat loss, ”standard” arrows stand for imposed mass flows and the last type of arrows represents valve connections.

An igniter input can be noticed: it is included to ensure ignition at $h_{liftoff}$. Ignition is artificially stimulated using a transient stream of $H^\bullet$ radicals injected during the first iterations of the system. It successfully ignites the sheet reactor, where combustion is sustained once the igniter mass flow is stopped. This additional energy input has no influence on the steady–state solution provided a good calibration. The igniter mass flow is implemented as time dependent Gaussian, which constants were adjusted so that the maximum value is much smaller than the debited mass flow from the core, and so that its value drops to 0 faster than the convergence time. A typical time evolution of the igniter mass flow is provided in figure 3.9.

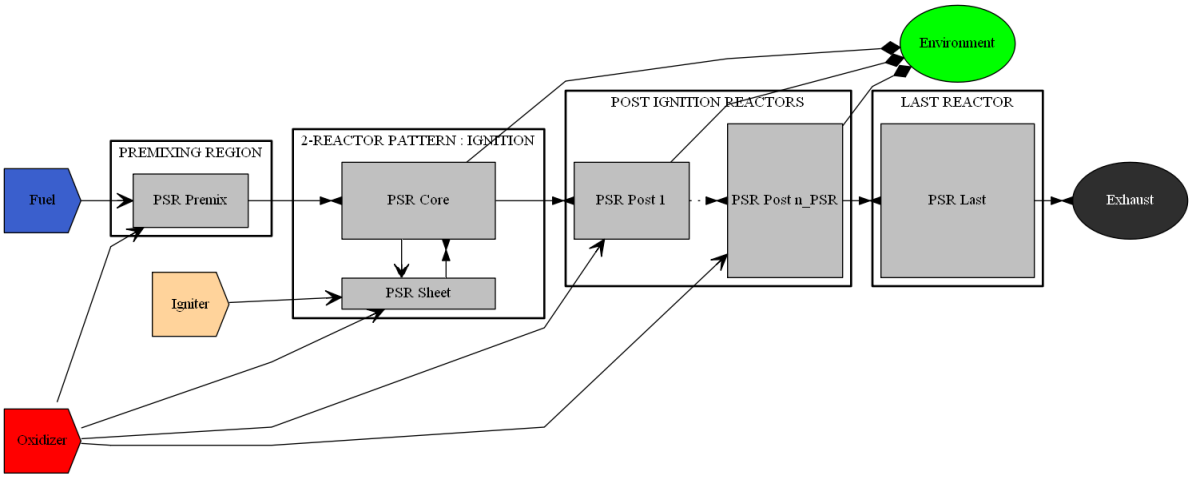

Figure 3.8: Sketch of the designed reactor network

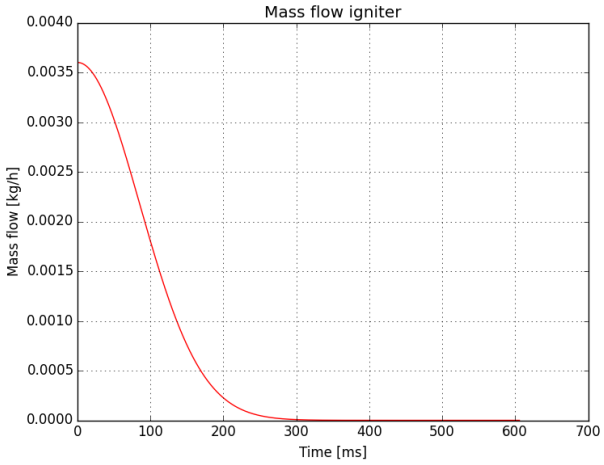

Figure 3.9: Typical time evolution of the igniter mass flow

3.3.2. Model inputs

This model's inputs are classified in two categories: the internal model inputs can be tuned to adapt the model to the fixed characteristics of the system (geometry e.g.) but they are also related to the iteration loop. The user–defined inputs can be varied by the user just to adapt to experimental conditions. The complete set of parameters describing these conditions was included although only one of them will be varied: T_{coflow}. In the original study the authors report experimental data obtained by varying also D_j, $\phi^N_{v,fuel}$ and the streams dilution with N_2 using Y_F and Y_O. Table 3.2 gathers all the model's inputs.

The iteration loop tolerances are used to determine the convergence conditions that must be fulfilled to stop the simulation. Because of the loop choice to iterate the reactor network, a safeguard for maximum simulation time is implemented: even if there is no convergence during this time the simulation stops but displays a warning that something is wrong in the network.

To minimize the simulation time and start with reasonable internal mass flows and compositions, an initialization loop for the 2–reactor pattern is implemented. The pattern is simulated without ignition over a given time span (t_max_init) using a specified time step (dt_init).

Although the liftoff height at given conditions is a model input, there is no liftoff height input specified. A power law interpolation of figure 3.2a allows to clearly define the liftoff height via the coflow temperature specification:

$$h_{liftoff} = 2.3809 \times 10^{41} \times T_{coflow}^{-12.691} \tag{3.6}$$

with $h_{liftoff}$ in mm and T_{coflow} in K.

USER–DEFINED		INTERNAL	
Fuel port inside diameter $[mm]$:	D_j	Duct dimensions $[m]$:	$L \times l \times l$
Fuel inlet volume flow $[Nl/min]$:	$\phi^N_{v,fuel}$	Coflow inlet volume flow $[Nl/min]$:	$\phi^N_{v,coflow}$
Inlet coflow temperature $[K]$:	T_{coflow}	Inlet fuel temperature $[K]$:	T_{fuel}
Fuel mass fraction in fuel stream :	Y_F	Fuel calorific value $[J/kg]$:	LHV_{CH_4}
O_2 mass fraction in coflow stream :	Y_O	Valve coefficient $[kg/s/Pa]$:	K_v
		Jet expansion rate premixing :	C_s^{premix}
		Scaling constant τ_{sheet} :	K_τ
		2–reactor pattern init. time step : $[s]$	dt_init
		2–reactor pattern init. time span : $[s]$	t_max_init
		Max simulation time $[s]$:	t_max
		Axial discretization step $[m]$:	dx
		Iteration loop abs. tolerance :	a_tol
		Iteration loop rel. tolerance :	r_tol
		Length of 2–reactor pattern $[m]$:	$L_{pattern}$
		Number of PSR post–ignition :	n_{PSR}^{post}
		Radiant fraction :	χ

Table 3.2: Classification of the inputs of the lifted flame model

Finally the entrainment has no specific input as well while it is required by the model: the local entrainment rate constant is calculated internally before each simulation. A streamwise discretization step is specified as input: it influences the local axial positions at which entrainment will be calculated. The entrainment law is built using Han & Mungal's results [55]: for the momentum–driven region the reacting C_{el}^{∞} (equation 2.42) is used, for the buoyancy–driven region equation 2.44 is used. Both functions are properly connected. Figure 3.10 shows the calculated evolution of the local entrainment constant and the resulting entrained mass flow along the combustion duct. The parameter x_{max} defining the end of the post–ignition region and the start of the last region is clearly illustrated: the axial position at which the whole coflow has been entrained.

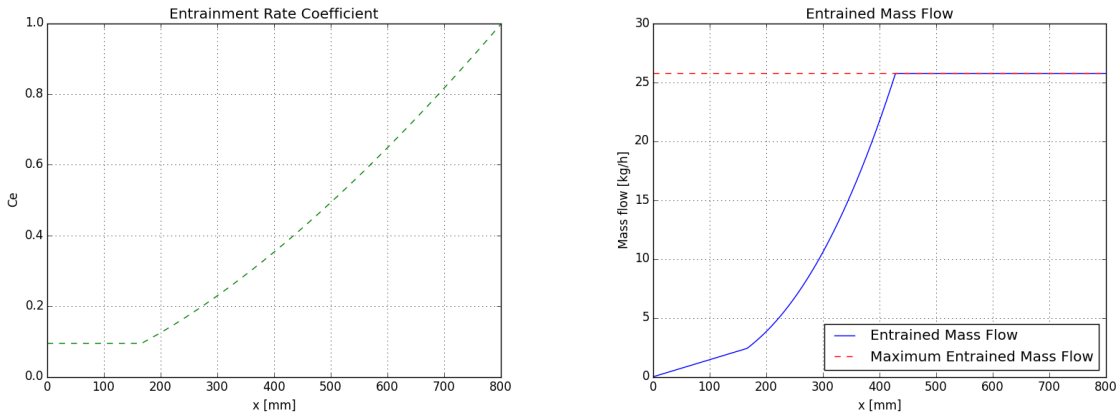

(a) Local entrainment coefficient

(b) Mass flow entrained

Figure 3.10: Entrainment characteristics for $T_{coflow} = 1310\,K$ / $h_{liftoff} = 65\,mm$

3.3.3. Simulation cases

From all the conditions investigated experimentally, only one set is simulated: $D_j = 1\,mm$; $Q_f = 5.0\,Nl/min$; pure methane ; undiluted air coflow. The liftoff height data available restricts the range of coflow temperatures that can be simulated. In total 6 cases spanning the liftoff height data are modeled (table 3.3).

Case n°	$T_{coflow}\,[K]$	$h_{liftoff}\,[mm]$
1	1250.0	118
2	1280.0	87
3	1310.0	65
4	1340.0	49
5	1370.0	37
6	1400.0	28

Table 3.3: Simulation cases of the lifted flame for the selected conditions

3.3.4. Calibration of the reactor network

Three main parameters of the model remain to be determined: $L_{pattern}$, n_{PSR}^{post} and χ. The purpose of the calibration is to find the best value for each of these parameters, for each case, consistently. The calibration is executed in a specific order:

1. $L_{pattern}$ is first determined, without heat loss ($\chi = 0.0$). The definition of $L_{pattern}$ was given in 3.3.1: determining this value is completely unrelated to the predicted emissions. A very small n_{PSR}^{post} setting is then used to reduce the simulation times. $L_{pattern}$ is determined for all cases.

2. n_{PSR}^{post} is gradually increased, maintaining $L_{pattern}$ to its newly determined value, still without heat loss ($\chi = 0.0$). A n_{PSR}^{post}–dependency study is performed on the $EINO_x$. Ideally the final selected value would be the minimum number of PSRs necessary to have a prediction independent from n_{PSR}^{post}, but the simulation time also has to be part of the constraints. The n_{PSR}^{post}–dependency study is conducted only on one reference case: eventually it allows to define a certain reactor density in the post–ignition region. A similar value is used for all other cases. *Case n°3 is selected as reference.*

3. Finally, with the proper values of $L_{pattern}$ and n_{PSR}^{post}, the radiant fraction is adjusted so that the predictions and the experimental data match for the reference case. The same radiant fraction is used for the other cases

Details of the calibration can be found in appendix B. Table 3.4 gathers the results of the calibration process for all cases.

3.3.5. Conclusion

This reactor network has been designed to be system specific: it relies on liftoff height data obtained with the experimental setup. However if the modeling approach is successful in predicting the emissions, a similar architecture may be applied to other lifted jet flame setups provided liftoff height data is available. A summary of the model inputs with their values is provided in table 3.5.

Case n°	$T_{coflow}\,[K]$	$h_{liftoff}\,[mm]$	$L_{pattern}\,[mm]$	n_{PSR}^{post}	Unit PSR length $[mm]$	χ [%]
1	1250.0	118	3	9	33.2	32.25
2	1280.0	87	15	10	32.2	32.25
3	1310.0	65	29	10	33.4	32.25
4	1340.0	49	41	10	34.2	32.25
5	1370.0	37	52	10	34.7	32.25
6	1400.0	28	60	10	35.2	32.25

Table 3.4: Results from the calibration process of the lifted flame model

USER–DEFINED		**INTERNAL**	
D_j :	$0.001\,m$	$L \times l \times l$:	$0.8m \times 0.07m \times 0.07m$
$\phi_{v,fuel}^{N}$:	$5.0\,Nl/min$	$\phi_{v,coflow}^{N}$:	$333.0\,Nl/min$
T_{coflow} :	Case dependent $[K]$	T_{fuel} :	$373\,K$
Y_F :	1.0	LHV_{CH_4} :	$50.0 \times 10^6\,J/kg$
Y_O :	0.233	K_v :	$1.0 \times 10^{-4}\,kg/s/Pa$
		C_s^{premix} :	0.1584
		K_τ :	30
		dt_init :	$1.0 \times 10^{-4}\,s$
		t_max_init :	$10.0\,s$
		t_max :	$5.0\,s$
		dx :	$0.001\,m$
		a_tol :	1.0×10^{-6}
		r_tol :	1.0×10^{-6}

Table 3.5: Simulation inputs for the lifted flame model

3.4. Results

For the simulations, the *chemical mechanism GRI 3.0* is used. Each case is simulated with and without heat loss and the predictions are compared to the experimental trend reported by Fujimori et al. The results are displayed in figure 3.11.

First it is worth noting the importance on the predicted emissions of the heat loss from the system to the surroundings. In the absence of heat loss, the predictions are more than double the predictions when heat loss is accounted for. It is consistent with a dominant thermal–NO pathway. However the trend of the predictions does not even begin to follow the sudden drop in $EINO_x$ observed experimentally: the modeling approach has failed.

One reason for the obtained trend can be found in temperature profiles along the combustion duct. For all simulated cases, they are plotted in figure 3.12. The exhaust temperatures are consistent with the different energy input of each coflow temperature. All these profiles have a common characteristic: the location and intensity of the peak temperature. Regardless of the liftoff height a peak temperature region is predicted around the same streamwise position with a maximum temperature between $2400\,K$ and $2500\,K$ (see figure 3.13). The maximum temperatures are consistent with the energy input except for case 1, which is probably due to an insufficient discretization of the post–ignition region. The predicted mild decrease in $EINO_x$ is the result of this slight difference in peak temperature combined with the heat loss model which effect can be noticed in the post–ignition region: the hot regions are less and less hot when the coflow temperature decreases.

These observations lead to several conclusions as to the failure of the designed reactor network to predict the sudden drop in $EINO_x$.

1. Such a sudden drop compared to the predicted mild decrease must be induced by a radical change in the physics and chemistry involved, or at least in the geometry of the flame. The reactor network does not allow the capture of radical geometry changes: it is possible that while liftoff increases multiple flame fronts appear, not necessarily of the same type (diffusion, premixed). For instance for far lifted flames, triple flames may play a dominant role and induce a radical change. It may not be adapted to model this transition phenomenon using only one reactor network: one network to model near–lifted flames and one to capture the far–lifted flames behavior could be a solution. However this raises one question: which criteria would be used to switch from one to the other? And assuming this approach works, the sudden drop would most probably not be predicted as smoothly.

2. It seems like obtaining predictions closer to expectations would require the model to be able to predict the peak temperature regions more distributed spatially: one could expect the peak temperature region to occur earlier for high coflow temperature (low liftoff height). In parallel the peak temperature of far–lifted flames may be significantly lower than what is predicted here, yielding a much flatter temperature profile. This could be due to recirculating patterns that may contribute to dilute the mixture with flue gas before ignition, thus creating conditions closer to flameless combustion. A triple flame structure may also participate in a peak temperature reduction. These phenomena in synergy could account for a radical drop in NO_x emissions.

3. Finally the heat loss to the environment and heat exchanges within the system should definitely be accounted for. The heat loss model implemented is simplistic and a more advanced model might bring improvements. Nevertheless, designing a new architecture which can capture the far–lifted behavior should be the number one priority: even combined with the same simple heat loss model it should bring significant improvements.

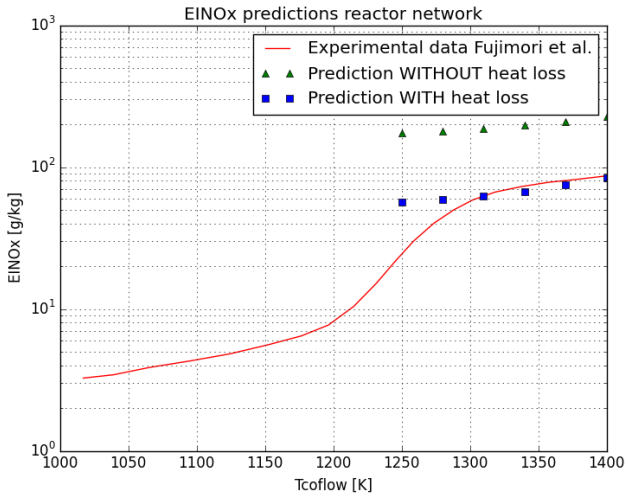

Figure 3.11: Reactor network predictions vs experimental data for the lifted jet flame

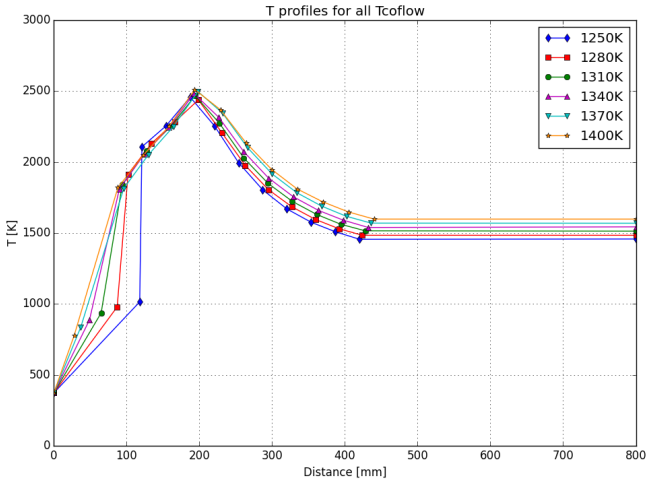

Figure 3.12: Predicted temperature profiles along the combustion duct

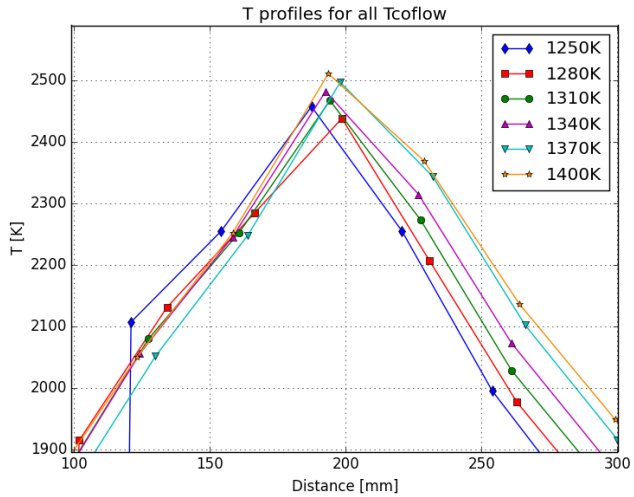

Figure 3.13: Detailed view of the peak temperature region

3.5. Conclusion

Based on literature, a reactor network was designed in order to predict NO_x emissions of a lifted jet flame in hot coflow system. Several modeling challenges were encountered calling for sharp assumptions. For instance because of the likely impossibility to obtain the liftoff height as a model output, the liftoff data is used as a model input. Modeling the flow pattern and the heat exchanges properly turned out to be very complex.

The performed simulations resulted in an unsatisfying prediction of the evolution of the $EINO_x$. The objective of capturing the sudden drop of the emission index is not reached. In view of these results several conclusions are drawn:

- The major physics involved must not have been identified correctly, or modeled correctly: a reactor cluster capable of modeling the triple flame structure could bring significant improvements, but it may not be realistic to try designing this particular flame front structure with reactor networks. Anyway it is likely that the governing physical phenomena are different whether the flame is classified as near or far lifted, inducing radical changes in the flame aspect that have been reported by Fujimori et al. [59].
- Consequently the modeling process adopted may not be the most effective: trying to model two potentially very different configurations with a single reactor network architecture.
- Finally, it might also be that chemical reactor network modeling is not the most suitable modeling technique for such a system. On the one hand it accounts for detailed chemistry, which is potentially beneficial for ignition and emission prediction. But on the other hand the turbulence is not modeled and the flow pattern is only roughly discretized. It would appear that for such a system a proper modeling of both aspects is required, as well as their interaction with the chemistry.

From the experience gained during the modeling of the two other combustion systems, some additions could be made to improve this network and its simulation: in the current architecture there is no recirculation between reactors after the ignition region. The post–ignition region and the exhaust region could then be modeled better as Plug Flow Reactors (PFR) (see appendix A) with varying section (post–ignition region) and constant cross section (exhaust region) with side entries for heat losses. This would impact the iteration process: first the simulation of of the premixing and ignition regions until steady–state, then the simulation of the PFR regions. The simulation time gain would be significant, but most of all the resolution problem of the post–ignition region would disappear. Differences with the actual predictions are foreseen, however it is not expected that these additions would yield the expected trend, the preceding conclusions still applying.

4

Emission modeling of flameless furnaces

4.1. Introduction

The first industrial applications of flameless combustion were in furnaces. This type of combustion system looks — a priori — more friendly as to CRN modeling, displaying large volumes of uniform temperature and concentrations (the ”well-stirred” characteristic mentioned in 2.3). Moreover the physical principles behind the flameless burner technologies developed are well–defined: postponing the mixing of the reactants so they have enough time to be diluted with recirculating hot flue gas, entrained thanks to high momentum injection.

The second combustion system proposed for emission modeling in this work is the multiple burner flameless furnace of the Process & Energy department of TU Delft. This furnace was investigated at length experimentally and numerically by Danon [5]. As could be expected, a rather complex flow field is induced by the particular configuration of this furnace which does not make it the ideal candidate for CRN modeling. However one particular publication from Mancini, Schwöppe, Weber and Orsino [62] reports a successful CRN modeling on a furnace with a much simpler flow configuration, the International Flame Reasearch Foundation (IFRF) flameless furnace. It is a semi–industrial scale furnace constituted by a simple rectangle parallelepipedic combustion chamber $(6.25m \times 2m \times 2m)$, equipped with a single flameless burner at one extremity, the exhaust being situated at the opposite length. Based on experiments and CFD simulations reported in previous papers [42][43][63] they successfully used a reactor network to retrieve experimental results which general architecture is displayed in figure 4.1.

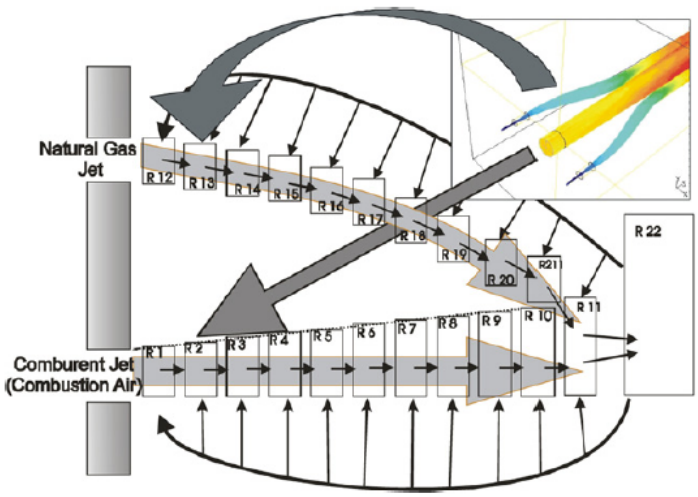

Figure 4.1: The reactor network built by Mancini [62]

The philosophy behind this architecture is the focus on the most critical phenomenon of flameless combustion technology in furnaces: the fuel and oxidizer jets evolution before they mix and ignite. The comburant jets issuing from the burner are spatially discretized using series of PSRs in order to capture their structure while the whole furnace volume is represented by a single reactor, taking the ”well–stirred” characteristic to the extreme.

As their results emphasized, the key to an accurate prediction of both jets structures is an accurate modeling of the entrainment of recirculating flue gases into the jets. To build this network, Mancini et al. used previous CFD studies and experimental measurements to determine the reactors volumes and the intensity of the recirculation in each jet reactor. Unfortunately such measurements are not available on the target furnace. And even if they were, for a more general purpose like calculating the emissions during the design of a new furnace, it would be impossible to conduct experiments and a lot of work and time to perform CFD studies. The objective of the work in this chapter is to find a way to get rid of the CFD/experimental dependence of Mancini's reactor network so that it could be used for fast and accurate prediction of emissions from any flameless furnace. This will require the development of analytical sub–models capable of representing the major physical phenomena involved. An extensive review on flameless combustion and systems operated under flameless conditions already allowed to identify key aspects for the modeling. In order to implement a reactor network emulating a flameless furnace using a SJ/WJ burner configuration, an accurate modeling of the entrainment of both jets before they mix together and of the distance from the burner at which they mix is compulsory. It also appears that for systems operated under flameless conditions, heat losses to the surroundings have to be accounted for since they participate in the overall temperature decrease compared to conventional firing. To answer these questions, some additional literature is necessary.

4.2. Additional literature

Finding an accurate enough jet entrainment model is one challenge, but it will be simplified by the knowledge of published entrainment models which have proven their worth in subsequent studies despite being simplistic (at least for the Ricou & Spalding model). Chapter 2 makes a small review of published entrainment models.

A real interest in predicting the evolution of jets in a SJ/WJ configuration and their trajectories appeared along with the emergence of flameless combustion and the development of new burner technologies. The first methodically derived model is the work of Grandmaison, Yimer, Becker and Sobiesiak [64] as part of the development of the CGRI burner (see section 2.3). They introduced a model to predict the curving trajectory of a ”weak jet” under the influence of a ”strong jet”, with a momentum ratio $\frac{\dot{G}_{weak}}{\dot{G}_{strong}} \ll 1$ so that the strong jet does not bend, an approximation that greatly simplifies the model and which is verified in experiments [65]. Their predictions are valid only until the merging point of the 2 jets. Since then, it has been often compared with experimental or numerical data [5][20][66][67] — where its accuracy is overall good — or used as a tool to analyze numerical and experimental results [49][56][68][69]. This model will be referred to as the ”SJ/WJ model” in the remaining of the thesis.

More than 10 years later, Lee [70] derived a 3D SJ/WJ physical model which was successfully used to predict the WJ trajectory over a wide range of flow conditions. It also allowed the author to identify important design/operation factors for such a system. However the system of Ordinary Differential Equations (ODE) he derived to describe the evolution of a pair of jets is particularly heavy, 16 ODEs, 7 of them coupled.

Finally, even more recently, Faghani and Rogak [71] derived a 2D phenomenological model of two circular turbulent jets which aims at predicting both trajectories and velocity field of multiple interacting jets for a wide range of parameters: injection momentum ratio, injection angles, port diameters and spacing. Their model is based on a combination of momentum balance for circular jets and an experimentally based correlation: the Ricou & Spalding entrainment model. The derived ”Bending Model” consists in a much simpler system of 2 coupled ODEs for the trajectories prediction, for a pair of jets. It is also not limited to a SJ/WJ configuration and can be tuned easily in case of a multiple coplanar jets configuration. This model possesses undeniable qualities: it is simple, more general than the SJ/WJ model, its implementation is simple and is executed almost instantly, but most of all the reported results are of good quality. For these reasons it is a good candidate to be used in the reactor network designed in this chapter as a sub–model for the jets convergence point prediction.

4.3. The ”Bending Model”

4.3.1. Setup and equations

The Bending Model is derived for a dual–hole setup but is easily applicable to more than two jets provided minor modifications to the system of equations, a capability that will be used. A sketch of the configuration is displayed figure 4.2.

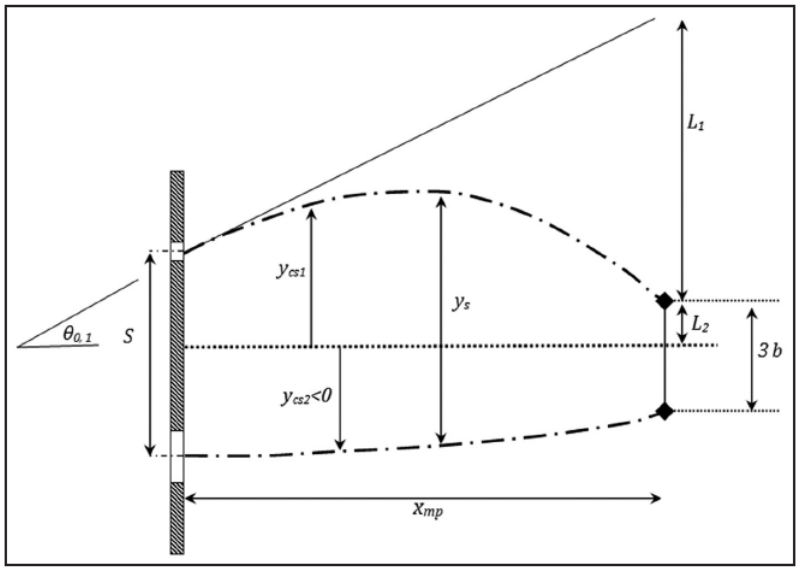

Figure 4.2: Parametrization of the Bending Model dual–hole configuration

Three major assumptions are made:

- the neighboring jet (1) does not change the entrainment of the main jet (2) significantly ;
- the lateral force on the neighboring jet is only due to the main jet entrainment, inducing a radial velocity pattern ;
- the entrainment rate of Ricou & Spalding is used:

$$\frac{d\dot{m}}{dx} = K_e\sqrt{\rho_\infty \dot{G}_0}$$

with $K_e = 0.284$.

Additionally, to derive the final equation system Faghani and Rogak assumed that $\theta(x)$ (the local angle of the trajectory with the horizontal) is not a strong function of x and that $\theta(x)$ is ”small”, allowing them to use Taylor series along with the following slope approximation:

$$\frac{dy_{cs}}{dx} = \tan(\theta) \approx \theta \tag{4.1}$$

A lack of information about the extent of the use of this approximation in the integration process introduced the necessity to investigate in total five possibilities to derive, integrate and implement the Bending Model (appendix C).

Performing momentum balances on a small volume and formulating the external forces on it in terms of main jet entrainment, the following system of equations is obtained by the authors:

$$\begin{cases} \dfrac{d^2y_{cs,1}}{dx^2} & = -\dfrac{y_s+R}{y_s}\dfrac{K_e^2}{2\pi y_s}\dfrac{\cos^2(\theta_1)}{\cos^2(\theta_{0,1})}\sqrt{\dfrac{\dot{G}_{0,2}}{\dot{G}_{0,1}}} \\ \dfrac{d^2y_{cs,2}}{dx^2} & = +\dfrac{y_s+R}{y_s}\dfrac{K_e^2}{2\pi y_s}\dfrac{\cos^2(\theta_2)}{\cos^2(\theta_{0,2})}\sqrt{\dfrac{\dot{G}_{0,1}}{\dot{G}_{0,2}}} \end{cases} \tag{4.2}$$

with:

- $R = K_b b = 1.5b$ the actual radius of the jet ;
- b the half velocity radius: $b = K_r x = 0.085x$;
- $y_s = y_{cs,1} - y_{cs,2}$.

It is worth mentioning that the Bending Model accounts for jet entrainment (via K_e) and jet spreading (via K_r and K_b). Finally, contrary to the SJ/WJ model, only one equation covers the whole trajectory of one jet instead of two: one before the trajectory's extremum and one after.

This system rules the evolution of $y_{cs,i}$ until the "merging point", defined by the authors as the axial position at which $y_s = y_{cs,1} - y_{cs,2} = 2R = 3b$.

4.3.2. The 3 jets problem

One of the pros of working with the Bending Model is its easy adaptability to a more complex setup, in this case a system of 3 coplanar jets, constituted of one central strong jet (2) and 2 weak jets (1) and (3) located one on each side, not necessarily symmetrically (see figure 4.3). This kind of arrangement is the general configuration of the burners in the works of Mancini et al. [62] or Lupant [20] that will be used to validate the network sub–models as well as the network predictions.

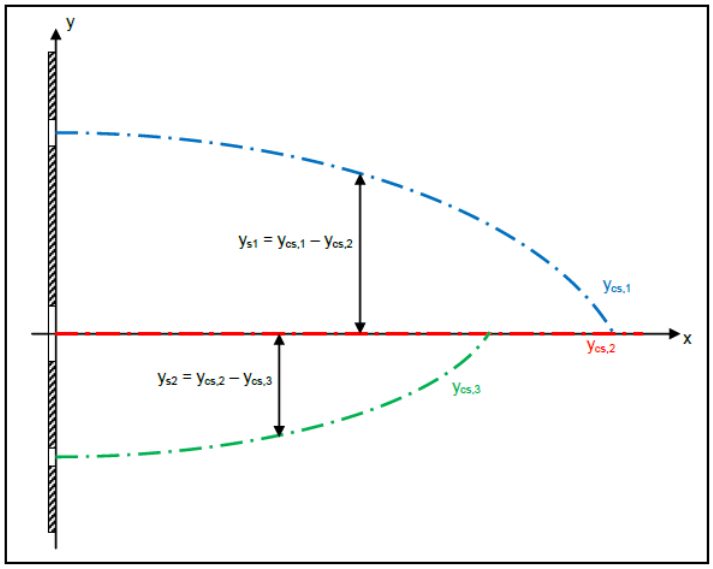

Figure 4.3: Parametrization of the Bending Model 3 jets configuration

Following the same reasoning as for the dual–hole setup, a third equation ruling the evolution of the third jet is added, *with the reasonable assumption that each weak jet is only influenced by the central strong jet.* The origin of the y–coordinate is now taken on the centerline of the strong jet. This coordinate system combined with the assumption that the strong jet evolves without any exterior influence from either weak jet greatly simplifies the problem. The differential equation steering the central strong jet trajectory is very simple and comes down to:

$$y_{cs,2} = cste = 0 \quad \forall x \tag{4.3}$$

And the final cluster of ODEs for the 3 jets configuration becomes:

$$\begin{cases} \dfrac{d^2 y_{cs,1}}{dx^2} & = -\dfrac{y_{s,1} + R}{y_{s,1}} \dfrac{K_e^2}{2\pi y_{s,1}} \dfrac{\cos^2(\theta_1)}{\cos^2(\theta_{0,1})} \sqrt{\dfrac{\dot{G}_{0,2}}{\dot{G}_{0,1}}} \\ y_{cs,2} & = 0 \quad \forall x \\ \dfrac{d^2 y_{cs,3}}{dx^2} & = +\dfrac{y_{s,2} + R}{y_{s,2}} \dfrac{K_e^2}{2\pi y_{s,2}} \dfrac{\cos^2(\theta_3)}{\cos^2(\theta_{0,3})} \sqrt{\dfrac{\dot{G}_{0,2}}{\dot{G}_{0,3}}} \end{cases} \tag{4.4}$$

4.3.3. Implementation of the dual–hole configuration

To integrate the system 4.2, a built–in Python solver able to handle both stiff and non–stiff ODE and DAE (Differential Algebraic Equation) systems is used: SciPy.integrate.odeint. This function is designed to integrate systems of 1st order ODEs, but system 4.2 is a coupled system of two 2nd order non–linear ODEs. It is well–known that a 2nd order ODE is equivalent to a system of two 1st order ODEs: a mathematical transformation prior to integration is needed. The final system will be composed of 4 coupled 1st order ODEs.

Appendix C reports in detail the investigation for the implementation of the final system of interest. The variable change

$$Z = (z_0, z_1, z_2, z_3) = \left(y_{cs,1}, \frac{dy_{cs,1}}{dx}, y_{cs,2}, \frac{dy_{cs,2}}{dx} \right)$$

and the trigonometric transformation

$$\cos^2(\theta) = \frac{1}{1 + \tan^2(\theta)} = \frac{1}{1 + \left(\frac{dy_{cs}}{dx}\right)^2}$$

are used and the following system is obtained:

$$\begin{cases} \dfrac{dz_0}{dx} & = z_1 \\ \dfrac{dz_1}{dx} & = -\dfrac{z_0 - z_2 + R}{z_0 - z_2} \dfrac{K_e^2}{2\pi (z_0 - z_2)} \dfrac{1}{\cos^2(\theta_{0,1})} \sqrt{\dfrac{\dot{G}_{0,2}}{\dot{G}_{0,1}}} \dfrac{1}{1 + z_1^2} \\ \dfrac{dz_2}{dx} & = z_3 \\ \dfrac{dz_3}{dx} & = +\dfrac{z_0 - z_2 + R}{z_0 - z_2} \dfrac{K_e^2}{2\pi (z_0 - z_2)} \dfrac{1}{\cos^2(\theta_{0,2})} \sqrt{\dfrac{\dot{G}_{0,1}}{\dot{G}_{0,2}}} \dfrac{1}{1 + z_1^3} \end{cases} \tag{4.5}$$

with the initial conditions:

$$Z_0 = \left(y_{cs,1}(0), \frac{dy_{cs,1}}{dx}(0) = \tan(\theta_{0,1}), y_{cs,2}(0), \frac{dy_{cs,2}}{dx}(0) = \tan(\theta_{0,2}) \right) \tag{4.6}$$

Multiple validation steps are now needed.

1. First it is necessary to validate the implementation of this system of equations against the reported performance in [71]. The isolated SJ hypothesis will be verified as well. Also, in order to be as comprehensive as possible, the impact of the entrainment model used in the Bending Model will be studied: the entrainment model will be switched from Ricou & Spalding’s to Han & Mungal’s. This second model accounts for a near field addition that might be beneficial to the jet entrainment prediction and hence to the jet trajectories and convergence point predictions.

2. Then the predictions of this implementation of the Bending Model will be compared to the trajectories and convergence point predictions of the SJ/WJ model.

3. Finally the 3 jets configuration is similarly implemented and tested against experimental and numerical data from three different flameless setups.

4.3.4. Validation against the reported performance

As a mean to validate their model, Faghani and Rogak compared their predictions to experimental data reported by Grandmaison et al. in [64]. This implementation will be compared to both the experimental data and the predictions from Faghani and Rogak. Two configurations are tested:

- a SJ/WJ configuration with the WJ injected at $10°$ diverging, the SJ at $0°$;
- a SJ/WJ configuration with the WJ injected at $20°$ diverging, the SJ at $0°$.

The greek letter ψ is used to characterize the ratio of initial momentum rate between WJ and SJ:

$$\psi = \frac{\dot{G}_{0,WJ}}{\dot{G}_{0,SJ}}$$

S stands for the distance between the SJ and WJ centerlines. In the legends, 'Bending Model' refers to Faghani and Rogak's predictions and 'Sim.' refers to this chapter's implementation.

Isolated SJ hypothesis

The isolated SJ hypothesis is one of the main assumptions of the Bending Model, considering that the SJ develops without any influence from the WJ. In the case where the WJ influence is potentially the biggest on the SJ ($10°$ diverging injection of the WJ), it is clear that the SJ trajectory barely bends under the effect of the WJ entrainment (figure 4.4). This hypothesis is obviously all the more valid when a second WJ is present on the other side of the SJ. In order to simplify the next figures, the SJ trajectory prediction will be omitted and assumed to be a straight line.

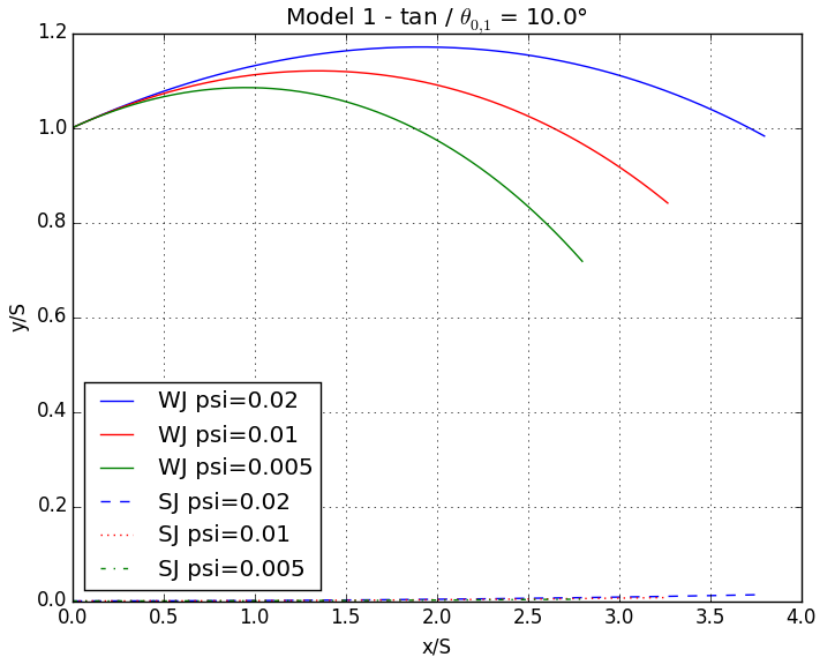

Figure 4.4: Validation of the isolated SJ hypothesis

Trajectories comparison

The trajectories predictions for $10°$ and $20°$ diverging injection are displayed in figures 4.5 and 4.6 respectively. Several features need to be highlighted:

- this implementation of the Bending Model consistently predicts more curved trajectories than what Faghani and Rogak reported for their implementation, regardless of the momentum rate ratio ψ. Appendix C reporting the detailed investigation on the integration mode shows that this is the case for all modes. The only plausible explanation for the discrepancies is then a different numerical method for the integration ;
- despite this difference, the predictions remain consistent with the experimental results and the trajectory prediction is of good quality ;

The investigation conducted in appendix C also illustrates one limit of the Bending Model. When the diverging injection angle increases, it induces bigger local angles (in absolute value) along the trajectory, in turn inducing the introduction of bigger deviations due to the use of Taylor series and the slope approximation in the derivation process. The error introduced also increases depending on the integration mode. To stay in a reasonable validity region, the Bending Model must be used with reservations and more caution when the relative injection angle between WJ and SJ diverges by more than $20°$.

Influence of the entrainment model

The Ricou & Spalding entrainment model used by the authors in the original derivation is switched to the Han & Mungal model: the only difference is that the entrainment constant K_e is now a function of x (see figure 2.9). Qualitatively, prior to any simulation, the results are expected to be very different and not as close a match with the experimental data as when the Ricou & Spalding model is used. The near–field correction makes the entrainment less intense immediately after injection which means that the WJ won't be attracted as much by the SJ. The WJ will then have the tendency to go further away from the SJ initially before finally starting to bend towards the SJ. This behaviour is confirmed by figures 4.7 and 4.8.

Although the Bending Model uses a simple jet entrainment model, it yields trajectory predictions of very good quality compared to experimental results, provided it is used in a reasonable range of injection angles.

4.3.5. Validation against the SJ/WJ model predictions

Having a way of predicting trajectories accurately is a good start because it indirectly leads to the real objective of using such a predictive model: estimating the streamwise position where the jets converge. The predictions from this implementation of the Bending Model are compared with the trajectories and convergence points predictions from the SJ/WJ model. However, two major changes have to be implemented to have consistency between both predictive models:

- in the SJ/WJ model the convergence point criteria is different that the one used by Faghani & Rogak in their publication. Grandmaison et al. define the streamwise position of convergence as the point where the centerline of the WJ hits the external envelope of the central SJ ;
- the SJ/WJ model uses equation 2.33 to define the spreading law and external radius of a jet. In the Bending Model, the equivalent to the spreading coefficient C_s is the product $K_b K_r$ which reported value corresponds to an opening semi–angle of $7°$. In order to have consistency, the product $K_b K_r$ is set to the same value as in equation 2.33 corresponding to an opening semi–angle of $11°$.

Finally both jets are considered to be injected from point sources, physically meaning that both ports diameters are very small compared to the port spacing.

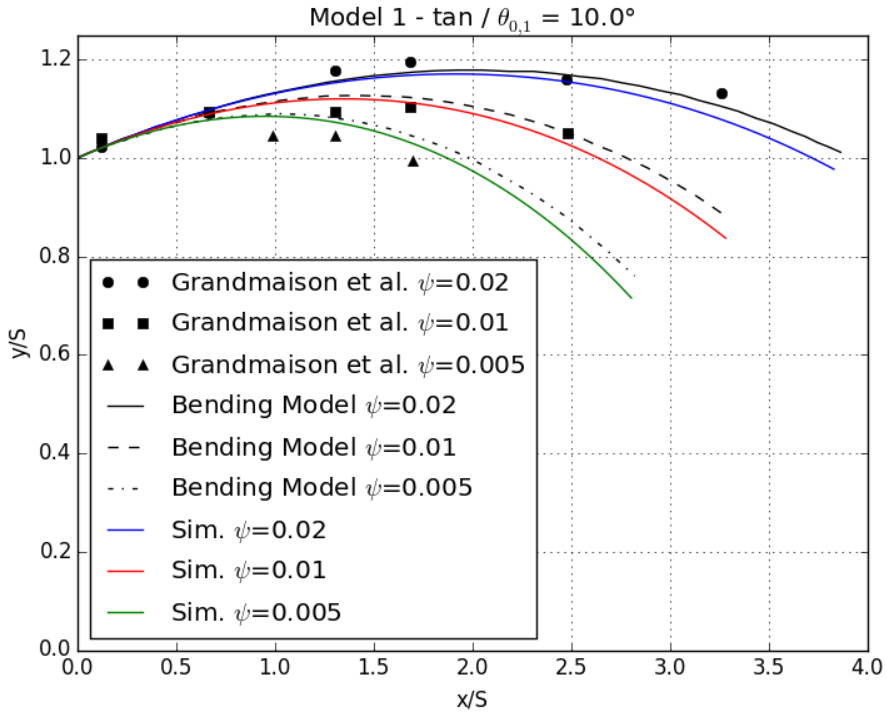

Figure 4.5: Trajectories predictions for $10°$ diverging injection

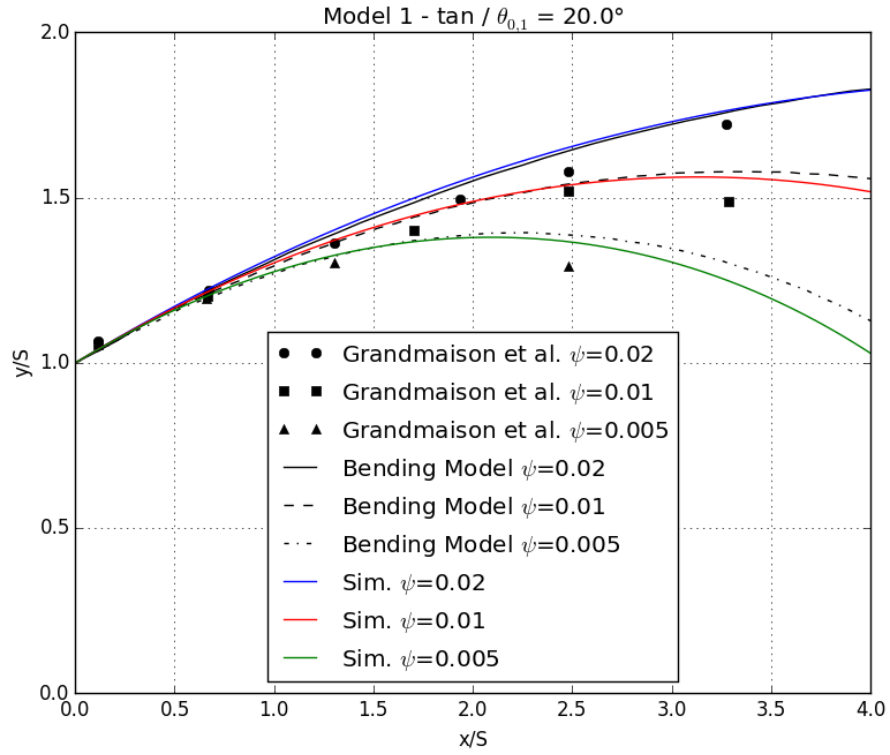

Figure 4.6: Trajectories predictions for $20°$ diverging injection

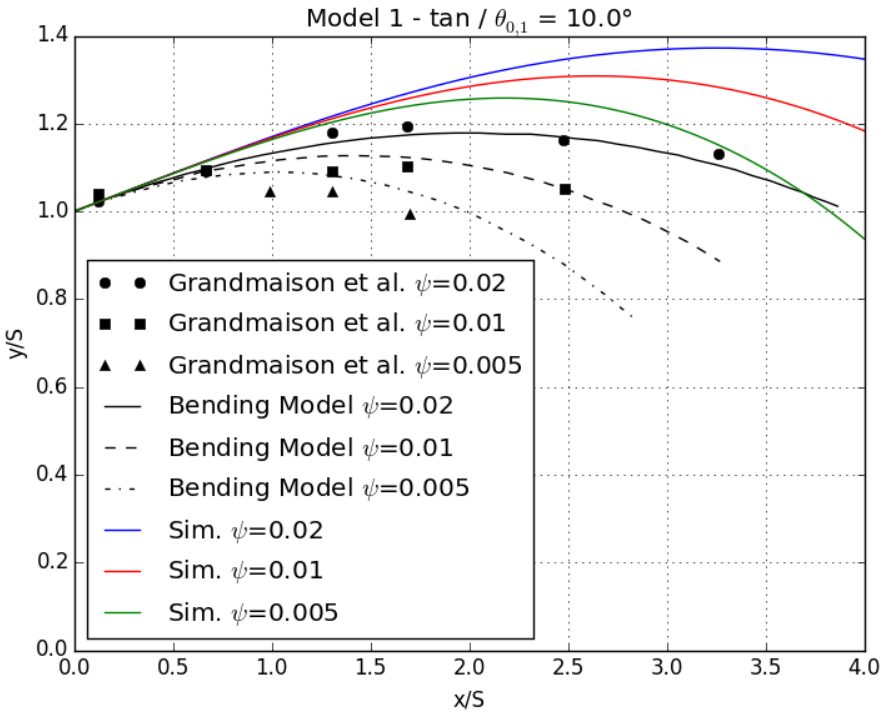

Figure 4.7: Trajectories predictions for $10°$ diverging injection with modified entrainment

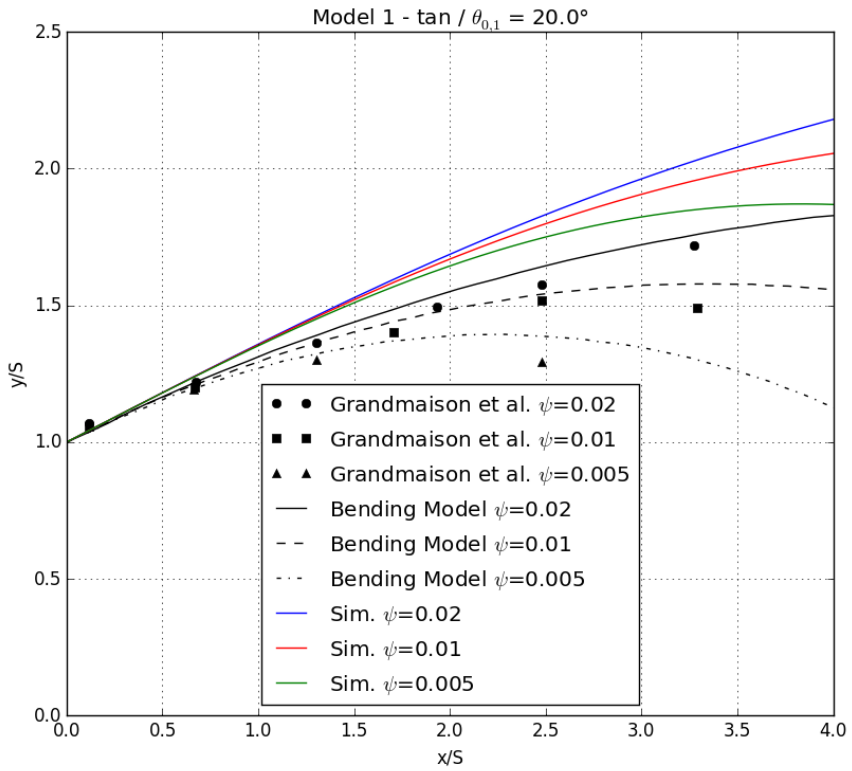

Figure 4.8: Trajectories predictions for $20°$ diverging injection with modified entrainment

Trajectory prediction comparison

Implementing these two modifications, trajectory predictions from the Bending Model were made again for WJ injection angle ranging from $0°$ to $40°$ diverging, the SJ injection angle remaining $0°$ in all cases. The results are presented on a dimensionless form: $\eta = \frac{y}{s}$ and $\xi = \frac{x}{s}$ with S the injection port spacing. The dashed line represents the calculated external envelope of the SJ. The black lines are the predictions from the SJ/WJ model, while the color lines are predictions obtained with the Bending Model. The prediction are made for a constant momentum rate ratio $\psi = 0.02$.

Figure 4.9a is obtained using the selected integration mode (appendix C), but the trends are the same for all integration modes for angles $0°$ to $20°$: the Bending Model consistently predicts more curved trajectories than the SJ/WJ model. If this case is any indication of a trend, it is likely that the trajectories at different ψ would show the same behaviour, consequently underpredicting the convergence point. At larger angles, the different integration modes have noticeable consequences and the predicted trajectories start to show significant discrepancies. $30°$ and $40°$ angles are outside the confidence region of the Bending Model validity mentioned previously. This difference in trajectory prediction inevitably induce different convergence point predictions.

Convergence point prediction comparison

For the same range of injection angles, sets of simulations are launched with varying ψ ranging from 0.004 to 0.1. The dimensionless axial position of the convergence point ξ_c is plotted against the momentum rate ratio ψ with the WJ injection angle as a parameter in figure 4.9b.

As expected, the Bending Model underpredicts the streamwise position of the convergence point, with increasing deviation from the SJ/WJ model when the WJ injection angle increases as well as when ψ increases (the WJ is getting "stronger"). At small injection angles ($0°$ and $10°$) the difference between both models is insignificant, starts to be not negligible at $20°$ and high ψ, while there is a significant deviation in predictions at $30°$ and $40°$. If the SJ/WJ model were to be taken as reference, this figure illustrates the limits of the Bending Model at high angles.

This set of simulations allowed to select the preferred integration mode of the Bending Model (appendix C). It also confirms the validity range proposed: it can be used with confidence up to diverging injection angles of $20°$, even $10°$ if the momentum rate ratio is high. On the contrary for converging injection angles of $20°$, the merging will occur closer to the ejection plane and the Bending Model should predict the convergence point with accuracy.

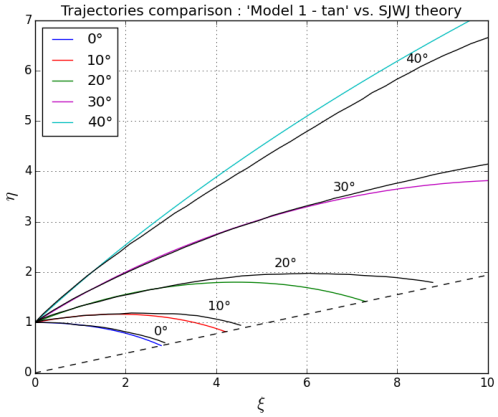

(a) Trajectory predictions

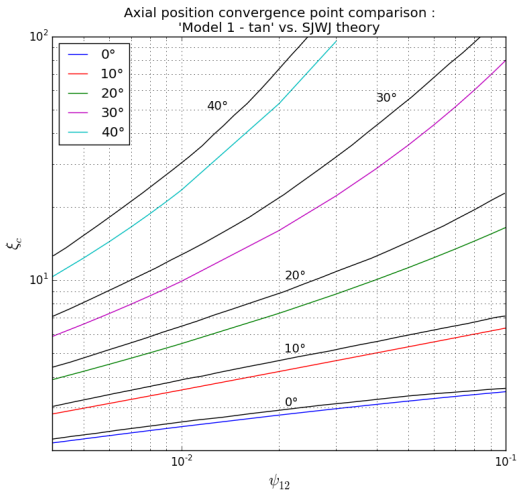

(b) Convergence point predictions

Figure 4.9: Comparison between predictions from the implemented Bending Model and the SJ/WJ model (adapted from [64])

4.3.6. Final validation: the IFRF furnace

Now that the Bending Model (dual–hole configuration) has proven its worth, the 3 jets configuration is implemented using the guidelines of the preferred integration mode that has been selected using the dual–hole configuration. The Bending Model performance under a 3 jets configuration is assessed comparing the convergence point prediction with experimental and numerical data obtained on three different flameless furnace setups. The first of them is the semi–industrial furnace of the IFRF $(580\ kW)$, the same on which Mancini et al. based their work [62]. Since the prototype reactor network designed in this chapter is largely inspired by them, it is only fitting to test one of the network's key components against this experimental setup. The burner characteristics are shown in figure 4.10: the configuration is in the recommended confidence window for the Bending Model (parallel injection). An estimate of the convergence point streamwise position corresponding to the inlet conditions is given by Mancini et al.: $x_c = 0.70m$. It has to be noted though that this value is quite a rough estimate determined based on experimental observations. Nonetheless, it will be used as the reference value for this furnace under the specified conditions.

Additionally, the Bending Model needs to be modified again for this simulation. The hypothesis considering the jets to be issued from point sources does not hold with the burner characteristics: $\emptyset_{WJ} = 1\ cm$ but $\emptyset_{SJ} = 12.4\ cm$ while the port spacing is $d_{12} = 28.0\ cm$. The SJ radius can't be approximated to issue from the origin any more. This is confirmed by a first run of the model not implementing this correction. It was then modified so that the SJ radius law originates at the SJ port extremity. The prediction is of excellent quality (figure 4.11).

4.3.7. Final validation: the University of Mons furnace

The flameless furnace installation at the University of Mons is a significantly scaled down version of the IFRF furnace. Also its (single) burner configuration is different (figure 4.12): the central strong jet is still injected at $0°$, but both weak jets are injected with converging angles of $11°$ for one and $16°$ for the other [20]. This difference was not designed purposely but it actually provides the possibility to test the predictive model with converging angles, and with different injection angles for each WJ. Lupant also used the SJ/WJ theory of Grandmaison et al. to analyze her results. The experimental trajectories of the weak fuel jets are extracted using the fuel concentration maxima on each plane parallel to the injection plane, the same criterion used in a previous extensive experimental and numerical investigation of the SJ/WJ problem [65]. The results for two different ψ (two different excess air, 10% and 20%) are reported and are then simulated. All the predictions are once again of very good quality (figures 4.13 and 4.14). There is no difference in the experimentally determined values between both excess air conditions, however the model predicts a slightly earlier merging point for 10% excess air, as could have been expected: the weak fuel jets keep the same injection momentum rate while the strong oxidizer jet injection momentum rate decreases.

4.3.8. Final validation: the University of Adelaïde furnace

This furnace was investigated experimentally and numerically at length by Szegö [8]. The dimensions of the furnace are of the same order of magnitude as the previous one. The nozzle configuration however is different from both previous burners: the furnace exhaust is constituted of several ports (red) inserted between a central oxidizer port (blue) and the surrounding fuel ports (black) (see figure 4.15). In [67] the same furnace is investigated, but with an additional degree of freedom for the fuel injection angle (not used for this validation). The convergence point axial position for two different burner configurations, but both with parallel injection, are extracted from numerical simulations. The convergence point criterion used by Mi et al. is once again different than the one used so far: the convergence point axial position is defined as the minimum axial position z at which only the central peak of the axial velocity profile exists across the central planes (yz and xz with the convention of figure 4.15). A wide range of momentum ratio is covered in different runs by varying the fuel ports diameter (case 7), the oxidizer port diameter (case 6), the overall equivalence ratio (case 4), the temperature of the preheated air (case 5), or the dilution of the fuel stream with inert gases (CO_2, N_2) (cases 2, 3 and 8). The results are displayed in figure 4.16 and compared to the SJ/WJ model predictions (made by the authors) and the Bending Model predictions for parallel injection. Despite some scatter, different convergence point criteria and CFD related issues, both predictive models provide a good approximation of the general trend extracted from CFD simulations.

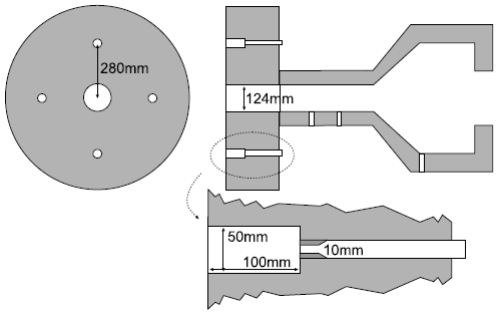

Figure 4.10: NFK regenerative burner of the IFRF furnace (from [72])

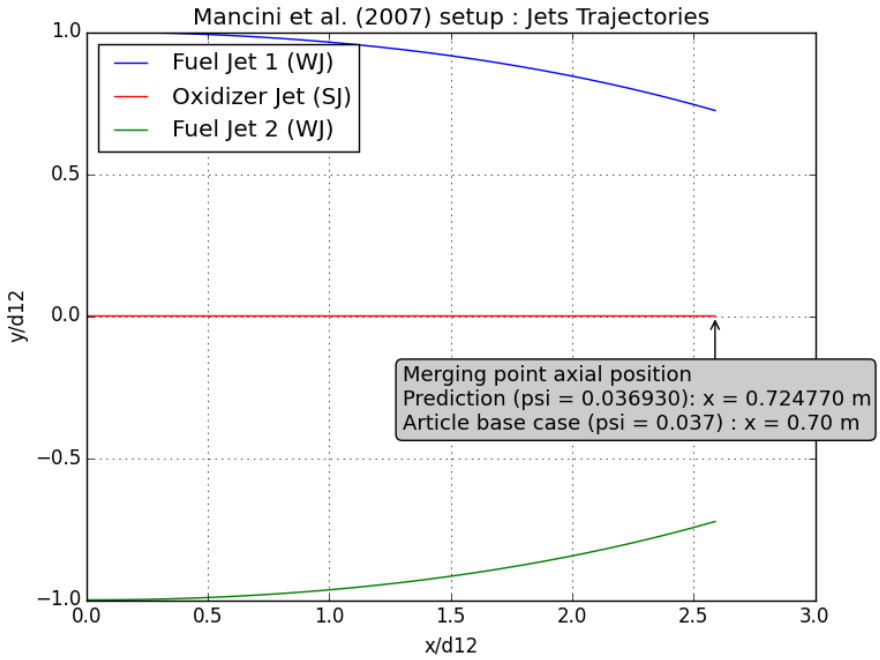

Figure 4.11: Convergence point prediction for the IFRF furnace

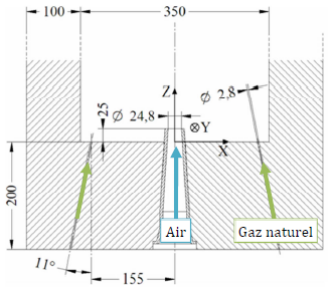

Figure 4.12: Vertical cut of the Mons furnace base in the injectors plane (from [20])

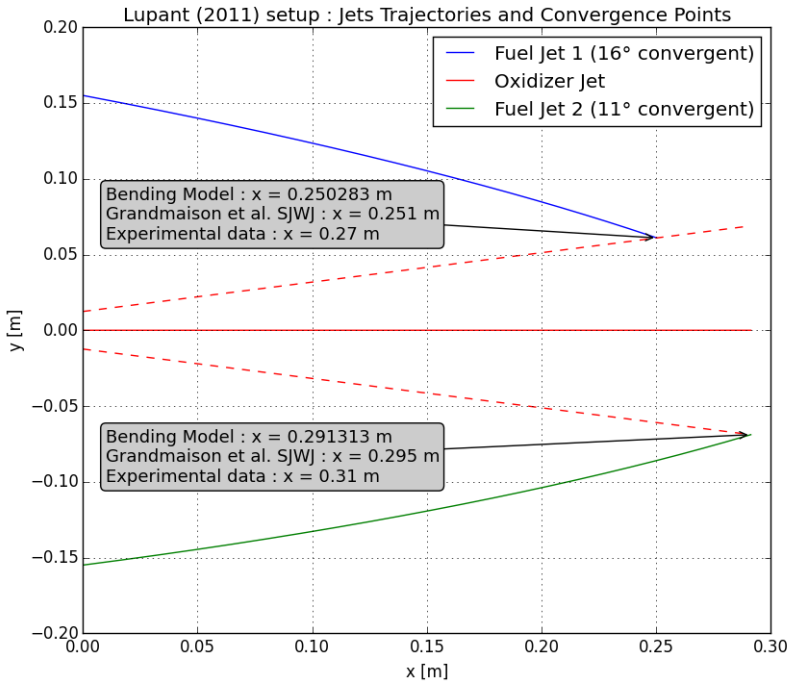

Figure 4.13: Convergence point prediction for the Mons furnace (10% excess air)

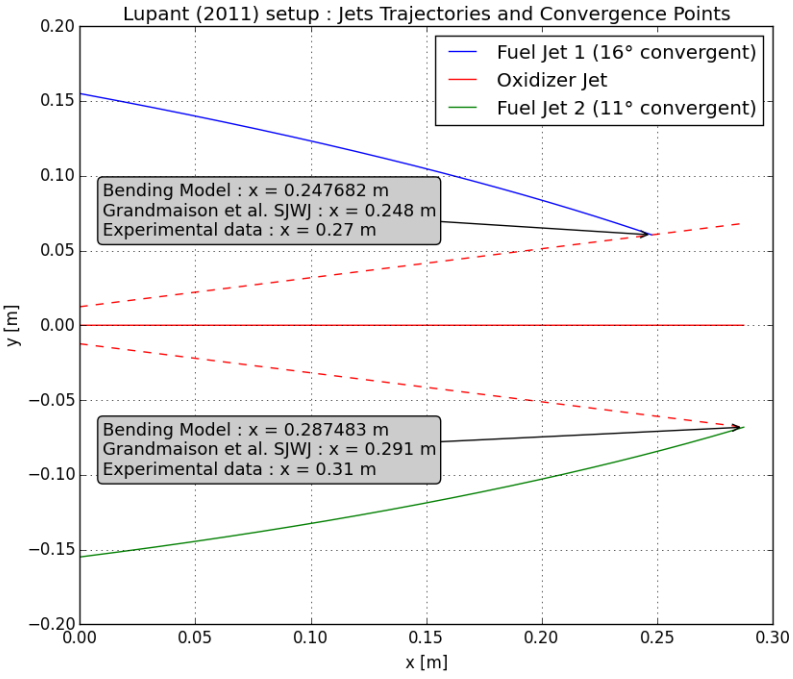

Figure 4.14: Convergence point prediction for the Mons furnace (20% excess air)

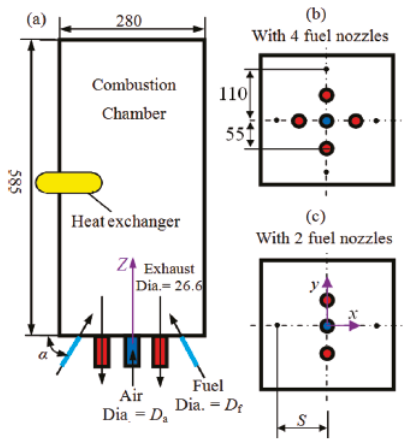

Figure 4.15: Adelaïde furnace dimensions (a) and two burner configurations (b) (from [67])

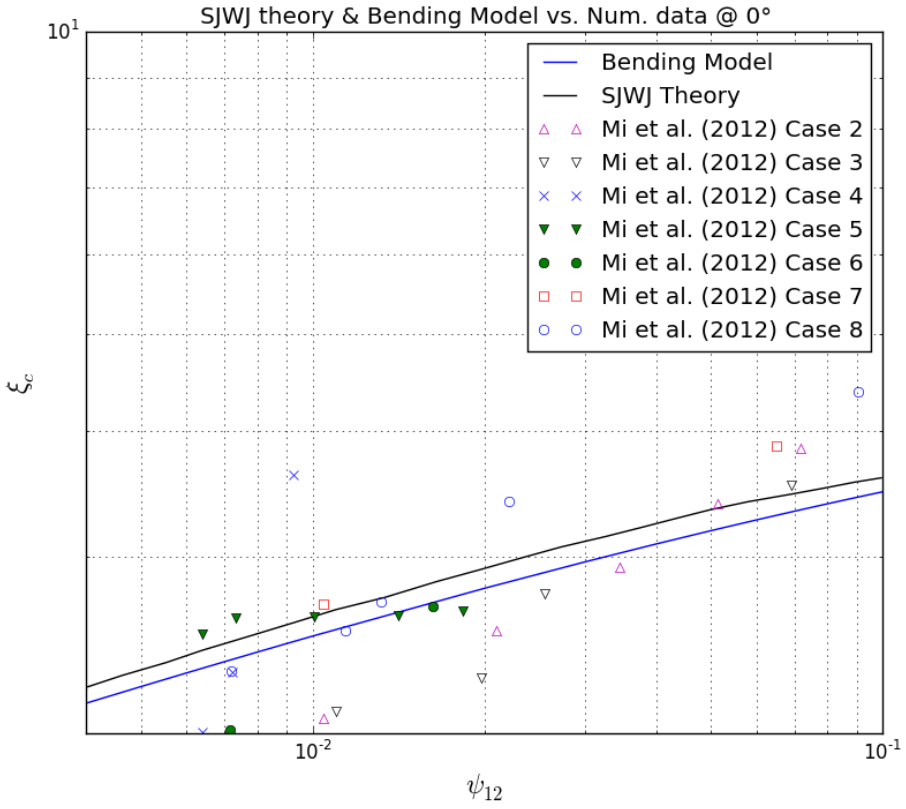

Figure 4.16: Convergence point prediction comparison for the Adelaïde furnace (adapted from [67])

4.3.9. Conclusion

As a final note to the development of this predictive model, it is safe to conclude that the Bending Model (implemented according to the preferred integration mode) can be used as a reliable component of the reactor network designed in this chapter. It has the potential to replace experimental or CFD determination of the convergence point, providing almost instant estimates: it won't hinder the fast emission prediction objective that was set.

4.4. Jet entrainment modeling in a SJ/WJ configuration

In the introduction, emphasis was put on one conclusion of Mancini and his coworkers: an accurate prediction of the amount of recirculated gases entrained into the jets is necessary to obtain a good prediction of the jets structure. In parallel, a sufficient inertization/vitiation is a key parameter of flameless combustion. A proper modeling of this phenomenon requires a combined accurate prediction of the position at which the jets mix together and of the amount of hot gases entrained. The former has been largely investigated in the previous section. The latter is the purpose of this section: designing an accurate entrainment model for jets issuing from a burner in a SJ/WJ configuration. It will be achieved by modifying an already existing entrainment model using the jets data (trajectory and expansion) calculated in the Bending Model. This way, only analytical expressions are involved and this customized model will meet the modeling specifications of the reactor network designed in this chapter (no experimental or CFD dependence).

4.4.1. Mutual "shielding" of the jets

An obvious choice of entrainment model to start the customization is the Ricou & Spalding model, used in the trajectories prediction. The modifications are implemented following the comparison between this analytical model to the entrainment data reported by Mancini et al. [62]. They determined the evolution of the entrainment along both SJ and WJ experimentally and from CFD simulations of their setup. The authors underlined the fact that both methods were consistent with each other and reasonably accurate when determining the SJ entrainment (10% error for experimental data). However as far as the WJ entrainment is concerned, the CFD notably underpredicts it (consequence of the turbulence model selected) while it is more difficult to extract the experimental data reliably (30% error is estimated). [62] reports all the data needed to compute the Ricou & Spalding prediction, which is plotted on top of the reported entrainment until a distance of 80 cm (the convergence point is estimated in this study to be around 70 cm from the ejection plane) in figures 4.17 and 4.18.

This comparison brings a compelling result out : for both jets, **the "real" entrainment decreases along the length compared to the analytical prediction.** This phenomenon is more important on the SJ than on the WJ. One theory can then be imagined : while the WJ is gradually pulled by the SJ towards itself, each jet acts as an **"entrainment shield"** to the other. This *mutual shielding* is weak at first and grows more and more important while the WJ gets closer and closer to the SJ: from 0% at injection up to more than 25% $80cm$ further for the SJ ; and up to approximately 20% $80cm$ downstream for the WJ.

The objective is then to use the jets structure data computed in the Bending Model, namely trajectories and radius expansion, to build a *shielding factor* for each jet. This factor will be constructed using purely geometrical arguments. One hypothesis has to be made to simplify the problem: a section of the WJ by a plane parallel to the injection plane is in reality an ellipse but is considered to be a circle in the reasoning. This hypothesis is not expected to introduce a significant error compared to the error made by the authors when extracting the data. Trying to build a shielding factor can be considered as 1st order precision already, 0th order being the use of the raw Ricou & Spalding model. Introducing ellipses would introduce unnecessary and irrelevant precision.

4.4.2. Shielding factor

A criterion combining methods A and B (appendix D) is implemented hoping to combine their respective good behaviors in the second and first part of the jets. The criterion uses method B to account for shielding until method A starts to give lower entrainment predictions. From this point on, method A is used. It is expected to yield a good prediction for the SJ, and hopefully for the WJ as well. Figure 4.19 shows the Ricou & Spalding prediction modified with this criterion. A close estimate of the SJ entrainment evolution is obtained. The big discontinuity of method A is attenuated but not enough to disappear completely. However the use of method B in the first part combined with method A in the second part results in a promising overall model.

As to the WJ, the implementation of the combined criterion to modify the entrainment model is not as successful (figure 4.20): it displays an increasing underestimation of the experimental data, though still within the 30% error the authors estimated. But the real problem resides in the fact that method B overpredicts shielding and its mathematical limit is hit before the calculation switches to method A. Hence the drop of the entrainment from $50\ cm$ on is still present, and to make things worse it induces

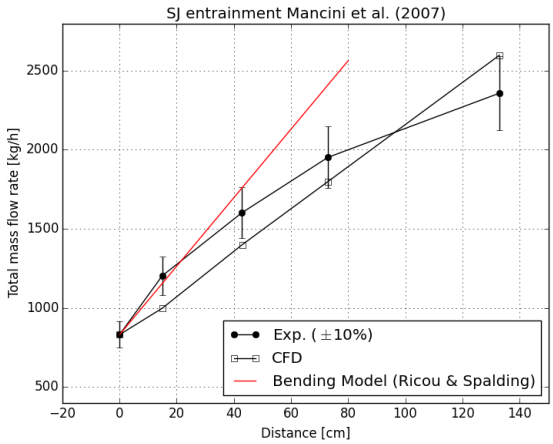

Figure 4.17: Strong jet entrainment data comparison with the Ricou & Spalding model (adapted from [62])

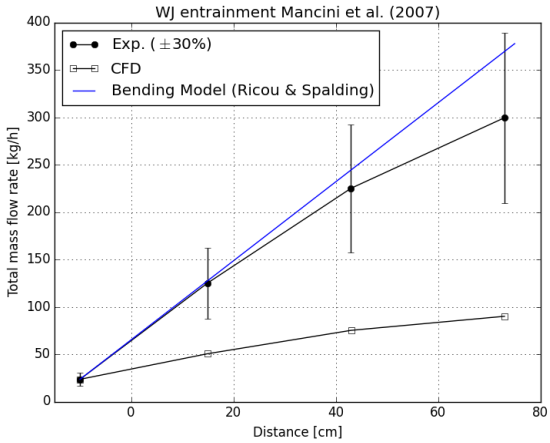

Figure 4.18: Weak jet entrainment data comparison with the Ricou & Spalding model (adapted from [62])

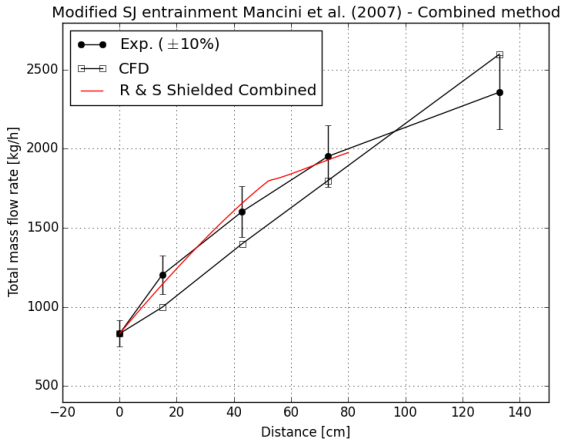

Figure 4.19: Strong jet entrainment data comparison with the modified Ricou & Spalding model (adapted from [62])

an upward step when switching to method A. It is best visible when both criteria are plotted at the same time (figure 4.21). Eventually it is not surprising that the combined method works better for the SJ than for the WJ since the geometry of the latter is more complicated because the jet is curved. It impacts the way the WJ envelope is defined : at each streamwise position the upper and lower jet extremities are attributed according to the radius expansion law. This means that in the Bending Model the trajectory is curved but not the external envelope.

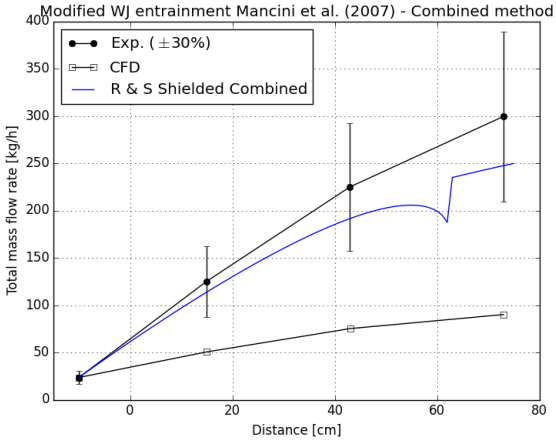

Figure 4.20: Weak jet entrainment data comparison with the modified Ricou & Spalding model (adapted from [62])

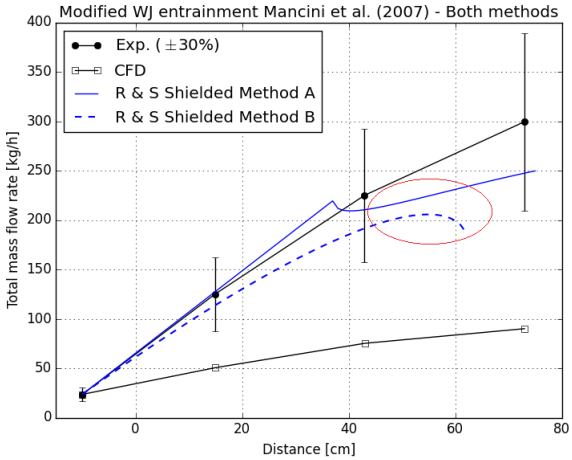

Figure 4.21: Weak jet entrainment data comparison with the Ricou & Spalding model modified with methods A and B (adapted from [62])

4.4.3. Conclusion

In view of these results, using the combined method to modify the basic entrainment model is only partly satisfactory. The combined criterion is not successful when applied to the WJ of Mancini et al. study but it yields an approximation of good quality for the SJ entrainment. It has been noted though that the predicted SJ entrainment is not perfect. Appendix D also reports evidence of non–physical entrainment behavior caused by this imperfect shielding model when used as a component of the network.

For the rest of the modeling **the combined criterion is adopted for the central strong jet entrainment modeling**, while **no shielding will be applied on the surrounding weak jets**. It will in the end come down to assess if the final emission predictions are satisfactory using this customization for the entrainment. This model will be referred to as the ”Shielded Entrainment Model” in the rest of the thesis.

4.5. CRN modeling of a flameless furnace

4.5.1. General architecture

The same general architecture as reported in [62] is used, combined with the two previously developed models. It is displayed in figure 4.22. The arrow codes are the same as in figure 3.8. In the original publication, the reactor network is specifically designed for the IFRF furnace and its symmetries have been exploited. Only one half of the furnace setup is modeled : half the total volume but more importantly concerning the burner jets interaction, one of the two weak fuel jets and half the central strong oxidizer jet.

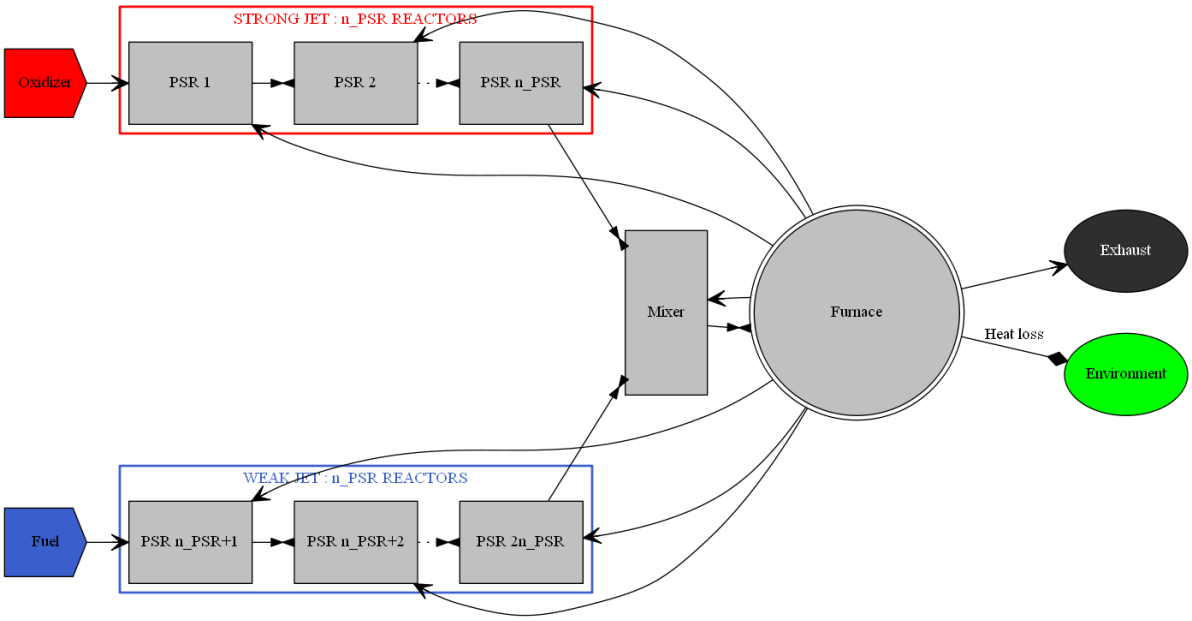

Figure 4.22: General architecture of the designed flameless furnace reactor network

The network main components are:

- 1 WJ discretized in n_{PSR} constant volume adiabatic PSRs ;
- 1 SJ discretized in n_{PSR} constant volume adiabatic PSRs as well (only half the ”real” SJ) ;
- 1 Mixer reactor: a constant volume adiabatic PSR where both jets mix and ignite ;
- 1 Furnace reactor: a constant pressure adiabatic PSR to model the rest of the (half) furnace volume. This type of PSR is used to impose the pressure in the whole system via a system of valves. However after gaining more experience with reactor networks in Cantera, it would have been easier to do so by using a constant volume PSR linked using a valve to the exhaust reservoir kept at the wanted system pressure. For more details on the valve coefficient refer to appendix A. The current design introduces unnecessary complexity.

One of the three key modeling parameters identified in the introduction is the heat loss from the system to its surroundings. In this network, a simple heat loss model is implemented: the furnace reactor temperature is kept constant, losing instantly any heat surplus to the environment reservoir. This exhaust temperature is a parameter given by the user. There is no heat exchange between reactors other than via the convective mass flows.

4.5.2. Role of the analytical submodels

Jets length

The Bending Model is the cornerstone of the network. It combines the ability to predict accurately the jets convergence point and the ability to analytically model any kind of burner with separate fuel and oxidizer injection (provided exploitable symmetries for complex burner configurations, it is a 2D model). It is the interface between the network and the user: all the parameters defining the furnace and its operating conditions are the inputs of the Bending Model, at the exception of the exhaust temperature. The streamwise position of jets convergence predicted by the Bending Model defines the jets length which is discretized into n_{PSR} reactors for each jet.

Entrainment of hot flue gas

The role of the Shielded Entrainment Model is to analytically predict the amount of hot flue gases each jet entrains before they mix together. It uses geometrical data computed in the Bending Model to construct a shielding factor which is in turn combined with the well–known Ricou & Spalding jet entrainment model. This customized jet entrainment model gives the evolution of the entrainment along the jets until they mix together. In the mixer reactor, the amount of entrained gases is determined using the mixer length parameter $x\%$: it is the sum of the calculated entrainment by the Shielded Entrainment Model for both the SJ and the WJ, over the mixer length.

Reactors volumes

In the Bending Model jet expansion is accounted for via the radius law. Each jet is represented as a cone (or a bended cone) with circular base. This provides a way of accessing the value of the volumes of the reactors used to discretize them. Each unit PSR is a cone of circular base truncated at a distance h_{PSR} from the base by a plane parallel to it. The truncated cone height is defined as:

$$h_{PSR} = \frac{convergence\ length}{n_{PSR}} \tag{4.7}$$

and the volume of this geometry is:

$$V_{PSR} = \frac{\pi h_{PSR}}{3}\left(R_1^2 + R_1 R_2 + R_2^2\right) \tag{4.8}$$

with R_1 and R_2 the respective radius of the small and large bases. This is illustrated in figure 4.23

Notes:

1. Only an insignificant error is made using this definition for a unit PSR of the WJ. The side surface is in reality slightly curved and not straight. The error introduced gets smaller when n_{PSR} is increased.
2. It is important to remind at this point that the network is built to model half the furnace. Each reactor discretizing the WJ has a volume $V_{unit}^{WJ} = V_{PSR}$ but each reactor discretizing the SJ has a volume $V_{unit}^{SJ} = \frac{V_{PSR}}{2}$.

Finally the volume of the mixer reactor has to be determined in a systematical way, as well as the volume of the furnace reactor. Even though the latter is not an input, it will serve as initialization value for the constant pressure reactor and for comparison purposes once the simulation has converged. **The final volume of the furnace reactor has to be really close to its initial value, which is the real value.** This is a consequence of using the constant pressure reactor. The suggested method to improve the pressure closure gets rid of this problem.

$$V_{furnace} = V_{total} - V_{SJ} - V_{WJ} - V_{mixer} \tag{4.9}$$

where V_{total} is the half furnace volume, V_{SJ} and V_{WJ} the total volume of the SJ and WJ, and V_{mixer} is the volume of the mixer reactor.

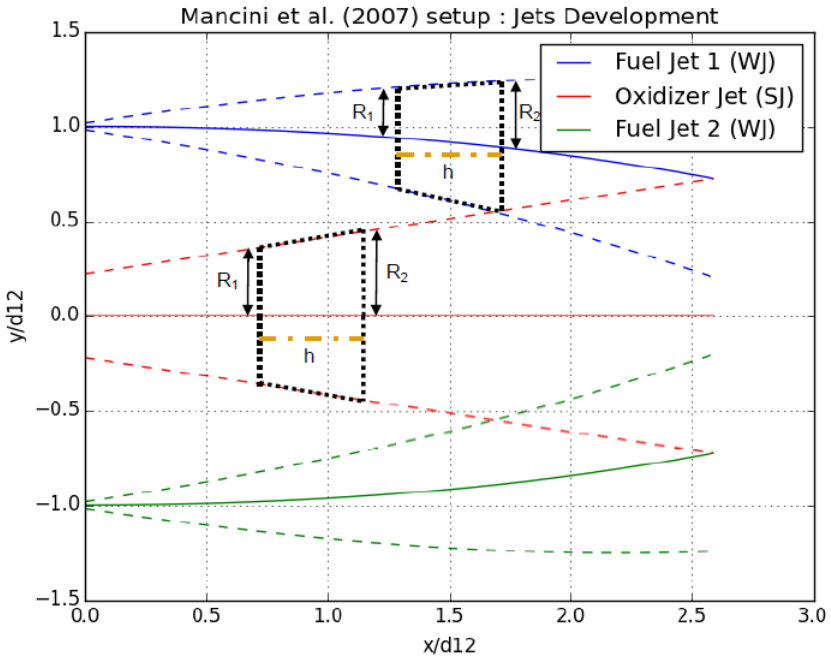

Figure 4.23: Volume determination of a unit PSR using the IFRF furnace example

To determine V_{mixer}, it is assumed that the SJ expansion is not strongly affected when mixing with the WJ [73]. As a consequence after the convergence point the single merged jet can physically be approximated just as if the SJ had continued to develop independently. The mixer reactor volume can then be determined the same way the SJ reactors were. It is then necessary to define the mixer streamwise extent h_{mixer}. It was found best to define it as a fraction of the merging distance $X_{merging}$:

$$h_{mixer} = x\% \times X_{merging} \tag{4.10}$$

The mixer length fraction $x\%$ is modifiable by the user but needs to be an educated guess. The length over which the founding hypothesis of method 2 is verified must be limited: too far and the merged jet won't behave like a jet any more, making the volume and entrainment calculations inaccurate. A fraction of $10 - 20\%$ of the merging length can be considered a good order of magnitude to start with. This parameter is not only used to obtain the volume of the mixing region, but also its entrainment. The mixer length influence on the emissions will be assessed later in the thesis. Finally the use of this parameter to access the mixer entrainment pointed out one deficiency of the Shielded Entrainment Model discussed in appendix D.

4.5.3. Parameters of particular interest

In addition to the mixer length fraction parameter $x\%$, two of the model parameters are of particular interest.

Number of reactors in the jets discretization n_{PSR}

It has a huge impact on the simulation time: each reactor adds mass, momentum, energy and species equations. For instance if the GRI 3.0 chemical mechanism is used, adding one reactor to the network adds 56 equations to the system to solve. Since one of the objectives is to build a fast emission estimator, the fewer reactors in the network the better, as long as the predictions remain of the same good quality. This simplification limit is investigated in later simulations.

Valve coefficient K_v and pressure drop

The reactor network is built with an inherent pressure drop, from the inlet reactor of both SJ and WJ ($p_{inlets} > 1.0\,atm$) to the furnace reactor ($p_{furnace} = 1.0\,atm$). This could have been a problem in the implementation of the recirculation mass flows, but luckily the mass flow controllers of Cantera maintain the flow even if the downstream pressure is greater than the upstream pressure. The documentation however warns that "this capability should be used with caution, since no account is taken for the work required to do this". This is another advantage (besides avoiding solver–related issues) of using a right setting for the valve coefficient K_v, keeping the internal Δp extremely small, completely negligible. Guidelines for the valve coefficient value are provided in appendix A.

4.5.4. Conclusion: model parameters classification

The reactor network model of a flameless furnace are gathered in table 4.1. As for the lifted jet flame system, they are classified in two categories: internal and user–defined.

USER–DEFINED		**INTERNAL**	
Furnace dimensions $[m]$:	$L \times l \times h$	Nb of reactors in jets discretization :	n_{PSR}
SJ port diameter $[m]$:	$\emptyset_{SJ}$	Mixer length fraction $[\%]$:	$x\%$
WJ port diameter $[m]$:	$\emptyset_{WJ}$	Valve coefficient $[kg/s/Pa]$:	K_v
Ports separation :	S or d_{12}	Heat transfer coefficient $[W/m^2/K]$:	U
Injection angles $[°]$:	θ_0^{SJ} and θ_0^{WJ}	Entrainment coefficient :	C_e or K_e
Inlet mass flows $[kg/s]$	ϕ_m^{SJ} and ϕ_m^{WJ}	Jet expansion rate :	C_s
Inlet flow temperatures $[K]$	T_0^{SJ} and T_0^{WJ}	Time steps $[s]$:	dt1 and dt2
Exit temperature $[K]$	T_{exit}	Maximum simulation time $[s]$:	t_{max}
Inlet flow compositions		Data time span $[s]$:	t_{data}
		Intermediate abs. tolerance :	a_tol1
		Intermediate rel. tolerance :	r_tol1
		Final abs. tolerance :	a_tol2
		Final rel. tolerance :	r_tol2

Table 4.1: Classification of the inputs of the flameless furnace model

The iteration process is articulated around two loops: a first loop of time step dt1 stopped when the selected quantities variations drop below the absolute and relative intermediate tolerances. The time step is changed to dt2 (> dt1) and the iteration resumes until the final tolerances are met. A maximum simulation time safeguard is implemented because of the loop type used. Finally the data time span parameter is the time span over which the time evolution of the desired variables will be plotted.

4.6. Prediction of emissions from the IFRF furnace

The first validation simulation has for objective to reproduce the emission and jets structure data reported in [62] for the IFRF furnace. With natural gas as fuel, the GRI 3.0 chemical mechanism is used.

4.6.1. Inputs

The model inputs are carefully gathered in tables 4.2, 4.3, 4.4 and 4.5: user–defined and internal model constants, fuel and oxidizer compositions.

USER–DEFINED			
Geometrical		**Thermodynamic**	
$L\ [m]$	6.25	$\phi_m^{SJ}\ [kg/s]$	0.2306
$l\ [m]$	2.0	$\phi_m^{WJ}\ [kg/s]$	6.528×10^{-3}
$h\ [m]$	2.0	$T_0^{SJ}\ [K]$	1573
$\emptyset_{SJ}\ [m]$	0.124	$T_0^{WJ}\ [K]$	298
$\emptyset_{WJ}\ [m]$	0.010	$T_{exit}\ [K]$	1500
$S\ [m]$	0.28	$p_{reservoir}\ [atm]$	1.0
$\theta_0^{SJ}\ [°]$	0	$p_{furnace}\ [atm]$	1.0
$\theta_0^{WJ}\ [°]$	0		

Table 4.2: User–defined parameters IFRF furnace

INTERNAL			
Model constants		**Solver constants**	
$U\ [W/m^2/K]$	100000	dt1 $[s]$	1.0×10^{-4}
$K_v\ [kg/s/Pa]$	0.1 or 10.0	dt2 $[s]$	1.0×10^{-3}
C_e	0.32	(r_tol1 ; a_tol1)	$(1.0 \times 10^{-3}\ ;\ 1.0 \times 10^{-3})$
K_e	0.284	(r_tol2 ; a_tol2)	$(1.0 \times 10^{-6}\ ;\ 1.0 \times 10^{-6})$
C_s	0.194	$t_{max}\ [s]$	400
		$t_{data}\ [s]$	60

Table 4.3: Internal parameters IFRF furnace

FUEL COMPOSITION $(\%\ vol)$	
CH_4	88.0
C_2H_6	5.0
C_3H_8	2.0
N_2	5.0

Table 4.4: Fuel composition for the IFRF furnace reactor network simulation

OXIDIZER COMPOSITION $(\% \, vol)$	
O_2	19.5
N_2	59.1
H_2O	15.0
CO_2	6.4
NO	0.0094

Table 4.5: Oxidizer composition for the IFRF furnace reactor network simulation

The oxidizer stream contains the usual inert gases resulting from combustion (H_2O and CO_2) as well as traces of NO $(94 \; ppmv, \; wet)$. In the IFRF installation the oxidizer stream is heated through pre–combustion followed by injection of O_2 in the vitiated stream to maintain its concentration more or less to atmospheric level. All this happens before injection in the flameless chamber.

4.6.2. Simulation cases

The purpose of this validation case is to simulate the operating point of the IFRF furnace reported in [62]. The influence of two critical parameters is also investigated: n_{PSR} and $x\%$, to investigate respectively the simplification limit and the influence of the mixer volume on the emissions. The simulation cases are gathered in table 4.6. For the operating point simulation, a 5–reactor discretization of the jets is chosen instead of 10 reactors like the original publication because of the prohibitive simulation time for a 22–reactor network. All the simulations are performed on a 6 years old notebook under Seven, equipped with a Intel®Core™i3 CPU oscillating at 2.27GHz and with 3.79Gb RAM: it is by no means a supercomputer. With this configuration the base case simulation time (CPU time) is already $13h$. It is a good incentive to investigate the simplification limit.

SIMULATIONS			
Case n°	n_{PSR}	$x\%$ [%]	$K_v \, [kg/s/Pa]$
1 (base case)	5	10.0	10.0
2	5	20.0	10.0
3	5	15.0	0.1
4	2	15.0	0.1
5	1	20.0	0.1
6	4	10.0	0.1
7	4	20.0	0.1

Table 4.6: Simulation cases IFRF furnace

4.6.3. Base case results

Emissions

The emission predictions obtained are compared with experimental and numerical data reported in [62]: experimental measurements from [42] and predictions from the network using experimental entrainment data from [62]. The peak temperature in the network corresponds to the mixer reactor temperature.

	Measurements [42]	Reactor network [62]	Predictions base case
$T_{exit}\,[K]$	1493	1489	1500
$T_{peak}\,[K]$	1808	1840	1876
$NO\ exit\ [ppmvd]$	140	135	169
$CO\ exit\ [ppmvd]$	0	13	27

Table 4.7: Emission prediction comparison for the IFRF furnace

The predictions from the designed network are conservative for both NO and CO, respectively:

- $+20.7\%$ and $+25.2\%$ for the NO exit concentration on dry basis ;
- $+107.7\%$ for the CO exit concentration on dry basis between both networks. No CO emissions were detected in the measurements: the concentration was most probably below the detection threshold, which value was not reported.

These deviations on dry basis make the argument that the designed analytical network may not be an accurate physical model. The absolute deviations make the opposite argument. Although the experimental measurement errors for the emission concentrations were not reported – making it hard to properly conclude – the designed network overpredicts NO emissions by only $30\ ppmvd$ compared to measurements. In terms of net NO production, instrumentation detected a marginal increase ($\approx 5-10\ ppmvw$) while the designed network predicts a $24\ ppmvw$ increase. The difference in NO emissions can be explained by:

- (unreported) experimental measurement error ;
- mostly because of the higher peak temperature obtained in the designed network: at this level of high temperatures (around the thermal pathway activation threshold) even a marginal increase of $70\ K$ is significant. The possible causes of the peak temperature overprediction are tackled in the jet temperature structure analysis below.

Concerning the CO exit concentration difference, no comparison is possible with experiments, but the higher concentration predicted by the designed network might be due to a shorter residence time in the high temperature region (mixer reactor) than for Mancini's network. This is related to the influence of $x\%$ and will be confirmed in the parametric study.

All in all, the designed reactor network seems to give predictions of good quality, validating the analytical approach taken.

Compositions

The major species concentrations in the exhaust gas are gathered in table 4.8. The experimental data reported in [42] is taken as reference. However, the fuel composition used is slightly different compared to the reported composition in [42]: it can explain the slight mismatch in exit compositions. Accounting for this difference, the exhaust compositions are consistent.

The "official" fuel composition used during the experiments is reported in table 4.9. It contains high hydrocarbons not possible to account for with the GRI 3.0 mechanism. The simplified fuel composition used also does not contain neither CO_2 nor $O_2 + Ar$.

Jets structure

Further insight in the validity of the designed anlytical network is provided by the comparison of the jets structure data: temperature evolution (figure 4.24), O_2 concentration evolution (figure 4.25) and NO_x concentration evolution (figure 4.26). The reported data is obtained using 10 reactors in each jet, the predictions used 5 reactors in each jet.

MAJOR SPECIES EXHAUST COMPOSITION $[\%\, vol,\, wet]$		
	Measurements [42]	**Predictions base case**
O_2	1.6	1.2
H_2O	29.6	30.0
CO_2	14.4	14.4
N_2	54.4	54.4

Table 4.8: Exhaust volumetric composition of the IFRF furnace

FUEL COMPOSITION EXPERIMENTS $(\%\, vol)$	
CH_4	87.82
C_2H_6	4.59
C_3H_8	1.59
C_4H_{10}	0.52
C_5H_{12}	0.13
$O_2 + Ar$	0.02
CO_2	1.65
N_2	3.68

Table 4.9: Fuel composition IFRF furnace experiments [42]

The temperature structure of the SJ agrees very well with Mancini's network prediction. They are also both in good agreement with the experimental sampling. For the WJ, the temperature evolution is underpredicted all along the jet's length compared to both experimental measurements and Mancini's network, that agree very well with each other:

- theoretically fuel is not consumed before the mixer reactor, but a very small amount of fuel consumed before entering the mixer ($0.215\, g/s$) is reported in [62]. It is also the case in the designed network but to a smaller extent: only $0.146\, g/s$. Additionally, the WJ entrainment is not shielded, entraining more flue gases than in Mancini's network. The amount of inert species of high calorific capacity in the WJ is consequently increased. Coupling these three factors can explain partly the temperature underestimation ;
- Mancini's network considers radiation individually for each reactor as an energy source/sink calibrated using CFD results. This difference between both networks can also explain the temperature evolution difference in the jets. The heat loss and heat exchange model of the designed reactor is quite crude compared to Mancini's work.

Finally, the mixer temperature overestimation could be explained by a conjunction of two factors: first a potential radiation heat loss from this reactor not accounted for in the designed analytical network, coupled to an equal or smaller amount of gases entrained. Indeed, an increase in the amount of entrainment in the mixer can affect the heat balance in two ways: a mass dilution effect and an increase in the calorific capacity of the gas due to boosted concentrations of inert gases. These two phenomena lower the temperature level, however the latter tends to be compensated by the induced temperature decrease through the temperature dependence of the calorific capacity coefficient. The importance of the mixer entrainment is highlighted in appendix E.

The O_2 concentration evolution reflects bigger discrepancies than the temperature, especially concerning the evolution of oxygen along the SJ (oxidizer): in the designed network, the concentration

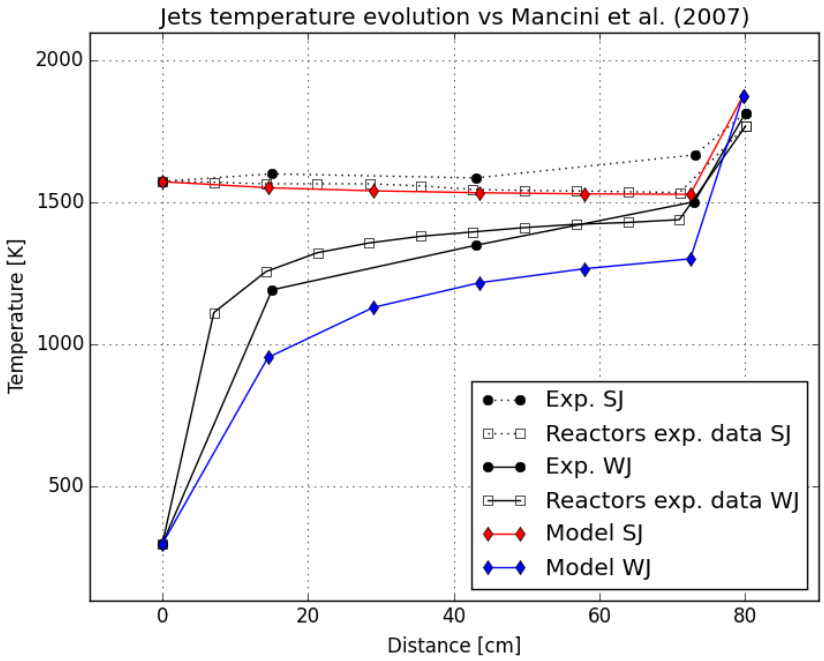

Figure 4.24: Jets temperature evolution comparison (adapted from [62])

shows a more intense decrease than measured experimentally and predicted by Mancini's network. After complete preconditioning, the predicted oxygen concentration is $11.3\ \%\ vol,\ dry$, while it is close to $18\ \%\ vol,\ dry$ for Mancini's network and just under $20\ \%\ vol,\ dry$ experimentally. This significant difference cannot be explained by an early combustion in the SJ because no fuel is present. However, one possible reason could be the lower O_2 concentration at the exhaust for the designed network. This concentration is "recirculated" into the jets via the entrainment and could result in this increasing difference given the mass flows involved for the SJ. For the WJ, the O_2 concentration evolution prediction is very much in accordance with both measurements and reported network results.

Finally as could have been expected, the NO_x concentration evolution in both jets is overpredicted by the designed network, explained by a higher amount of recirculated NO_x.

Overall, it is possible to conclude that the jets structures are predicted consistently by the reactor network developed in this chapter, further validating the use of the analytical submodels even though their current state of development leaves room for improvements. The modeling of the mixer reactor characteristics seems to be central to an accurate estimation of the amount of pollutants emitted at the furnace exhaust.

Additional checks

In order to comprehensively validate this operating point simulation, two more variables must be checked:

- the pressure drop across the system is kept to insignificant levels: $1.5 \times 10^{-6}\ atm$ on the SJ side, $6.5 \times 10^{-7}\ atm$ on the WJ side ;
- because of the method used for pressure closure, the volume of the furnace reactor is inherently a degree of freedom of the model. The initial value is the "true" value and to limit its evolution, the furnace reactor is initialized with a mixture close to what is expected at the end of the simulation. In this case the final value is $0.2\ \%$ bigger after convergence. It corresponds to a negligible $24\ L$ increase (the total volume is $26000\ L$).

This concludes the validation of the IFRF operating point: the analytical reactor network designed yields consistent predictions of good quality in terms of emissions and jet structure. A parametric study is now performed to assess the respective impacts of the mixer length fraction and the number of PSRs in the jets discretization on the predicted emissions.

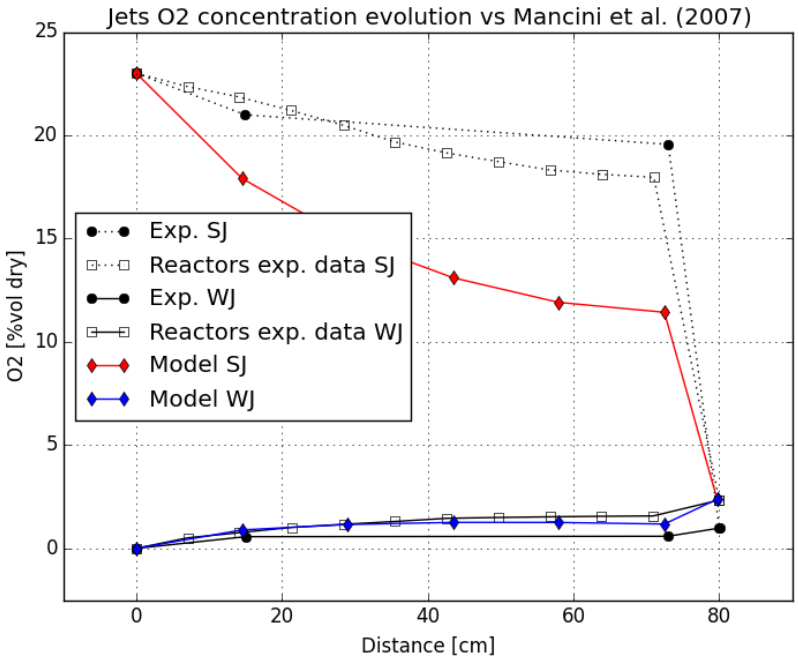

Figure 4.25: Jets O_2 concentration evolution (adapted from [62])

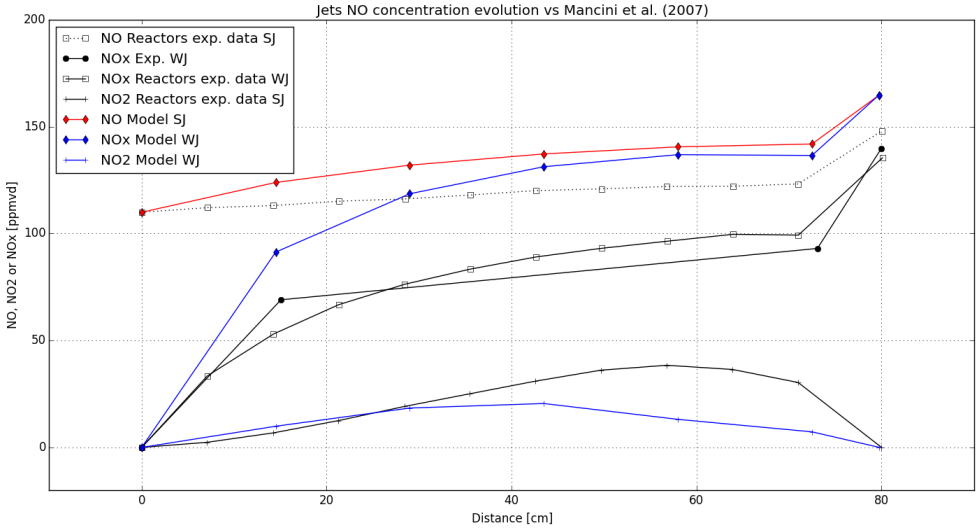

Figure 4.26: Jets NO_x concentration evolution (adapted from [62])

4.6.4. Parametric study

The predictions obtained from all simulations are gathered in table 4.10.

Case n°	n_{PSR}	$x\%$ [%]	NO [$ppmvd$]	CO [$ppmvd$]
1 (base case)	5	10.0	169	27
2	5	20.0	169	24
3	5	15.0	169	25
4	2	15.0	169	25
5	1	20.0	168	24
6	4	10.0	169	27
7	4	20.0	169	24

Table 4.10: Parametric study emission predictions

Influence of $x\%$

The mixer reactor volume has no impact on the NO prediction from the network in the investigated window. A faint decrease in CO emission is caused by an increase of $x\%$. The parameters with the most potential to influence the emissions are gathered in table 4.11 for cases 4 to 7: the peak temperature, the residence time in this high temperature region and the composition of the igniting mixture in this reactor.

Case n°	T_{peak} [K]	τ_{res}^{mixer} [ms]	$CH_4^{mixture}$ [$\%\, vol$]	$inerts^{mixture}$ [$\%\, vol$]	$O_2^{mixture}$ [$\%\, vol$]
4	1880	3.546	2.2	91.0	6.4
5	1879	4.773	2.1	91.2	6.2
6	1876	2.346	2.3	90.8	6.5
7	1879	4.773	2.2	91.2	6.3

Table 4.11: Mixer reactor characteristics

Among them, the only parameter significantly evolving with $x\%$ is the residence time in the mixer, a high temperature reactor with very low oxygen concentration. CO production is favored when oxygen is not available in sufficient quantity as well as for insufficient residence times in high temperature regions. The CO emission trend follows the mixer residence time trend: when τ_{res}^{mixer} increases, the CO produced tend to decrease. The other parameters are completely independent from the mixer length fraction. Finally it is worth noticing the highly diluted lean environment in the mixer reactor, characteristic of flameless conditions.

Influence of n_{PSR}

The number of PSRs in the jets discretization has no influence on the predicted emissions. However it is of tremendous importance when it comes to simulation time: an exponential increase of the simulation time with n_{PSR} is displayed in figure 4.27.

In theory it seems like a 4-reactor model would be enough to obtain fast and reliable emission predictions. But because of a weakness in the current design of the Shielded Entrainment Model, the values of both n_{PSR} and $x\%$ have to be determined in a coordinated manner.

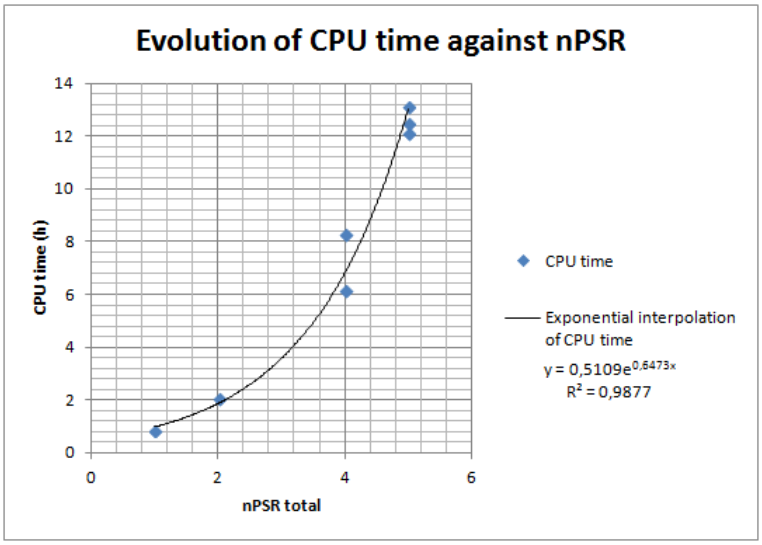

Figure 4.27: Influence of n_{PSR} on CPU time

4.6.5. Conclusion

This reactor network has been designed based on arguments largely inspired by the modeling work on the IFRF furnace reported in [62] by Mancini et al. It was only fitting to test it first against experimental data obtained with this furnace and against predictions by Mancini's own reactor network. The development of two analytical submodels, the Bending Model and the Shielded Entrainment Model, allowed to get rid of the experimental/CFD dependence of the reference network of Mancini and the resulting analytical–only reactor network performs very well as far as the emissions and jets structure are concerned.

Furthermore, the influence of two important parameters of the network have been investigated:

- the mixer length fraction $x\%$ has no impact on the NO emissions, but slightly influences the final CO production ;
- the number of PSRs in the jets discretization n_{PSR} has no influence on either emission, but greatly impacts the simulation time.

Results show that the most critical reactor in the network to model is the mixer reactor: it is where the peak temperature in the network is located (main influence of NO production), its extent seems to influence the CO production but it also determines the amount of entrained gases, and hence the reactor temperature. Details of the reactor network structure designed by Mancini could be obtained only after this modeling work and are reported in appendix E. Although a different reactor volume determination process and a different criterion defining the extent of the mixer reactor were used, they confirm the independence of the NO_x predictions regarding the mixer volume or the number of reactors discretizing the jets. Additional simulations were performed with the designed network, using Mancini's criterion to define the mixer extent. They highlighted the importance of a better modeling of the mixing region entrainment.

Finally, one of the motivations for the design of this reactor network was to make it more general and applicable to other flameless furnace setups than the IFRF installation. This potential adaptability will now be tested, simulating two other furnaces: first the University of Mons flameless furnace, and eventually the original target system will be simulated: the multiple burner flameless furnace of TU Delft.

4.7. Prediction of emissions from the Mons furnace

One of the components of the network (the Bending Model) has already been tested against results obtained on the Mons flameless furnace by Lupant [20]. But in addition to trajectory data, her final dissertation also gathers experimentally determined NO and CO emissions. The fuel used in this furnace is natural gas as well: the GRI 3.0 chemical mechanism is used.

4.7.1. Inputs

Different inputs of the reactor network model are now modified to describe geometrically the Mons furnace. The inlet thermodynamic conditions are different as well. This is all reported in table 4.12. This furnace is significantly smaller than the IFRF furnace and could be classified as a laboratory scale furnace, for both its size and burner power (30kW). Comparatively, the IFRF furnace could be classified as a semi-industrial furnace (580kW).

USER–DEFINED			
Geometrical		**Thermodynamic**	
$L\ [m]$	1.0	$T_0^{WJ}\ [K]$	298
$l\ [m]$	0.35	$p_{reservoir}\ [atm]$	1.0
$h\ [m]$	0.35	$p_{furnace}\ [atm]$	1.0
$\emptyset_{SJ}\ [m]$	0.0248		
$\emptyset_{WJ}\ [m]$	0.0028		
$S\ [m]$	0.155		
$\theta_0^{SJ}\ [°]$	0		
$\theta_0^{WJ}\ [°]$	-13 / 13		

Table 4.12: User–defined parameters Mons furnace

During the validation of the Bending Model, one specificity of this burner was mentioned: the two weak fuel jets are not injected at the same converging angle in reality. However the designed network is based on a perfectly symmetrical furnace: an injection angle of $13°$ converging is adopted for both weak jets so that they converge and mix with the SJ at the same axial location.

For this configuration the combination ($n_{PSR} = 5$; $x\% = 20.0\%$) is used: it gives a smooth evolution of the jet entrainment and keeps the reactor number at a relatively low value.

The oxidizer is pure air taken as:

OXIDIZER COMPOSITION $(\%\ vol)$	
O_2	21.0
N_2	79.0

Table 4.13: Oxidizer composition for the Mons furnace reactor network simulation

The fuel (natural gas) stream average composition is specified in [20]. However it contains species not covered by the detailed GRI 3.0 mechanism (butane and pentane). Their combined reported concentration (0.56%) is divided equally over the other hydrocarbons to give the fuel composition that will be used in the model (table 4.14.

This inevitably changes the fuel heating value, and in order to keep the burner power consistent between experience and simulations the inlet mass flows will consequently be different. The calculated

FUEL COMPOSITION ($\%\ vol$)	
CH_4	90.4
C_2H_6	5.19
C_3H_8	1.25
CO_2	0.93
N_2	2.23

Table 4.14: Fuel composition for the Mons furnace reactor network simulation

LHV for the simulation fuel is:

$$LHV_{fuel,CRN} = 34950\,kJ/m^3\ @15°C$$

Based on this new value, the burner power and the excess air, the inlet mass flows are recalculated:

1. The burner power is $P_{fuel} = 30\,kW$.
2. Using $LHV_{fuel,CRN}$ the volumetric flow of fuel injected (@15°C) is obtained, then the total mass flow of fuel using the corresponding density. The WJ inlet mass flow is then obtained by dividing this value by the number of weak jets (2):

$$\phi_m^{WJ} = 3.205 \times 10^{-4}\,kg/s$$

3. The corresponding volumetric flow of fuel injected in normal conditions $(0°C\ ;\ 1atm)$ is then obtained ($\phi_{v,N}^{WJ}$). The injected volumetric flow of oxidizer in normal conditions is then calculated:

$$\phi_{v,N}^{SJ} = 4.76(1+E)\phi_{v,N}^{WJ} n_{O_2,st}$$

with E the excess air and $n_{O_2,st}$ the stoechiometric amount of oxygen:

$$n_{O_2,st} = x + \frac{y}{4} - \frac{z}{2}$$

when the empirical fuel formula is $C_xH_yO_zN_w$. With the modified fuel $x = 1.0546$, $y = 4.0274$, $z = 0.0186$ and $w = 0.0446$ giving:

$$n_{O_2,st} = 2.05215$$

4. Finally using the oxidizer density at normal conditions the mass flow of oxidizer injected is obtained for the given excess air. In this set of simulations, two excess air settings are simulated:

$$\phi_m^{SJ,10\%} = 1.126 \times 10^{-2}\,kg/s\ @\ 10\%\ \text{excess air}$$

$$\phi_m^{SJ,20\%} = 1.228 \times 10^{-2}\,kg/s\ @\ 20\%\ \text{excess air}$$

Finally the last two parameters remaining to determine are the SJ inlet temperature and the exit temperature. Two main operating points are defined:

- Point 1: $T_0^{SJ} = 800.0°C$, $E = 10\%$, $T_{exit} = 1100°C$
- Point 2: $T_0^{SJ} = 800.0°C$, $E = 20\%$, $T_{exit} = 1100°C$

These two parameters are also the subject of a parametric analysis in [20] that will be reproduced: for each excess air, T_0^{SJ} is varied in the range $(800.0°C\ ;\ 1000.0°C)$ and T_{exit} is varied in the range $(1100.0°C\ ;\ 1300.0°C)$.

4.7.2. Simulation cases

In total 12 operating points of the Mons furnace are simulated. They are gathered in table 4.15.

SIMULATIONS			
Case n°	$T_0^{SJ}\,[K]$	$E\,[\%]$	$T_{exit}\,[K]$
Operating point 1	1073	10.0	1373
Operating point 2	1073	20.0	1373
3	1073	10.0	1473
4	1073	10.0	1573
5	1273	10.0	1373
6	1273	10.0	1473
7	1273	10.0	1573
8	1073	20.0	1473
9	1073	20.0	1573
10	1273	20.0	1373
11	1273	20.0	1473
12	1273	20.0	1573

Table 4.15: Simulation cases Mons furnace

4.7.3. Results

The link between Lupant's notations and the ones used in this work is:

$$T_f = T_{exit}\,;\, T_a = T_0^{SJ}$$

The measured NO emissions at the exhaust are systematically corrected to a reference $3\%\ O_2$ content using :

$$NO_{@3\%O_2} = NO_{measured}\frac{n_{f,measured}}{n_{f,@3\%O_2}} \tag{4.11}$$

with n_f the number of moles of exhaust gas per mole of fuel. The same correction is applied to the predictions from the reactor network. The emissions are not corrected to dry basis. n_f is calculated using:

$$\begin{aligned} C_xH_yO_zN_w + \left(x+\frac{y}{4}-\frac{z}{2}\right)(1+E)\,(O_2+3.76N_2) \rightarrow xCO_2 + \frac{y}{2}H_2O + E\left(x+\frac{y}{4}-\frac{z}{2}\right)O_2 \\ + \left[3.76\left(x+\frac{y}{4}-\frac{z}{2}\right)(1+E)+\frac{w}{2}\right]N_2 \end{aligned} \tag{4.12}$$

When the excess air is known, it gives:

$$n_f = x+\frac{y}{2}+E\left(x+\frac{y}{4}-\frac{z}{2}\right)+\left[3.76\left(x+\frac{y}{4}-\frac{z}{2}\right)(1+E)+\frac{w}{2}\right] \tag{4.13}$$

When the excess air is unknown but the O_2 content at the exhaust $x_{O_2,exhaust}$ is known, it is necessary to compute the corresponding excess air before using equation 4.13:

$$E = x_{O_2,exhaust}\frac{x+\frac{y}{2}+3.76\left(x+\frac{y}{4}-\frac{z}{2}\right)+\frac{w}{2}}{\left(x+\frac{y}{4}-\frac{z}{2}\right)\left(1-4.76x_{O_2,exhaust}\right)} \tag{4.14}$$

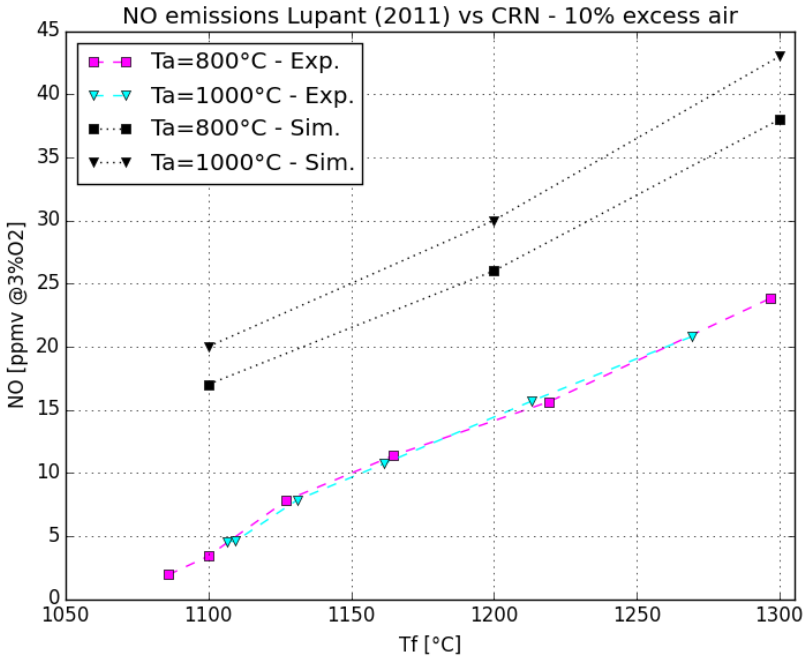

Figure 4.28: NO_x emissions from the Mons furnace at 10% excess air (adapted from [20])

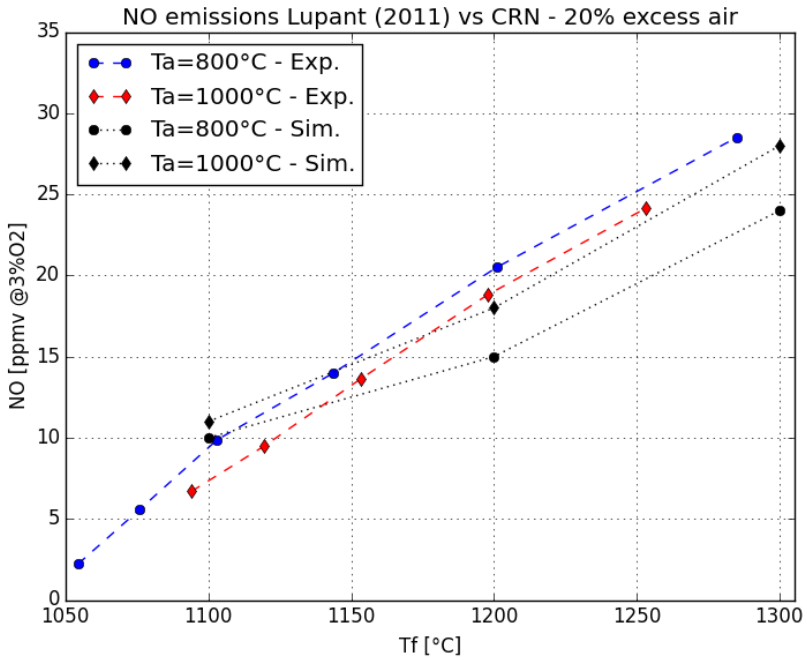

Figure 4.29: NO_x emissions from the Mons furnace at 20% excess air (adapted from [20])

The predicted NO emissions are compared to the corrected measured values in figures 4.28 and 4.29 respectively for 10% and 20% excess air. The predicted NO_x emissions are higher than the reported NO_x emissions for 10% excess air while for 20% excess air, predictions and measurements match well given the measurement error of a few ppm. The measurement error alone cannot account for the difference in the 10% excess air case, which is probably caused by a relatively inaccurate representation of the mixing region. However the overall level of emission is predicted in the right order of magnitude, typical of flameless conditions. In both cases, the increasing trend of NO emission with an increasing exhaust temperature is captured. Finally, the influence of preheating the air from $800°C$ to $1000°C$ on the predictions is of the order of $3-5ppmv$ in both cases. Experimentally, and accounting for the measurement error, the same could be said.

Concerning the furnace CO emissions, experimental data is available only for the two base operating points. The measurement uncertainty for the CO concentration is much bigger than for NO: the results have to be analyzed accounting for $\pm 20\,ppm$. Table 4.16 gathers all CO emission data and predictions: they agree well with each other given the uncertainty.

$E = 10\%$	**Exp. 1**	**Exp. 2**	**Exp. 3**	**Prediction**
CO $[ppmvd]$	35	15	21	48
$E = 20\%$	**Exp. 1**	**Exp. 2**	**Exp. 3**	**Prediction**
CO $[ppmvd]$	31	19	25	32

Table 4.16: CO emissions from the Mons furnace

Finally the average CPU time for each simulation is $4.3h$: though this is not instant prediction, it still constitutes a huge gain in simulation time compared to a CFD study, especially given the good quality of the predictions obtained. Cases 9 and 11 presented a singularity in simulation time : they lasted respectively $14.5h$ and $17h$.

4.7.4. Conclusion

The adaptability of the developed reactor network is clearly demonstrated: for a completely different furnace (dimensions, power output, burner), the predicted emissions are also of good quality for both investigated pollutants: either within the experimental measurement error or predicting the correct order of magnitude. Further development of this analytical reactor network to correct the weaknesses highlighted in the previous section could have a beneficial effect on the accuracy of the estimations.

There is however one common feature to both furnaces simulated so far: the general flow configuration. The (single) burner is located on one side of the chamber, the exhaust on the other side. This makes for a ”simple” flow field, more suitable for CRN modeling. The last validation case will test the model on a much more complex furnace which is one of the original target systems of this work: the multiple burner flameless furnace present at the Process & Energy department of TU Delft.

4.8. Prediction of emissions from the TU Delft furnace

4.8.1. Furnace characteristics

The flameless furnace of the Process & Energy department of TU Delft is yet again a very different furnace compared to both setups simulated before on several accounts (figure 4.30 shows a sketch of the furnace):

- Furnace dimensions: this furnace has a more cubic shaped volume $(1.5m \times 1.5m \times 1.85m)$ than a rectangle parallelepiped shape like the previous furnaces.

- Furnace configuration: the burners used induce a different configuration. First of all, regenerative burners are used, and second it is a multiple burner setup: 3 burner pairs are installed. Because of the regenerative feature the burners work in pair: while one is firing, the paired burner functions as exhaust sucking out the hot flue gas, storing the recuperated heat in order to preheat the

oxidizer stream when the firing/regenerating cycle switches. In total 6 burners are installed, each pair having a thermal power of 100kW.

- The burner/exhaust arrangement is not as simple as in the previous furnaces. This time the exhaust is twofold: the major part of the flue gas is leaving via the paired burner (80%) while the remaining (20%) exits via a stack located on the roof of the furnace.

- The burner configuration itself is different: instead of being constituted of one central strong oxidizer jet surrounded by two symmetrically located weak fuel jets (the usual SJ/WJ configuration), the regenerative burners are constituted of a central weak fuel jet surrounded by four symmetrically located strong oxidizer jets which induces more of a WJ/SJ configuration (see figure 2.7). This particularity will test even further the versatility and adaptability of the Bending Model.

More details on the burners locations, firing mode (parallel or staggered) or cycle time can be found in [5] but are not reported here since the purpose of the developed reactor network is not the same as the author's goals. The only aim is to predict as accurately as possible the emissions and not study the burner-burner and burner-stack interactions, or the influence of the cycle time on the emissions. In fact, the reported experimental data obtained by Danon varying the above mentioned parameters forms clusters around an average value for both NO_x and CO. In addition the designed model is not able to account for these parameters and important approximations are necessary to simulate this furnace using the model. Consequently the only reasonable and achievable goal is to obtain a good order of magnitude for the predicted emissions, consistent with the clusters of experimental data. Only one of the parameters investigated by Danon can be accounted for with the model: the excess air ratio.

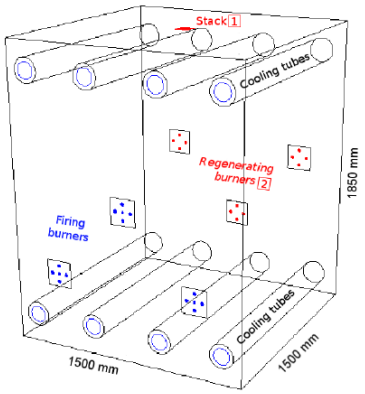

Figure 4.30: Sketch of the TU Delft multiple burner flameless furnace (from [5])

4.8.2. Necessary approximations

A complex flow pattern results from the particular configuration of this furnace. In order to be compatible with the simple configuration modeled in the reactor network the complex geometry has to be greatly simplified. Unfortunately none of the true symmetries of the system can be exploited since they don't result in the desired simple burner configuration (1 surrounding jet with the corresponding portion of the central jet). Sharp approximations are then made using characteristics of the furnace that are not true symmetries because of the wall presence and the different possible locations of the burners:

1. Only one of the three burner pairs is accounting for with the corresponding 1/3rd of the total volume.

2. On this new sub–system, only 1/4th of the volume is considered to be representative. This second approximation allows the final system to be reduced to 1 surrounding jet and a quarter of the central jet, a simple configuration almost identical to the desired one. A small modification in the model (central jet volume and entrainment determination) allows to consider only 1/4th of the central jet instead of half.

In conclusion, this whole very complex setup is modeled considering only 1/12th of its total volume to be typical, along with the corresponding jets. The use of these pseudo–symmetries constitutes sharp approximations, and the obtained predictions have to be analyzed accordingly.

4.8.3. Inputs

Only one operating point is simulated, corresponding to an excess air ratio of $\lambda = 1.23$. The values $n_{PSR} = 3$ and mixer length parameter $x\% = 20.0\%$ are used (the mixer length parameter definition can be found in section 4.5.1). For this furnace a value of $x\% = 10.0\%$ appeared to underestimate too much the mixing/reacting region resulting in a residence time shorter then the ignition time: no ignition occurs in the mixing region as it should. A value of $x\% = 30.0\%$ yielded the same predictions as with $x\% = 20.0\%$.

Because of the regenerating effect, the preheat temperature of the oxidizer jet is in reality variable. The amplitude of its variations depends mostly on the cycle time of the burner pair, but the burners configuration, the firing mode and the excess air ratio also impact the average value. Experimentally determined values are reported in [5] and an average preheat temperature of $800°C$ was chosen to be representative. Experimental exhaust temperatures are also reported for all configurations: a value of $1100°C$ was chosen to be typical. This value is a slight overestimation of the experimental data $(1035°C–1075°C)$, but underestimates predictions from a detailed CFD study performed by Danon $(1120°C–1140°C)$.

Similarly to the Mons furnace, the real fuel composition (Dutch Natural Gas) had to be approximated to be compliant with the GRI 3.0 chemical mechanism. A composition as close as possible from the actual fuel is chosen, but once again the modifications impact the heating value. Consequently, as for the previous furnace the mass flows are calculated according to the burner pair power $(100\ kW_{th})$, the calorific value of the fuel used in the simulation and the excess air ratio. The calculated heating value for the simulation fuel is:

$$LHV_{fuel,CRN} = 29966\ kJ/m^3\ @15°C$$

The different inputs used for the model are gathered in tables 4.17, 4.18 and 4.19.

USER–DEFINED			
Geometrical		**Thermodynamic**	
$L\ [m]$	1.5	$\phi_m^{SJ}\ (oxidizer)\ [kg/s]$	1.051×10^{-2}
$l\ [m]$	0.25	$\phi_m^{WJ}\ (fuel)\ [kg/s]$	2.63×10^{-3}
$h\ [m]$	0.925	$T_0^{SJ}\ [K]$	1073
$\emptyset_{SJ}\ [m]$	0.020	$T_0^{WJ}\ [K]$	298
$\emptyset_{WJ}\ [m]$	0.012	$T_{exit}\ [K]$	1323
$S\ [m]$	0.050	$p_{reservoir}\ [atm]$	1.0
$\theta_0^{SJ}\ [°]$	0	$p_{furnace}\ [atm]$	1.0
$\theta_0^{WJ}\ [°]$	0		

Table 4.17: User–defined parameters TU Delft furnace

Important note: the network was developed for a central SJ and a surrounding WJ. In this case the surrounding jet is the oxidizer and is in reality the SJ. In the model the (central) SJ inputs will take the values of the fuel WJ indicated in table 4.17 and the surrounding WJ inputs will take the indicated values of the strong oxidizer jet.

OXIDIZER COMPOSITION $(\% \, vol)$	
O_2	21.0
N_2	79.0

Table 4.18: Oxidizer composition for the TU Delft furnace reactor network simulation

FUEL COMPOSITION $(\% \, vol)$	
CH_4	81.2
C_2H_6	2.9
C_3H_8	0.7
CO_2	0.9
N_2	14.3

Table 4.19: Fuel composition for the TU Delft furnace reactor network simulation

4.8.4. Simulation cases

As mentioned three cases were investigated on the same operating point, varying the mixer length fraction parameter:

SIMULATIONS		
Case n°	n_{PSR}	$x\%$ [%]
1	3	10.0
2	3	20.0
3	3	30.0

Table 4.20: Simulation cases TU Delft furnace

4.8.5. Results

The measured emissions were normalized towards a reference $3\% \, O_2$ content in the flue gas using the following formula:

$$x_i = x_i^m \lambda \frac{x_{O_2,air} - 0.03}{x_{O_2,air}} \tag{4.15}$$

with $x_{O_2,air}$ the oxygen fraction in pure air, λ the excess air ratio, x_i^m the measured mole fraction of species i in the flue gas in $[ppmv, dry]$ and x_i the normalized mole fraction of species i in $[ppmv@3\%O_2, dry]$. The predictions are obtained after approximately $2h$ CPU time. The results are gathered in table 4.21 and cases 2 and 3 are plotted against experimental data in figures 4.31 and 4.32.

For the simulated operating point, CO emissions are in overall agreement with the whole experimental dataset provided a minimum mixer volume. Furthermore the predictions $(33-39 ppmv@3\%O_2, dry)$ are located in the upper range of the experimental concentration span $(6-40 ppmv@3\%O_2, dry)$, consistently with the previous simulations on different setups were the CO concentration was slightly overestimated. The instrumental error for CO concentration determination is reported to be $\pm 7 \, ppm$.

Contrary to the same previous simulations, the predicted NO emissions are not conservative : an underprediction of NO concentration at the exhaust is clear, even accounting for the reported $\pm 7 \, ppm$ experimental uncertainty. However the order of magnitude $(\sim 10 ppm)$ is correctly predicted. The major simplifications made in order to make the real furnace geometry compliant with the reactor network may

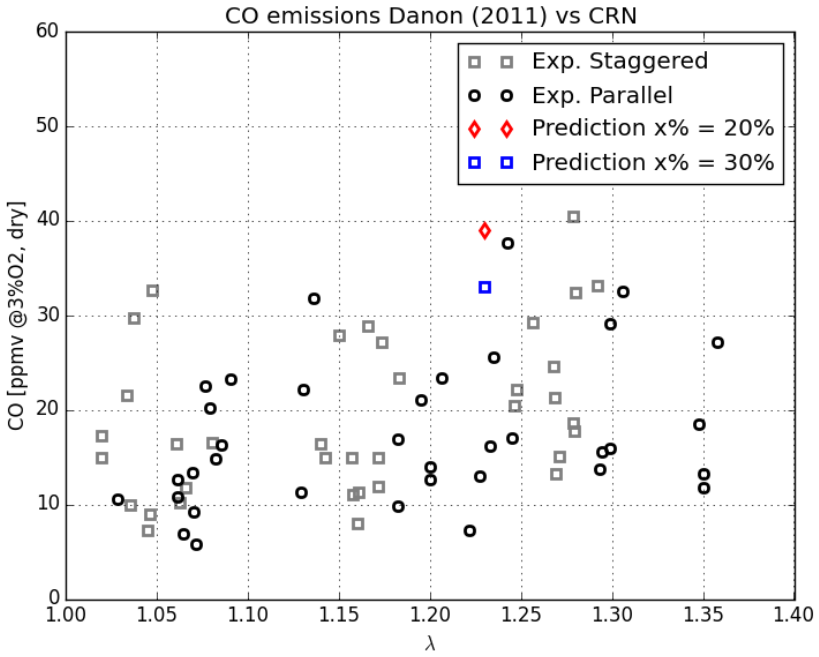

Figure 4.31: Prediction of CO emission from the TU Delft flameless furnace (adapted from [5])

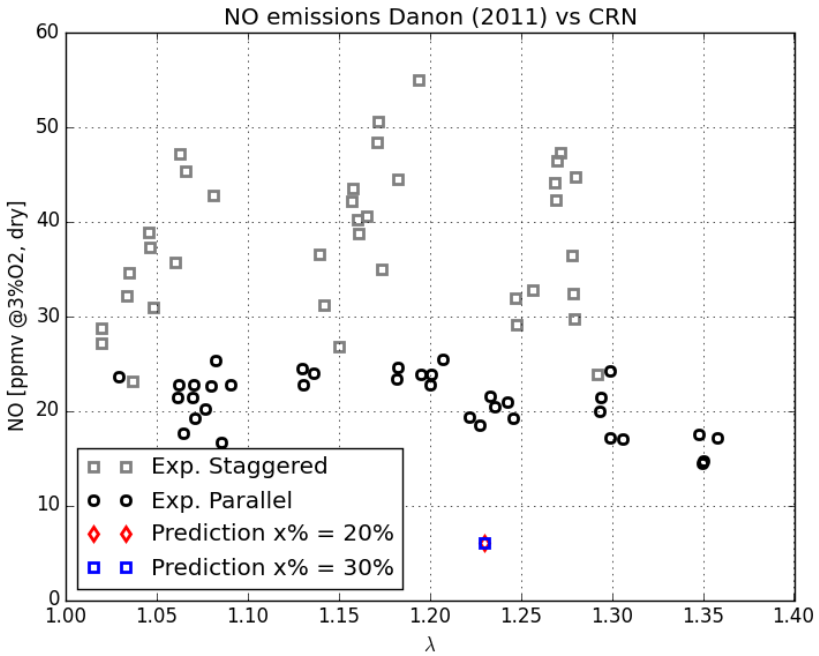

Figure 4.32: Prediction of NO emission from the TU Delft flameless furnace (adapted from [5])

PREDICTIONS				
Case n°	n_{PSR}	$x\%$ [%]	NO $[ppmv@3\%O_2, dry]$	CO $[ppmv@3\%O_2, dry]$
1	3	10.0	1	70
2	3	20.0	6	39
3	3	30.0	6	33

Table 4.21: Simulations results on the TU Delft furnace

have a role in this prediction, along with the mixing region modeling deficiencies and the assumptions made on the preheated oxidizer temperature and the furnace exhaust temperature. But the major factor is probably the lack of shielding on the surrounding jet, which is in this case the SJ with the most important mass flow contribution. An overestimation of this jet entrainment impacts the total mass flow through the mixer to a greater extent than if the surrounding jet is the WJ. Hence the temperature level of the mixing region is underestimated, and so is the NO production.

Finally the importance of the mixer reactor is highlighted again: its volume has a definite impact on both NO and CO emissions in this case. The residence time in this reactor needs to be higher than the ignition time, but if ignition occurs, the volume does not seem to influence the NO formation and once again CO creation tends to decrease when this volume increases. This phenomenon is linked to a longer residence time in a high temperature region, favoring CO oxidation.

To conclude, the reactor network predictions for the TU Delft flameless furnace can be considered of good quality overall, keeping in mind the experimental error, the sharp assumptions necessary and the identified model weaknesses. The overall quality of the predictions is however an indication of the good behavior of both analytical sub–models: they appear to capture the major phenomena involved, although they could be refined to do so with more accuracy and coherence.

4.9. General conclusion

A simple chemical reactor network aiming at providing reliable emissions predictions (NO_x and CO) in a reasonable amount of time was successfully built. It is based on an idea reported in [62] and adapted to circumvent the use of any input from previous CFD studies or experiments on the investigated system.

This goal was reached by developing two components on which the whole network is based. First a model able to describe jets trajectories and their convergence in a SJ/WJ configuration was implemented and validated. It resulted in an adaptation of the so-called ”Bending Model” derived by Faghani and Rogak [71]. This model is particularly interesting because of its adaptability: it was derived for a pair of jets, but can easily be tuned when more jets are involved, and its validity is not limited to a SJ/WJ configuration. It also takes as input several geometrical parameters (ports diameters and spacing, injection angles) which can be modified to describe a wide range of burners. There are however a few shortcomings: it is a 2D model which means that the jets involved have to be coplanar, and all jets are supposed to be injected through circular ports. To overcome the first deficiency, simplifications can be made regarding the burner geometry to reduce it to a simple configuration. This component allows analytical access of a key parameter of flameless combustion: the length from the injection plane at which the jets merge, after having separately entrained flue gas in sufficient quantity.

In order to predict as accurately as possible the amount of flue gas entrained by each jet — another key physical phenomenon of flameless combustion — a second component is developed. Based on entrainment data reported by Mancini et al. [62], a mutual shielding of the jets on each other’s entrainment pattern was detected. Geometrical data calculated by the Bending Model is then used to build a shielding factor. It is in turn applied to an analytical jet entrainment law (Ricou & Spalding [53]) to obtain a systematic way of determining each jet entrainment in a SJ/WJ configuration. This Shielded Entrainment Model is however not perfect and several deficiencies were noted during the study: it does not provide with a good approximation of the surrounding jet shielding so no shielding is applied on this jet, and the determination of the mixer reactor entrainment needs to be improved. This is to be related with the definition of the mixer streamwise extent and volume.

These two submodels provide a systematic analytical way of modeling two important coupled physical phenomena in flameless furnaces: pre–conditioning and jet merging. Based on them, a CRN composed of Perfectly Stirred Reactors (PSRs) is built and tested against three different furnaces for which experimental data is available: the semi–industrial furnace of the IFRF studied by Mancini et al. [62], the laboratory–scale furnace present at the University of Mons studied at length by Lupant [20] and the multiple burner flameless furnace of the Process & Energy department of TU Delft [5]. These three setups are very different in terms of size, burner power, burner configuration or burner number, allowing to test the adaptability of the designed network. The predictions obtained for both investigated pollutants (NO_x and CO) are overall of good quality for each furnace: at least the correct order of magnitude is predicted, parametric studies give the right trends, and the simulation times are very reasonable. One salient feature of the network is the importance of the mixer reactor characteristics, key to the network predictions. Finally, areas for improvements have been identified:

- Improving the definition of the mixer reactor extent (length and volume).
- A better way of calculating the entrainment shielding would be beneficial to model the surrounding jet shielding. Additionally the determination of the mixer reactor entrainment using this model can be improved.
- Incorporating a more advanced heat loss model, in particular for the mixer reactor, would probably help to predict the emissions more accurately.

5

Emission modeling of a jet engine lean–premixed combustor

5.1. Introduction

Since its creation, commercial aviation has made great progress to now establish itself as an essential part of modern society not only allowing worldwide economic exchanges but also encouraging cultural exchanges. The number of passengers carried by airlines keeps soaring while continuous improvements have allowed for increased safety and passenger comfort, but also fuel savings and emission reductions [6]. Despite these positive developments, specific challenges have to be overcome in order tho sustain the future growth of aviation: availability of fuel resources and environmental concern.

With global warming and ozone depletion now being major issues to be reckoned with, aviation emissions cannot be ignored. The gradual technological improvements are counterbalanced by an always intensifying air traffic. The emission standards are becoming more and more stringent with the consequent need to reduce pollutants levels drastically [74]. Therefore, in order to initiate and define a framework for future technologies, the Advisory Committee for Research in Aeronautics (ACARE) has targeted emission reduction objectives on various fronts: noise levels, air pollution, fuel consumption (figure 5.1). Compared to the baseline year 2000, it aims at drastically reducing noise levels (50% reduction), CO_2 emissions (75% reduction) and NO_x emissions (90% reduction) by 2050. These ambitious objectives can only be achieved by breakthrough innovations in both aircraft concept and aero engines.

In parallel, kerosene has been used in aviation for a long period of time due to its numerous qualities making it ideal for aircraft operations: relatively high energy density, ease of storage, acceptable cost and safe usage. But oil is a limited natural reserve and air traffic is only predicted to increase while the oil prices are unstable but overall on the rise. The inevitable fuel shortage combined to environmental concerns triggered the research for alternative fuels. Reducing the carbon footprint will require to switch to hydrogen or hydrogen–rich fuels, among which LNG and LH2 are attractive [74]. However the use of such cryogenic fuels raises problems related to the specificity of their storage. A conventional aircraft architecture cannot accommodate the cylindrical or spherical tanks in the usual volume dedicated to fuel storage (wings). On the contrary, a Blended–Wing–Body (BWB) configuration seems to be more promising towards the objective of using alternative fuels [75]. Nonetheless a radical change in aircraft concept alone cannot meet the future standards, and drastic improvements of the propulsion system are also required in order to take full advantage of using cryogenic fuels for instance. Gas turbine engines have improved significantly over the years, becoming lighter, stronger and more efficient. Proven methods to increase engine efficiency include increases in bypass ratio, overall pressure ratio and turbine inlet temperature, but they all possess increasingly significant adverse effects and these trends cannot be sustained [74]. New engine architectures have to be envisioned.

In a BWB configuration, an integration of body and wing is used instead of the conventional separate fuselage with wings. This allows to obtain a larger amount of space available within the aircraft, making it possible to carry the tanks used for cryofuel storage. Additionally, the thiner parts of the wings can still be used to carry more conventional fuels like kerosene. A multi–fuel BWB concept with a

combination of biofuel and cryofuel is proposed by the AHEAD project (Advanced Hybrid Engines for Aircraft Development) sponsored by the European Union. To power this new aircraft, a new type of propulsion system – called the hybrid engine – has been conceived, which is able to meet the requirements of the multi–fuel BWB aircraft [6]. A schematic of this new engine is displayed in figure 5.2. It includes a combination of several technologies, among which the breakthrough innovation of interest is the hybrid dual combustion chamber. The main combustor operates on LH2/LNG in lean–premixed conditions while the second combustor (between high pressure turbine and low pressure turbine) uses biofuel in the flameless combustion mode. Such a novel combustion system has never been used before for aero engines. This unique design has several advantages. Firstly, since the flammability limits of H_2/Methane are wider than kerosene, the combustion can take place at lean conditions, thus reducing NO_x emissions significantly compared to a conventional kerosene combustor. Secondly, the LH2 used for the first combustor can be used for cooling the bleed air, thus reducing the required amount and reducing the fuel consumption, which result in an increase in the overall efficiency. Moreover, using LH2 in the first combustion chamber will increase the concentration of water vapor and reduce the concentration of O_2 in the hot exhaust stream entering the second combustion chamber, thus creating a hot vitiated environment in which flameless combustion can be sustained. The implementation of the flameless combustion can minimize the emission of CO, NO_x, UHC and soot. Additionally, the reduced emission of soot and UHC also reduces the amount of nucleation centers available for condensation of water vapor in the plume, thus reducing the contrail formation. In conclusion, this new propulsion design has the potential to drastically reduce emissions of CO_2, CO, UHC, NO_x and soot. The objective of this chapter is to model the emissions from the first combustor, burning LH2 in a lean–premixed combustion regime. Contrary to the previous chapter, the objective is not to design a generally applicable network but a network specific to this combustion system, able to predict the main parameters of influence and their effects.

5.2. The cryo–combustor of the AHEAD engine

Low emissions is *the* design criterion behind the whole AHEAD concept and its development. For the first combustor the design responsibility was given to TU Berlin, one of the partners in the AHEAD consortium. Premixed combustion was chosen as the preferred mode since it exhibits much lower flame temperatures than diffusion flames, offering the potential to very low NO_x emissions [76]. However, burning a high reactivity fuel like hydrogen may push forward the lean blowout limit, but it also increases the flashback susceptibility of a premixed system. Additionally, in the designed combustor, the flame is swirl stabilized and to waive the necessity of a bluff body, a cylindrical centerbodyless mixing tube is used to further enhance mixing. The induced swirling flow field exhibits a central recirculation zone and its vortex breakdown is situated under most conditions at the nozzle exit or just upstream. Such a flow field is prone to combustion induced flashback for high reactivity fuels. To overcome this stability issue, additional air is injected on the axis of rotation in the mixing tube. This has the advantage to further enhance mixing. Both spatial and temporal mixing are important factors influencing emissions [76]: the force of premixed combustion is to allow operation at lean equivalence ratio, inducing relatively low flame temperatures. When mixing is not optimal, some regions will be overall richer than the operating equivalence ratio, and some leaner, but due to the non–linearity behavior of NO_x (thermal) formation, it will result in higher emissions.

Using an original experimental setup sized to what the ”real life” combustor would be, Reichel et al. investigated the flashback resistance of the designed swirl stabilized hydrogen burner with axial air injection [76]. A representation of the general burner geometry is shown in figure 5.3 and more detailed schematic of the burner is displayed in figure 5.4. The combustor length is $297\ mm$. The typical flow field of swirl stabilized combustors is displayed: an inner (central) recirculation zone, enveloped by an annular jet and an outer less intense recirculation zone between the annular jet and the walls. They concluded that in the presence of a high amount of axial air injection, no occurrence of flashback was observed for the experimental conditions investigated: inlet temperatures up to $620\ K$ and up to stoechiometric conditions.

In a more recent study, Reichel et al. [77] investigated the axial flame base location as function of axial air injection and fuel momentum for a variety of inlet parameters: equivalence ratio, integral burner exit velocity and burner preheat temperatures. From their results they extracted the axial location of maximum flame front probability density x_F, which they use to quantify the flashback safety margin.

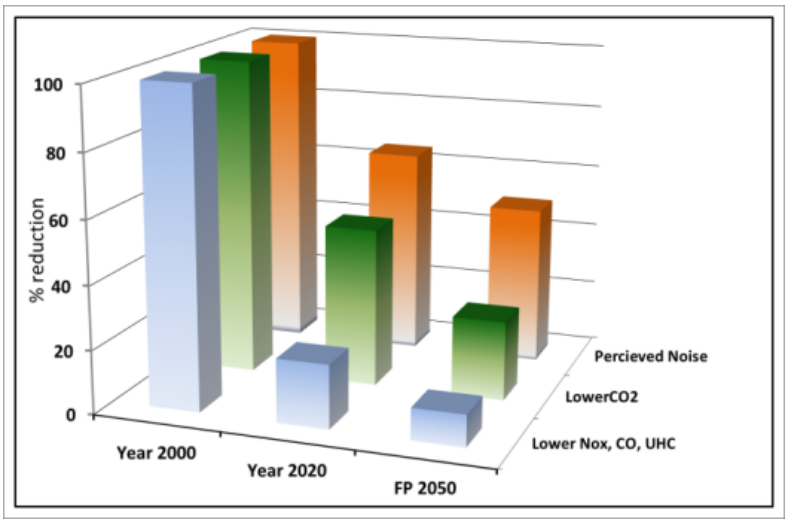

Figure 5.1: ACARE vision for Europe (from [6])

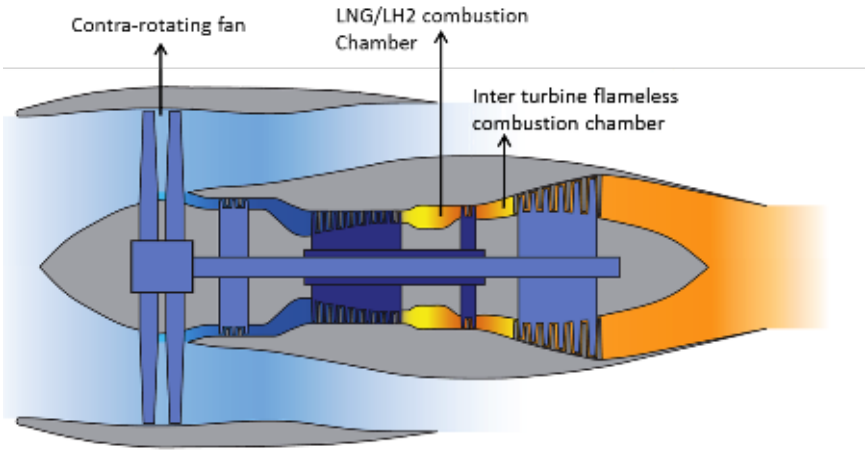

Figure 5.2: Schematic of the AHEAD hybrid engine (from [6])

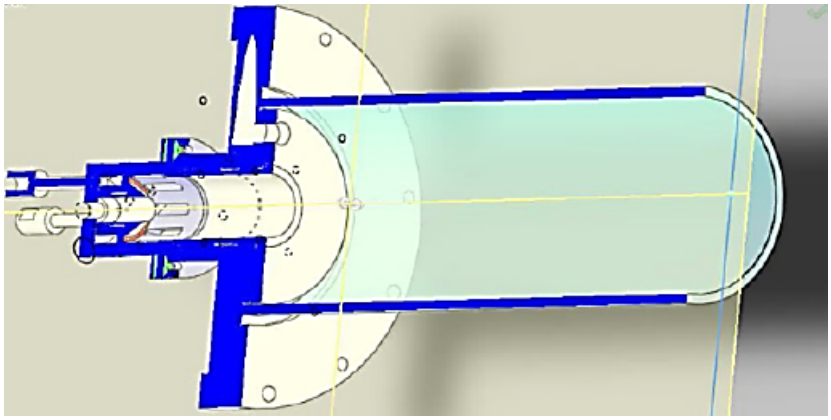

Figure 5.3: General layout of the hydrogen combustor (from [74])

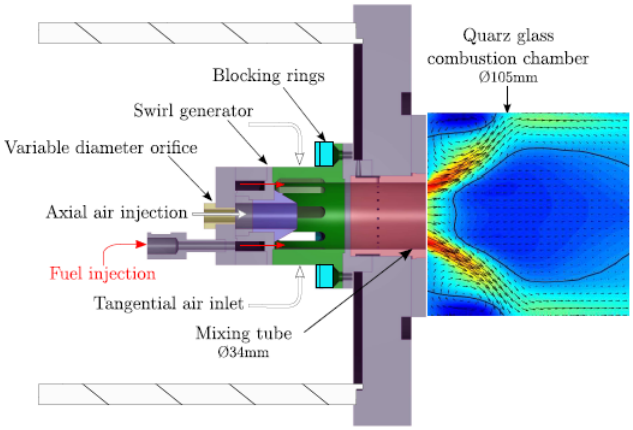

Figure 5.4: Schematic of the burner (from [76])

They identified the fuel–air momentum ratio J as the governing parameter for the evolution of x_F:

$$J = \frac{\rho_{fuel} u_{fuel}^2}{\rho_{air} u_{air}^2}$$

Their results are plotted in figure 5.5: it highlights an onset of major flow field changes around $J = 2$. The quantification of this axial flame base location will be used in the network to determine the reactors volumes.

Finally, a fundamental study of vortex breakdown mechanisms in swirling flows was performed by Terhaar et al. [78]. One result of interest they reported is the initial jet opening angle for a swirl stabilized burner with mixing tube and axial air injection. An image of the flame issuing from the experimental burner setup of TU Berlin can be seen in figure 5.6: it displays a cone shaped like geometry. This phenomenon will be used in the reactor volumes determination as well.

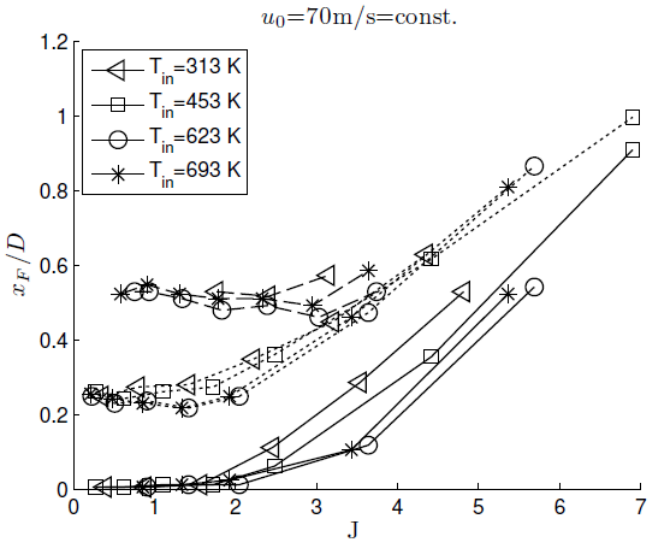

Figure 5.5: Evolution of x_F with J for various T_{in} and ϕ, for hydrogen and medium amount of axial air injection (solid) and high amount of axial air injection (dotted), and for methane at high amount of axial air injection (dashed) (from [77])

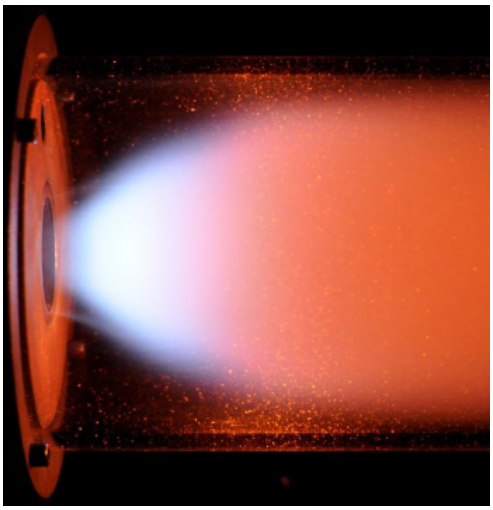

Figure 5.6: Flame shape and cone angle issuing from the designed lean–premixed burner (from [79])

5.3. Network architecture

The general architecture used is similar to the one proposed as default in the CHEMKIN software to simulate a gas turbine combustor [29]. It consists of a hybrid PSR–PFR network: a PSR cluster is used to model three main regions of the flow field directly after the nozzle (a mixing region, a flame/ignition region and a recirculation region) while a PFR is used for the post–flame region. Although the system studied is premixed, this basic arrangement models quite accurately the general flow field visualizations obtained experimentally. However, the mixing reactor does not represent a real mixing region in reality (premixed system) but represents the region of the flow between the nozzle and the flame front, where the mixture is not yet ignited. In the architecture presented it will however play the mixing role between fuel and oxidizer. This basic architecture also includes heat loss since the experimental setup loses a substantial amount of heat to its surroundings [80]. It is in this way different from the potential "real life" combustor, which is close to adiabatic conditions when dilution/cooling air is included in the heat balance. There is no dilution/cooling air stream on the experimental setup. The reactor network architecture is displayed in figure 5.7.

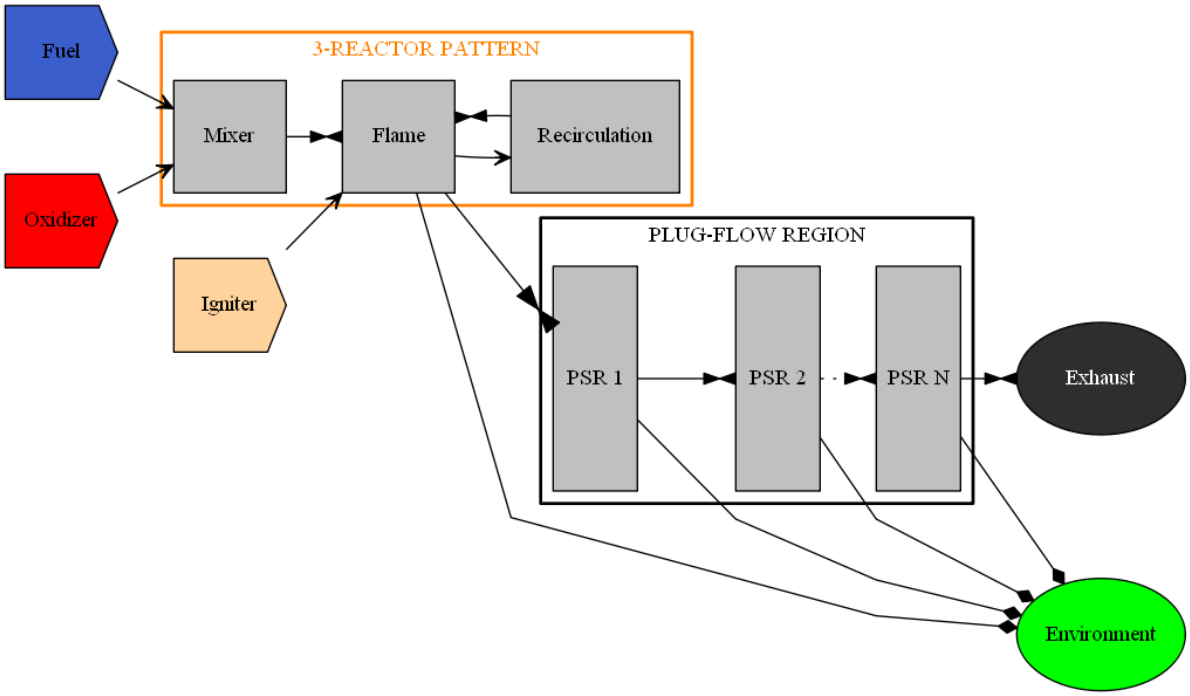

Figure 5.7: Basic architecture modeling the cryo combustor of the AHEAD engine: 3-reactor pattern (PSRs) + post-flame (PFR)

Similarly to the lifted flame model, an igniter inlet is carefully added to make sure the flame reactor ignites and the reaction is sustained while not impacting the steady–state solution.

A PFR model is compulsory in this case. An explanation of PFR modeling with Cantera is provided in appendix A.

The experimental setup is far from being adiabatic: implementing heat loss to the surroundings is also mandatory. The emission predictions are greatly impacted if no heat loss is modeled, which anyway would not represent accurately the experimental conditions. It is assumed that only the very hot regions lose heat to the surroundings: the flame and the PFR regions. A lump heat loss value (calibrated with experimental data) is assumed to be lost via a constant heat flux through the flame and PFR lateral areas. Equivalently this constant heat flux could be imposed on the recirculation and PFR reactors lateral areas (see appendix F) even though the flame reactor is physically the one along the combustor wall losing heat to the environment. An additional parameter allows to transfer part of the heat lost in the flame reactor to be lost in the PFR region, allowing in the extreme case for a constant heat loss flux only along the PFR walls. The influence of this parameter will be investigated.

Finally, the PSRs in the 3–reactor pattern region are constant volume PSRs. Rather than imposing the residence time in each, their volume is imposed. These volumes have to be determined with

consistency across the range of parameters that can be varied: reproducing the temperature–residence time characteristic of the actual flow is critical for emission prediction. The different volumes of the basic configuration are determined using the geometry depicted in figure 5.8.

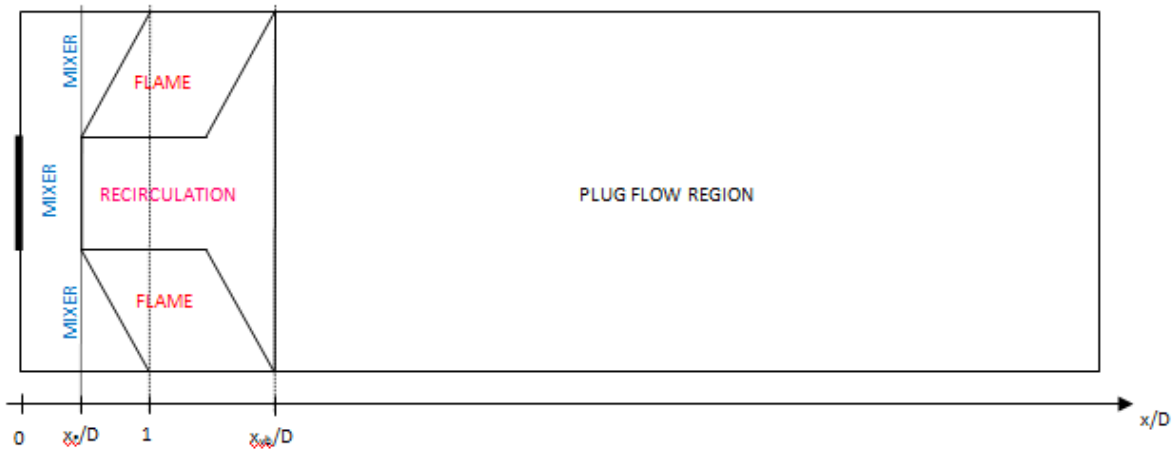

Figure 5.8: Determination of the reactors volumes

The mixer is considered to be the volume between the mixing tube nozzle and the flame front, after which the composition and temperatures will be radically different. To define the flame front, the x_F parameter is used in the width of the nozzle. On the side regions, the flame front is defined to be slanted, following the flow pattern general direction. The value of $\frac{x}{D} = 1$ is an approximated average value coming from mean flame probability fields reported in [77]. The flame reactor length is defined as $x_{vb} - D$, where D is the mixing tube diameter and x_{vb} is defined thanks to the initial jet opening angle θ_{vb} reported in [78] for an axial air injection of 12.5%:

$$\tan(\theta_{vb}) = \frac{D_{combustor} - D}{2x_{vb}}$$

The plug–flow region starts at axial positions after x_{vb}. Simple geometrical volumes are so defined, allowing easy computation of the volumes.

5.4. Model inputs

A summary of all the inputs of this reactor network model is provided in table 5.1.

The geometrical and internal parameters are set once and for all for this system since they are related to the system geometry and the iterative process to make the reactor network converge. Two thermodynamic parameters are also inherently constant: $T_{ambient}$ and LHV_{fuel}. Because of the specific implementation of the PFR in Cantera it is not possible to iterate the network as a whole, the PFR must be iterated on its own. However it is not problematic since there is no recirculation from the PFR to the PSR region. This specificity has two advantages: first it allows to use a large number of PSRs in the PFR discretization since they are solved in series, one at a time, which is extremely fast. Second, the convergence of the PSR cluster will quickly be reached as well, since it consists of only 3 PSRs. Then, because it is possible, a large number of PSRs is used to discretize the PFR: $N_{PSR} = 2000$. A very fine spatial resolution will be obtained, and the total simulation time (CPU time) of the model is in average 3 minutes only. Although such a fine resolution is not needed, a sufficient spatial discretization in necessary. This will be illustrated in the parametric study.

The operating conditions are defined by $T_{preheat,air}$, $\dot{m}_{air}$ and ϕ while T_{fuel} is determined by $T_{preheat,air}$ according to [77]:

$$T_{fuel} = T_{ambient} + 0.25\left(T_{preheat,air} - T_{ambient}\right) \tag{5.1}$$

The experimental setup is operated under atmospheric pressure.

The heat differential parameter Δ_{heat} introduces a degree of freedom in the heat loss implementation that will be exploited in a parametric analysis to assess the influence of the heat loss distribution.

GEOMETRICAL PARAMETERS
Combustor length $[m]$: $L_{combustor}$
Combustor diameter $[m]$: $D_{combustor}$
Mixing tube diameter $[m]$: D
Fuel ports diameter $[m]$: D_{fuel}
Fuel ports number: N_{fuel}
Initial jet opening angle [°]: θ_{vb}
THERMODYNAMIC PARAMETERS
Ambient temperature $[K]$: $T_{ambient}$
Air preheat temperature $[K]$: $T_{preheat,air}$
Fuel temperature $[K]$: T_{fuel}
Air mass flow rate $[kg/s]$: $\dot{m}_{air}$
Equivalence ratio: ϕ
Ratio of recirculating mass flow to flame inlet mass flow: $\dot{m}_{ratio}$
Fuel heating value $[MJ/kg]$: LHV_{fuel}
Heat loss ratio [%]: ζ
Heat loss differential [%]: Δ_{heat}
INTERNAL PARAMETERS
Valve coefficient $[kg/s/Pa]$: K_v
Iteration time step PSR region $[s]$: dt_{PSR}
Maximum simulation time PSR region $[s]$: t_{max}
Number of PSRs in the PFR: N_{PSR}
Maximum simulation time unit PSR in the PFR $[s]$: t_{max}^{unit}
Absolute tolerance for convergence criteria: abs_tol
Relative tolerance for convergence criteria: rel_tol

Table 5.1: Classification of the inputs of the cryo combustor model

HEAT LOSS CALIBRATION				
ϕ	$T_{exit}^{exp}\,[K]$	$T_{exit}\,[K]$	Calculated ζ [%]	$T_{exit}\,[K]$ (calibrated @ 35%)
0.4	1196	1545	30.9	1140
0.5	1323	1757	33.0	1288
0.6	1423	1948	35.3	1425
0.7	1502	2116	37.3	1551
0.8	1550	2259	39.5	1668

Table 5.2: Calibration of the heat loss model

Finally, $\dot{m}_{ratio}$ and ζ need to be calibrated before performing simulations for comparison purposes. This calibration is detailed in the next section. The definition of $\dot{m}_{ratio}$ is:

$$\dot{m}_{ratio} = \frac{\dot{m}_{flame \rightarrow recirculation}}{\dot{m}_{flame,inlet}} \tag{5.2}$$

with $\dot{m}_{flame \rightarrow recirculation}$ the mass flow rate from the flame reactor to the recirculation reactor and $\dot{m}_{flame,inlet}$ the mass flow rate entering the flame reactor. The heat loss of the system to the surroundings is defined using the heat loss ratio:

$$\zeta = \frac{\dot{Q}_{loss}}{\dot{Q}_{combustion} + \dot{Q}_{air} + \dot{Q}_{fuel}} \tag{5.3}$$

where $\dot{Q}_{loss}$ is the total power lost to the surroundings, $\dot{Q}_{combustion} = \dot{m}_{fuel} LHV_{fuel}$ the power released by the combustion and $\dot{Q}_{air}$ and $\dot{Q}_{fuel}$ the sensible heat of the air and fuel streams respectively.

5.5. Calibration

The combustor is burning pure hydrogen. The $C2\_NO_x$ mechanism is used for all the following simulations. The oxidizer is air taken as $(21\%\ O_2\ ;\ 79\%\ N_2)$.

5.5.1. Heat loss calibration

Experimentally determined exhaust temperatures are reported in [80]. The same equivalence ratio cases are simulated using the basic architecture without heat loss. The results are gathered in table 5.2. The heat lost to the surroundings by the combustor is significant. Furthermore it is not constant for all investigated ϕ, but the raw experimental data shows variations of the heat loss intensity even between experimental runs at same ϕ. For want of anything better, an average value of $\zeta = 35.0\ \%$ is adopted to be representative of the experimental conditions.

5.5.2. Recirculation intensity calibration

The recirculation intensity, governed by $\dot{m}_{ratio}$, can potentially impact the predicted emissions. Its main effect is to reduce or increase the residence times in the flame and recirculation reactors: if $\dot{m}_{ratio}$ increases, the mass flows through the reactors increase and consequently the residence times decrease (constant volumes), and inversely, potentially impacting the production of NO_x. A physically possible order of magnitude for this parameter is set to be $\dot{m}_{ratio} = 1.0$. A parametric analysis on its influence is performed for $T_{preheat,air} = 453\,K$, $\phi = 0.8$ and $\dot{m}_{air} = 130\,kg/h$: it is the most critical case in terms of NO_x production for which experimental data is available. It is then the more likely to display significantly any potential deviation. The results are displayed in table 5.3. The $NO_x = NO + NO_2$ emissions are corrected to $15\%\ O_2$ in the exhaust gas using equation 2.27.

It can be seen that the changes in residence times induced by a change in $\dot{m}_{ratio}$ in the range $0.25-4.0$ do not result in any significant change in the predicted emission for this critical case. This is not contradictory with the statement made on the residence time influence, it just means that the influence of this parameter is minimal. In fact if there was a trend to extract from these results, it would be a rather surprising one: the emissions would tend to increase with the recirculation intensity (decreasing residence times). This is a consequence of the constant heat loss flux from the flame reactor: while the mass flow across this reactor increases, the temperature decrease caused by the constant cooling is less intense ($\dot{Q} = \dot{m} C_p \Delta T$). As a result, the flame reactor temperature tend to increase, and because the temperature levels are typical of a dominant thermal pathway, the decreasing residence times are compensated causing a weak increase in NO_x production in the flame reactor NO_x^{fl}.

For the remaining simulations, a recirculation intensity of $\dot{m}_{ratio} = 1.0$ is assumed.

RECIRCULATION INTENSITY INFLUENCE						
$\dot{m}_{ratio}$	$\tau_{fl}\,[ms]$	$\tau_{rec}\,[ms]$	$T_{fl}\,[K]$	$T_{rec}\,[K]$	$NO_x^{fl}\,[ppmvw]$	$NO_x\,[ppmv@15\%O_2, dry]$
0.25	0.979	1.27	2060	2163	59	42.53
0.5	0.816	0.637	2061	2152	60	43.05
0.75	0.699	0.426	2061	2145	61	43.36
1.0	0.612	0.320	2062	2139	61	43.58
2.0	0.407	0.161	2063	2124	62	44.05
4.0	0.244	0.081	2066	2110	63	44.37

Table 5.3: Calibration of the recirculation intensity

5.6. Results: comparison with experimental data

The same parameter windows investigated during the experimental runs are simulated: $\phi = 0.3 - 0.8$ and $T_{preheat,air} = 313 - 703\,K$ for at constant inlet air mass flow rate $\dot{m}_{air} = 130\ kg/h$. The results are superposed with the measurements in figure 5.9. Although the general trends are reproduced (increasing emissions with increasing ϕ and $T_{preheat,air}$), the emissions are globally underestimated, and the deviation from the experiments increases with the equivalence ratio.

These results highlight the major influence of the combustion equivalence ratio and the air preheat temperature on the combustor's NO_x emissions. They indeed are prominent factors in the determination of the flame reactor temperature, itself a parameter of great importance as to NO_x production. A combined NO_x concentration / temperature profile across the different regions of the network shows as expected that the bulk of the predicted emission is produced in the flame (1) reactor (figures 5.10a and 5.10c for the PSR cluster, 5.10b and 5.10d for the post–flame region). It is also possible to notice that H_2 keeps being burned at the very beginning of the PFR.

In order to highlight the importance of the flame reactor temperature, the relative importance of the NO formation pathways in this reactor is investigated for the series at $T_{preheat,air} = 453\,K$ with $\dot{m}_{air} = 130\ kg/h$ and for a variable equivalence ratio $\phi = 0.3 - 0.8$ (figure 5.11). The pathways involved in this combustion process are: the thermal pathway, the N_2O–intermediate pathway and the NNH pathway. The fuel is pure hydrogen which prevents NO formation via the prompt and fuel pathways. Each of the three routes involved is alternatively dominant:

- The N_2O–intermediate route is dominant at $\phi = 0.3$. At this equivalence ratio, the flame reactor temperature is $1236\,K$, a temperature too low for the thermal pathway to activate. Although the NNH pathway contribution is not negligible, the rate constants of the formation reactions are extremely small, producing overall an insignificant amount of NO_x, below 1ppm. The NNH relative contribution is already important because the fuel used is pure hydrogen: even at low equivalence ratio a sufficient amount of hydrogen is present in the mixture to activate this particular pathway.

- From $\phi = 0.4$ to $\phi = 0.7$, the NNH route is dominant: hydrogen is increasingly available and the temperatures rise. It has several consequences, the first of which being the strengthening of the NNH pathway. Then, a second subroute of the NNH route activates from $\phi = 0.5$ due to a high enough temperature level:

  $$NNH + O \rightleftharpoons NO + NH$$

  It is also stimulated because this reaction is less exothermic than the main subroute:

  $$NNH + O \rightleftharpoons N_2O + H$$

  At $\phi = 0.6$, the flame reactor temperature reaches the $1800\,K$ threshold, and indeed the thermal pathway is shown to activate with a non negligible contribution. It is however still weak compared to the NNH contribution. And finally, from this equivalence ratio on, there is no NO formation via

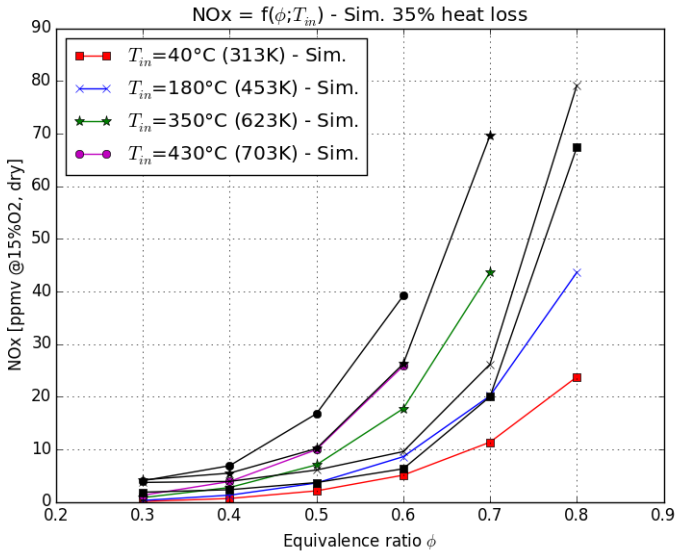

Figure 5.9: Comparison of NO_x predictions with experimental data for various ϕ and $T_{preheat,air}$ at constant $\dot{m}_{air} = 130\ kg/h$ ($\zeta = 35\%$, $\dot{m}_{ratio} = 1.0$) (the black signs are the corresponding experimental results from [81])

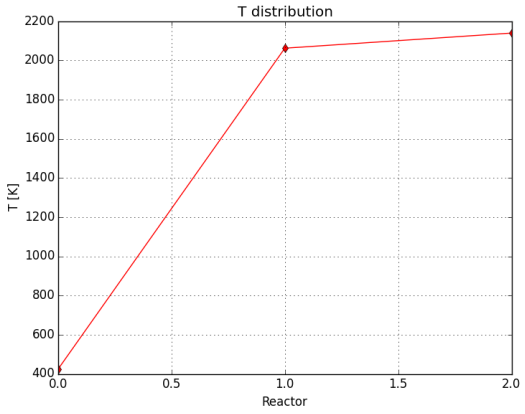

(a) Temperature distribution in the PSR region

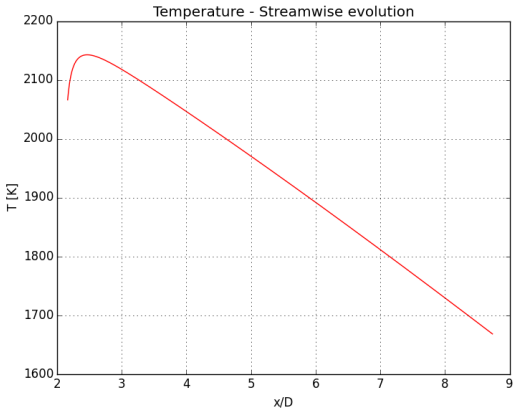

(b) Temperature distribution in the post–flame region

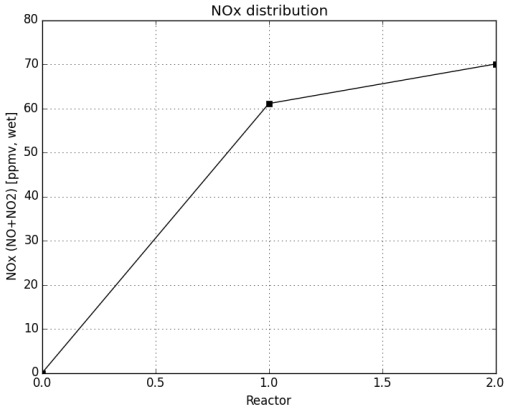

(c) NO_x distribution in the PSR region

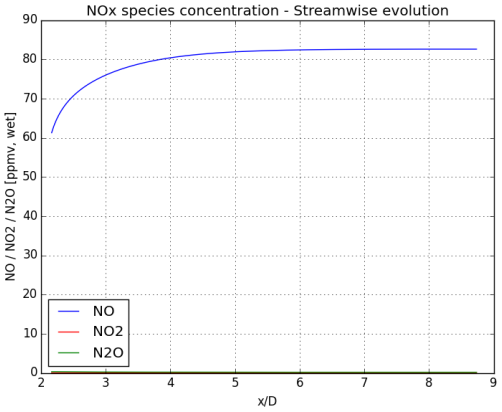

(d) NO_x distribution in the post–flame region

Figure 5.10: Temperature and NO_x distribution along the combustor for $T_{preheat,air} = 453\ K$, $\phi = 0.8$ and $\dot{m}_{air} = 130\ kg/h$ (Mixer: 0, Flame: 1, Recirculation: 2)

the N_2O–intermediate pathway anymore: the profusion of H radicals in the mixture stimulates the reduction of N_2O into molecular nitrogen.

- At $\phi = 0.8$ the temperature inside the reactor is now significant enough for the thermal pathway to just overcome the strength of the NNH pathway. In this case the highest level of emissions is reached for the conditions investigated.

This illustrates further the central role of the flame reactor temperature in the production of NO_x. The importance of the NNH route is not as an odd behavior as one would think: this combustion system operates under the most favorable conditions for this pathway to thrive. Pure hydrogen is burned under lean–premixed conditions, which means no prompt NO, negligible thermal NO up to a certain point, and a profusion of H and O radicals. Experimentally, the NNH pathway was evidenced in a low temperature, low pressure, rich premixed hydrogen–air flame [23] or in rich flames of H_2 and CH_4 at atmospheric pressure [24]. It has also been investigated numerically by Konnov et al. [82] for lean, steochiometric and rich mixtures $(0.7 - 1.3)$ of H_2–air in a well–stirred reactor of varying temperature $(1500 - 2200\ K)$ and residence time $(5\ \mu s - 100\ ms)$. In conditions comparable to the flame reactor for $T_{preheat,air} = 453\ K$, $\phi = 0.8$ and $\dot{m}_{air} = 130\ kg/h$ (the residence times in the flame and recirculation reactors are respectively $\tau_{fl} = 0.6\ ms$ and $\tau_{rec} = 0.3\ ms$), Konnov et al. found that the NNH pathway is prominent up to residence times of the order of $1\ ms$.

It has to be noted that the experimental measurement error can in average be taken equal to 5%. The predictions do not enter this interval, which means that the temperature levels are underestimated in the flame reactor.

Now that the importance of the combustion equivalence ratio and the air preheat temperature have been clearly noted, the behavior of the system will be investigated against the overall residence time (modified by varying $\dot{m}_{air}$), the heat loss intensity and distribution (ζ and Δ_{heat}) and the number of PSRs in the PFR discretization N_{PSR}.

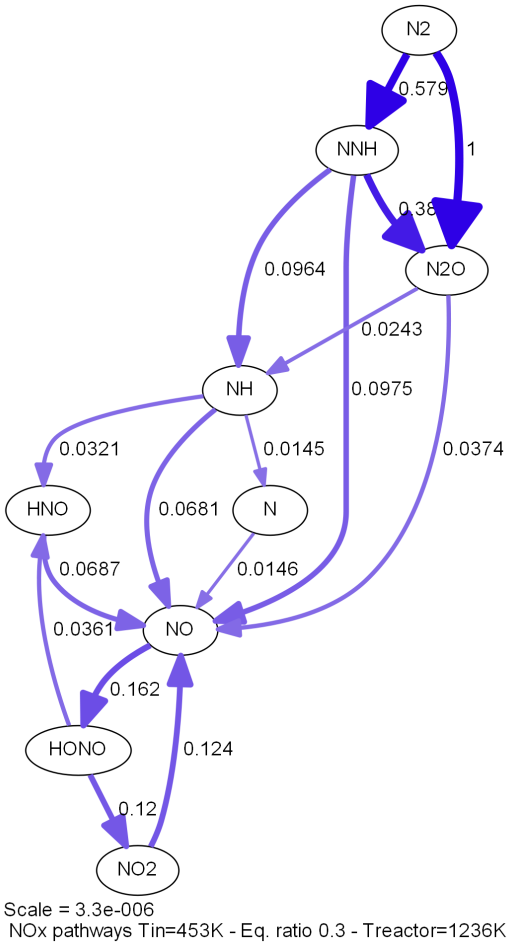

(a) $\phi = 0.3$ - $T_{flame} = 1236\,K$

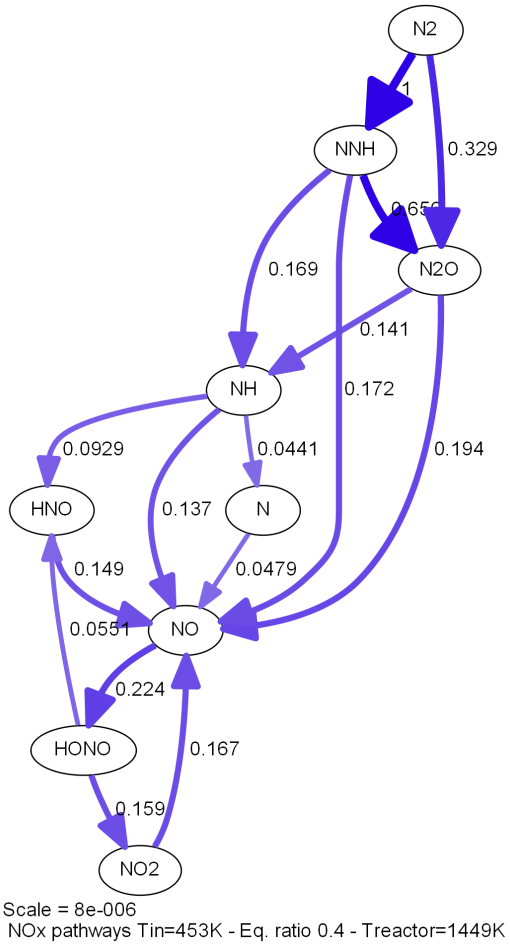

(b) $\phi = 0.4$ - $T_{flame} = 1449\,K$

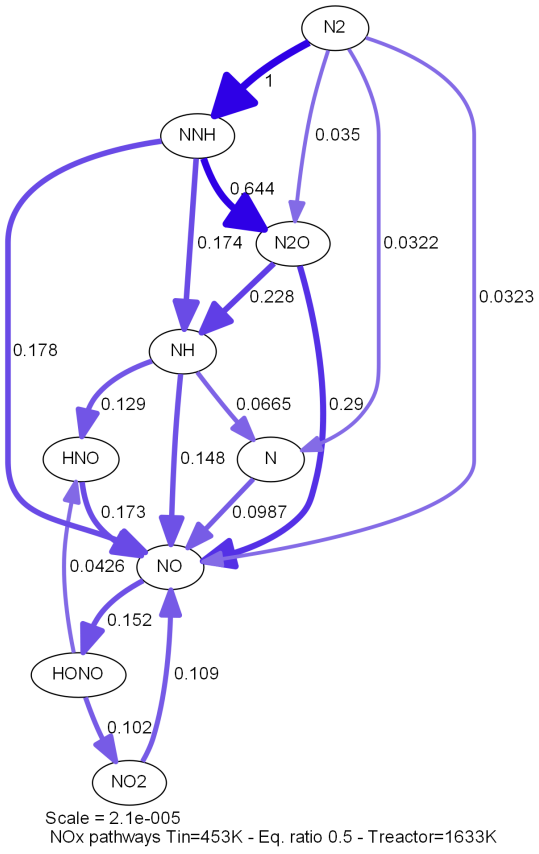

(c) $\phi = 0.5$ - $T_{flame} = 1633\,K$

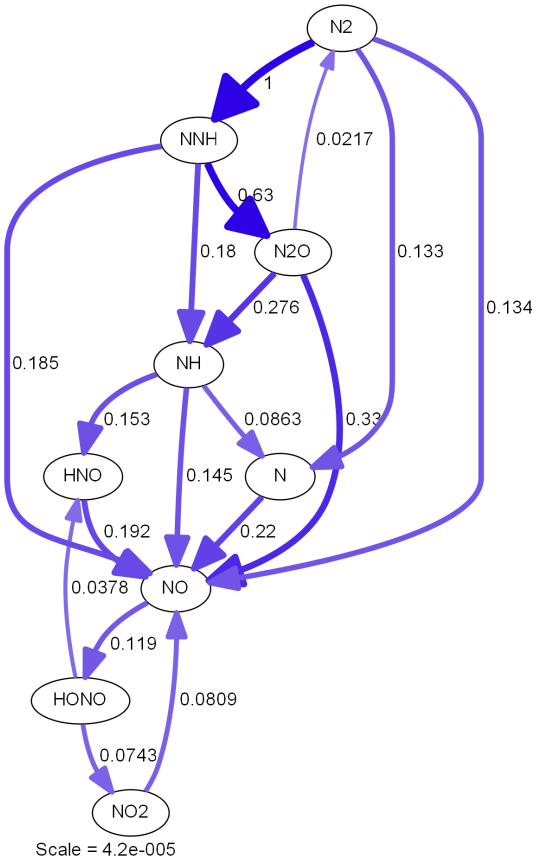

(d) $\phi = 0.6$ - $T_{flame} = 1796\,K$

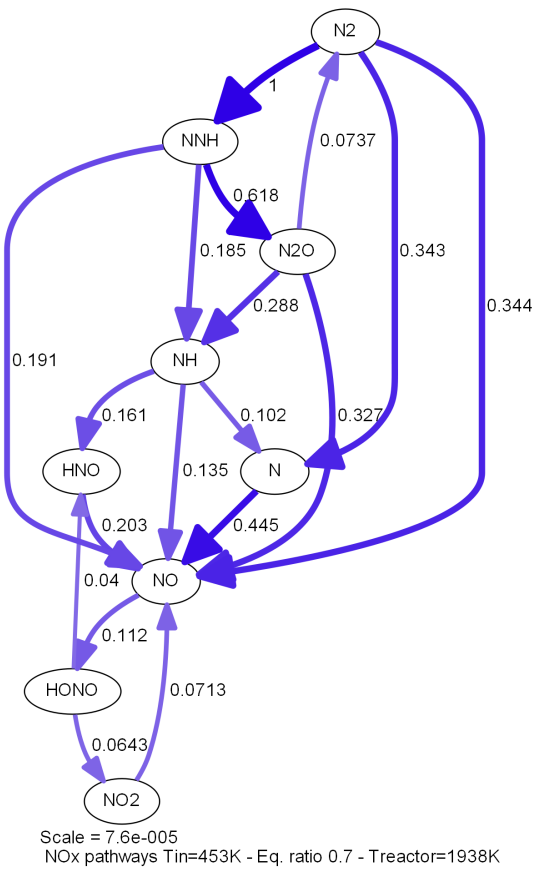

(e) $\phi = 0.7$ - $T_{flame} = 1938\,K$

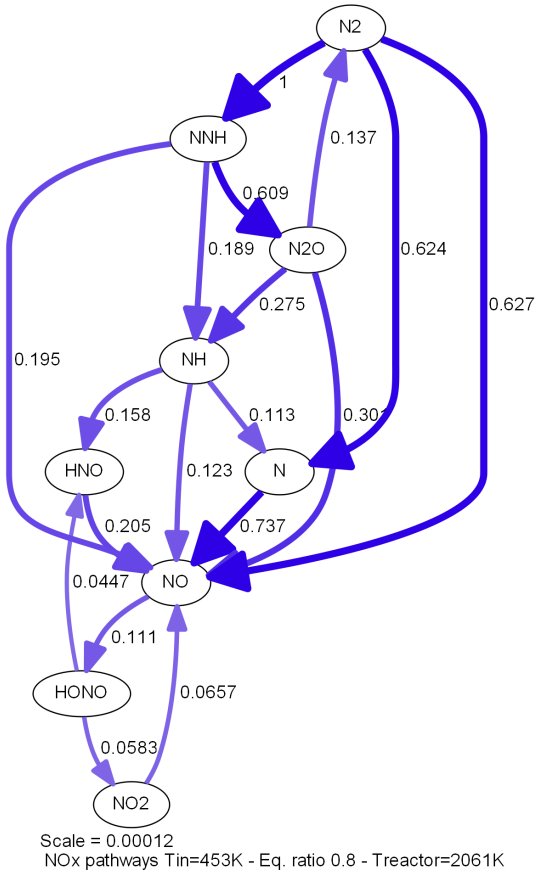

(f) $\phi = 0.8$ - $T_{flame} = 2061\,K$

Figure 5.11: NO_x pathway analysis for $T_{preheat,air} = 453\,K$ and $\dot{m}_{air} = 130\,kg/h$ on the flame reactor

INLET AIR MASS FLOW RATE INFLUENCE							
$\dot{m}_{air}\,[kg/h]$	$\tau_{fl}\,[ms]$	$\tau_{rec}\,[ms]$	$T_{fl}\,[K]$	$T_{rec}\,[K]$	$H_2^{fl}\,[\%]$	$H_2^{rec}\,[\%]$	$NO_x\,[ppmv@15\%O_2, dry]$
80	0.983	0.517	2089	2155	0.78	0.33	60.69
130	0.612	0.320	2062	2139	0.96	0.44	43.58
180	0.445	0.233	2040	2125	1.09	0.53	35.18
230	0.351	0.183	2023	2113	1.21	0.61	30.10

Table 5.4: Influence of the inlet air mass flow rate on the emissions in the critical case of $\phi = 0.8$ for $T_{preheat,air} = 453\,K$

5.7. Parametric study

5.7.1. Influence of the overall residence time: $\dot{m}_{air}$

The residence time in the hot regions plays an undeniable effect on the production of NO, especially when the thermal pathway is activated. Residence time changes in the reactors can also be obtained by varying the inlet air mass flow rate. The predictions variation is displayed in figure 5.12 for the series at $T_{preheat,air} = 453\,K$. The induced variations play no significant role at low equivalence ratio, when the thermal pathway is not activated. However, as soon as temperature levels get close to $1800\,K$ ($\phi = 0.6$) deviations appear between the constant mass flow predictions: at constant ϕ, the predicted emissions increase with a decrease in inlet air mass flow (increased residence time in hot regions). Moreover, not only the residence time increases, but the temperature levels as well: there is more time for the fuel to be burned, not compensated by the heat loss. To illustrate this double mechanism, table 5.4 gathers the hot reactors data. Between the two extreme cases, the flame reactor residence time is multiplied by 3 while its temperature increases by $65\,K$, producing eventually the double amount of NO_x.

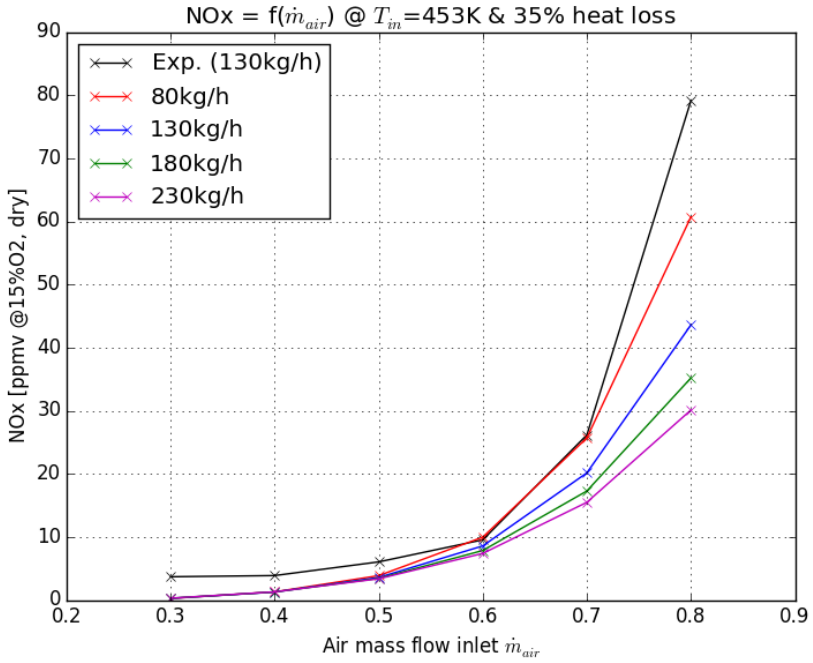

Figure 5.12: Influence of $\dot{m}_{air}$ on NO_x emissions for $T_{preheat,air} = 453\,K$, $\phi = 0.8$ and $\zeta = 35\,\%$

5.7.2. Influence of the heat loss intensity

To further confirm that the underprediction of NO_x at high equivalence ratio is due to the underprediction of the hot reactors temperatures, the heat loss ratio parameter ζ is reduced and its impact on the emissions is examined. As expected it can be seen in figure 5.13 that reducing the amount of heat extracted from the combustor globally raises the predicted emissions up to the measured values for $\zeta = 15\%$. This is true for the high equivalence ratios, meaning the equivalence ratios inducing temperatures typical of thermal NO activation in the flame and recirculation reactors. However the optimized value of 15% is not physically acceptable since the experimental combustor heat loss was estimated to be around 35%. Another way of increasing the temperature in the hot reactors has to be investigated: the introduction of the heat loss differential parameter Δ_{heat} in the model allows to do just that.

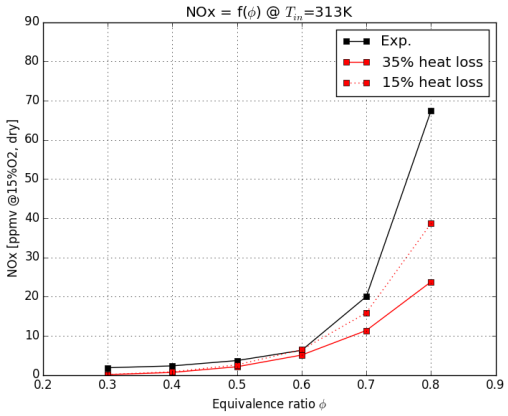

(a) Details $T_{preheat,air} = 313\,K$

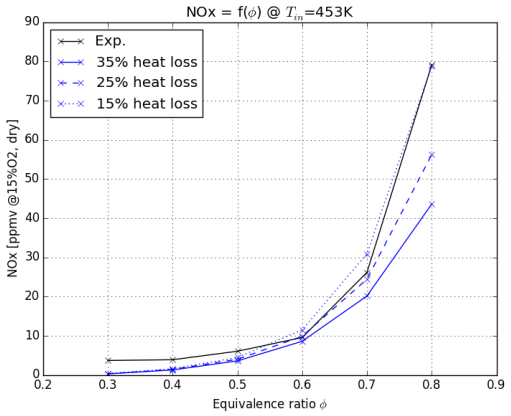

(b) Details $T_{preheat,air} = 453\,K$

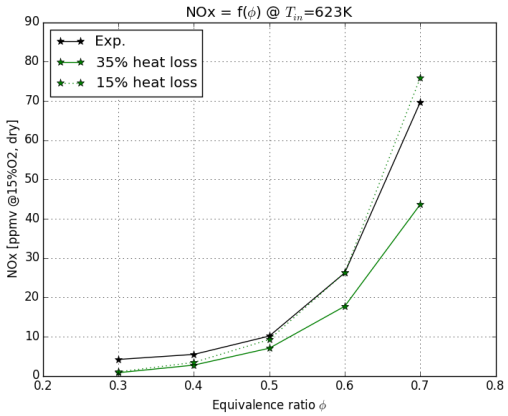

(c) Details $T_{preheat,air} = 623\,K$

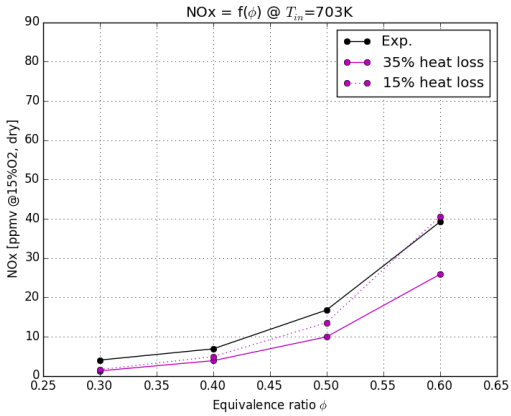

(d) Details $T_{preheat,air} = 703\,K$

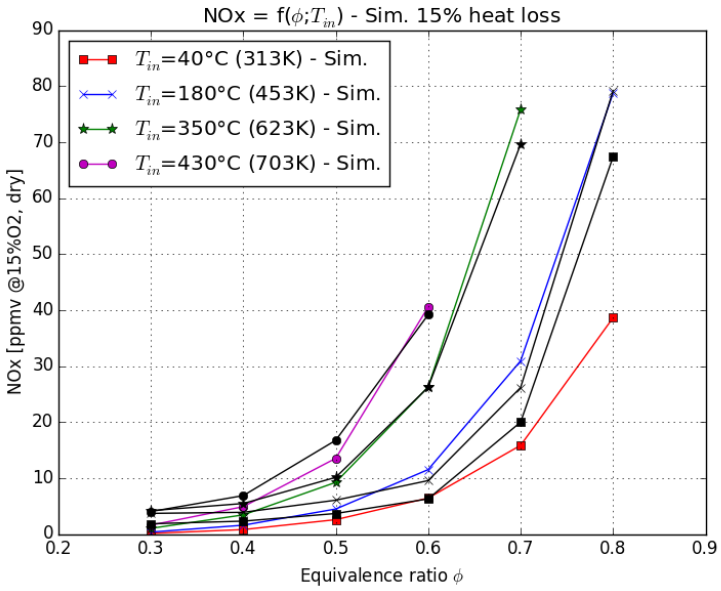

(e) All cases simulated with $\zeta = 15\,\%$

Figure 5.13: Heat loss intensity influence on the overall NO_x emissions

5.7.3. Influence of the heat loss distribution

Varying Δ_{heat} from 0% to 100% changes the heat loss distribution along the combustor:

- At $\Delta_{heat} = 0\,\%$, the heat loss is implemented using a constant heat loss flux through the flame and PFR reactors lateral walls.
- At $\Delta_{heat} = 100\%$, the same amount of heat loss is implemented using a constant heat flux through the PFR wall only. The flame reactor is no longer subject to heat loss.
- Intermediate values of the heat differential parameter allow to change gradually the heat loss load on the hot reactors in the PSR cluster.

It is expected that while the heat loss from the flame reactor decreases, its temperature would increase enough to counterbalance the slight decrease in residence time and produce more NO_x. One optimized value of the heat differential would hopefully yield predictions close to the experimental values. The evolution of the NO_x prediction for the case $T_{preheat,air} = 453K$, $\phi = 0.8$, $\dot{m}_{air} = 130kg/h$ and $\zeta = 35\%$ is displayed in figure 5.14. It turns out that the optimal heat differential is the one corresponding to a constant heat loss flux on the PFR wall only ($\Delta_{heat} = 100\,\%$), to simplify. The predictions for all cases are computed with this setting, producing very acceptable results shown in figure 5.15: the general trends are more closely predicted, despite a slight overestimation due to the simplified assumption of a constant heat loss flux on the PFR only. Furthermore, the quality of these predictions validates the reactor volumes determination process.

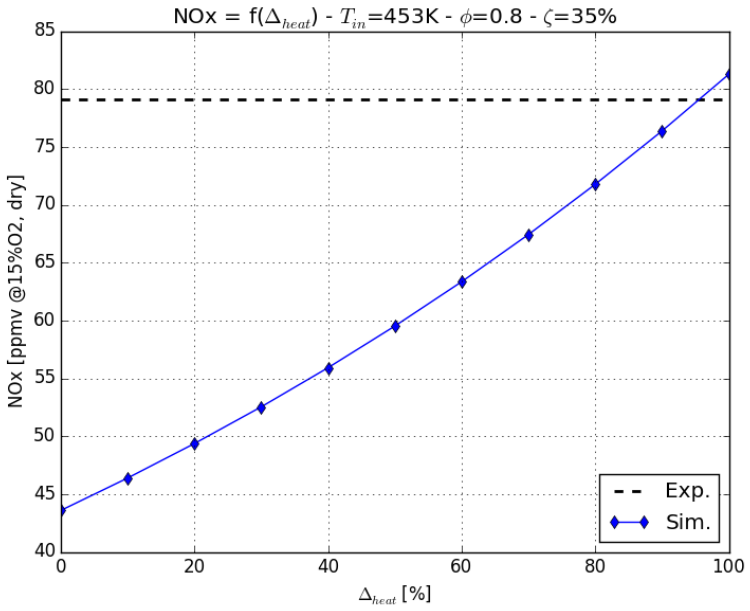

Figure 5.14: Influence of the heat loss distribution on NO_x emissions for $T_{preheat,air} = 453\,K$, $\phi = 0.8$, $\dot{m}_{air} = 130\,kg/h$ and $\zeta = 35\,\%$

5.7.4. Influence of N_{PSR}

It was mentioned in section 5.4 that a value of $N_{PSR} = 2000$ was used to discretize finely the PFR into a series of PSRs although it was not necessary to have such a fine discretization. This statement is now investigated with the aim to determine a minimum threshold value above which the predicted emissions are not affected but a further increase. The majority of the NO_x emissions are produced in the PSR cluster, but the participation of the initial region of the PFR cannot be neglected. A too rough discretization would not capture accurately the high temperatures in this initial region, resulting in an overall decrease of the NO_x predicted. Figure 5.16 gathers the results obtained varying N_{PSR} on the critical case $T_{preheat,air} = 453\,K$, $\phi = 0.8$, $\dot{m}_{air} = 130\,kg/h$, $\zeta = 35\,\%$ and $\Delta_{heat} = 100\,\%$. In order to have independent predictions from the model, a minimum value of $N_{PSR} = 100$ is necessary.

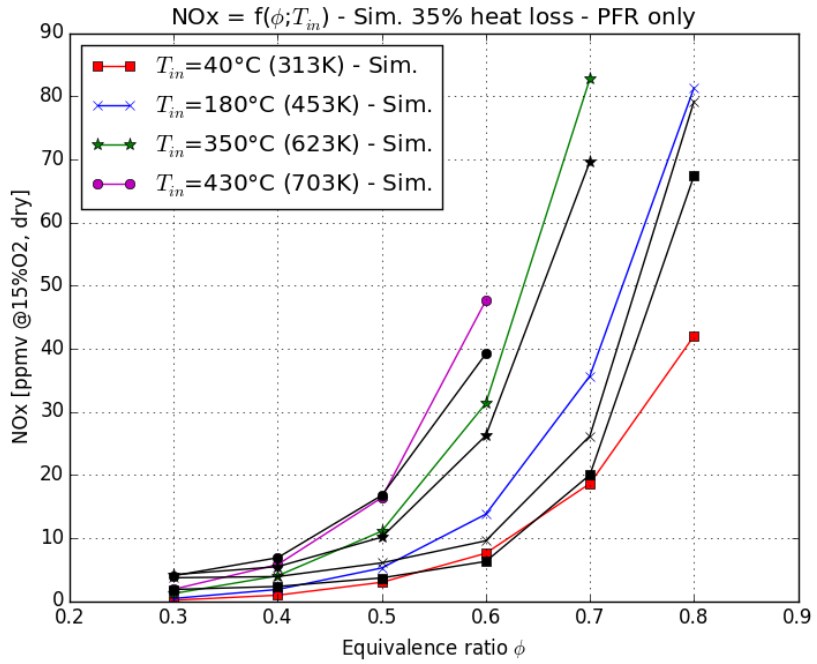

Figure 5.15: Influence of the heat loss distribution on NO_x emissions for all cases

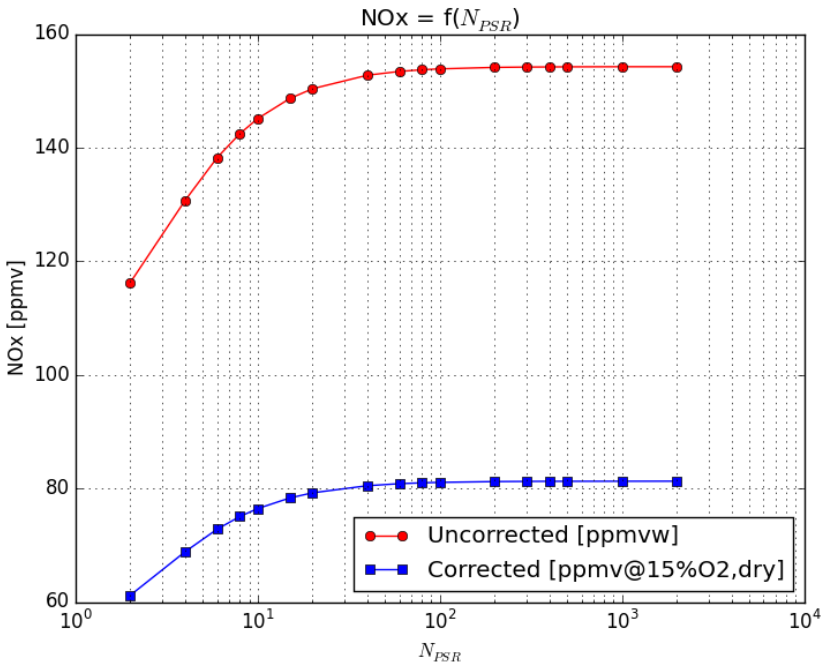

Figure 5.16: Influence of the PFR discretization on NO_x emissions

5.7.5. Conclusion

A reactor network capable of modeling accurately the NO_x emissions of the experimental lean–premixed combustor setup has successfully been built. The most influential parameters in terms of NO_x production in such a system have been identified:

- the heat loss intensity from the installation to its surroundings ζ ;
- the combustion equivalence ratio ϕ ;
- the air preheat temperature $T_{preheat,air}$;
- the heat loss distribution along the combustor Δ_{heat} ;
- the inlet air mass flow rate $\dot{m}_{air}$.

Their respective impact on the production of NO_x have been investigated, and they are all linked to one key parameter: the flame reactor temperature. This temperature setting is crucial because it impacts the relative intensities of the NO_x formation processes. Since the design objective is a very low NO_x combustor, the operating conditions must prevent at all costs a significant activation of the thermal pathway. A lean operating equivalence ratio has to be chosen in synergy with the level of air preheating, with a margin above the lean blowout limit (experimentally determined to be close to $\phi = 0.2$ [77]). Given typical pressurized air temperatures in gas turbines ($800 - 900\ K$) a reasonable order of magnitude for an operating equivalence ratio would be around $\phi = 0.4$.

5.8. Predictions from the real combustor in operating conditions

The final objective of the combustor design is to integrate it into a gas turbine. These final simulations aim at predicting the potential emissions of the real combustor in a gas turbine during operation. However, there are major differences between the experimental installation and the real combustor once integrated.

5.8.1. Differences with the experimental installation

Two major differences exist between the experimental setup and the integrated combustor:

1. In a gas turbine, the combustor is operated under very high pressures, while the experimental installation is at atmospheric pressure.
2. Because of the high temperature levels reached during operation, a gas turbine combustor requires cooling to maintain its structural integrity. The usual cooling method is to use part of the compressed air as dilution stream flowing around the combustor. It cools down the hottest parts and it is also gradually injected in the combustor, either as part of the combustion process (Rich Burn – Quick Quench – Lean Burn e.g.) or to dilute the flue gas to lower the average stream temperature. The combustor structure is also protected by film cooling, a layer of ”cold” air serving as buffer between the combustor wall and the very hot flue gas. Compared to the experimental installation far from being adiabatic, a gas turbine combustor can be considered (as a whole with the dilution stream) an adiabatic system.

Before being able to simulate the integrated combustor in operating conditions, the architecture developed and optimized in the previous sections needs to be modified to account for these differences. The high pressure modification is straightforward, only the reactors pressure need to be changed, essentially the inlet and exhaust reservoirs. The implementation of dilution air requires a modification in the architecture, displayed in figure 5.17. The dilution stream exchanges heat with the combustion stream all along the PFR while also being gradually injected inside, and it can also exchange heat with the flame reactor. It is implemented in 2 parts: first as a PSR being iterated with the PSR cluster, then as a PFR discretized with the same number of PSRs as the post–flame region. These two PFRs exchange matter and heat and are iterated in parallel.

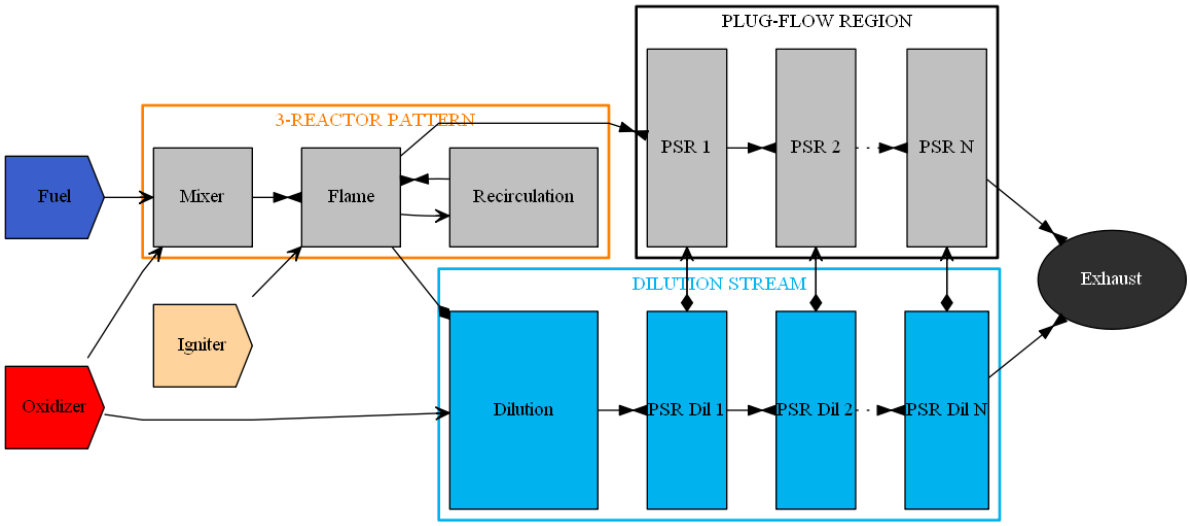

Figure 5.17: Architecture of the reactor network modeling the integrated combustor in a gas turbine

5.8.2. Simulation cases and parameters

Following the optimization steps of the previous sections, the number of PSRs in the discretization is fixed as $N_{PSR} = 100$ and no heat is exchanged between the flame and dilution reactors ($\Delta_{heat} = 100\%$). The heat loss intensity between post–flame region and dilution stream (ζ) can be varied. The total inlet air mass flow is separated in two streams: 85% goes into the combustion stream, 15% goes into the dilution stream. This split ratio can be varied.

The injection of dilution air in the post–flame region can be regulated and completely defined by the user. The choice made is to inject 40% of the total dilution stream in the first post–flame PSR (as dilution of the flue gas), then 5% distributed equally over the following 49 PSRs (modeling film cooling), then 40% as a whole again in PSR 51 (further dilution), and again 5% distributed equally over the remaining PSRs (film cooling of the second half). The remaining dilution air would be mixed with the combustion flue gas just after the combustor, before entering the high pressure turbine.

Preliminary simulations involving both heat exchange and gradual injection are launched and one major issue is encountered: in the last few PSRs, the dilution mass flow is very small and any heat transfer from the combustion stream to the dilution stream induces temperature levels not admissible. Moreover, the heat transfer is assumed to be unidirectional, from the combustion stream to the dilution stream, using the same implementation as previously: a constant heat flux along the PFRs wall. However because of the continuous decrease of the dilution mass flow and the continuous heat exchange, the dilution stream temperature becomes higher than the combustion stream temperature at some point along the PFR. This contradicts the heat loss model implementation. To circumvent this problem, choice is made to not use any heat transfer from combustion stream to dilution stream, the cooling of the combustion stream is realized only via the injection of "cold" dilution air: $\zeta = 0\ \%$. It is the worst case scenario for which the temperatures in the PFR are the highest.

Two flight conditions will be simulated: take–off and cruise. The predictions obtained will be compared to the predictions obtained using a reactor network as well [74][80]. The operation conditions for both flight conditions are given completely in [80]. In [74] slight differences in operating pressure and mass flows are reported for the same flight conditions, but the air and fuel temperatures are not indicated. The inlet air temperature is calculated using:

1. The barometric formula to obtain the atmospheric pressure at altitude h (in m) $p(h)$.

2. The classic linear decrease of temperature with altitude $T(h) = T_{ambient} - 0.0065h$ to obtain the atmospheric temperature at altitude h. The ambient temperature is set to $T_{ambient} = 300.0\,K$.

3. The atmospheric air at altitude h properties are accessed to compute the heat capacity ratio γ.

4. An adiabatic compression is assumed in the gas turbine compressor, giving:

$$T_{air} = T(h)\left(\frac{p(h)}{p_{combustor}}\right)^{\frac{1-\gamma}{\gamma}}$$

.

Take–off happens at altitude $h = 0\ m$, cruise at $h = 10000\ m$. The fuel temperature is assumed to be $T_{fuel} = 300.0\ K$ for all cases. The fuel burned is pure hydrogen.

The flight conditions parameters for the 4 cases that will be simulated are gathered in table 5.5

FLIGHT CONDITIONS SIMULATED						
Case n°	Flight condition	$p_{combustor}\ [bar]$	$T_{air}\ [K]$	$T_{fuel}\ [K]$	$\dot{m}_{air}\ [kg/s]$	$\dot{m}_{fuel}\ [kg/s]$
1	Take–off	51.23	935.58	300.0	57.59	0.5764
2	Take–off	51.6	923.69	300.0	55.23	0.514
3	Cruise	19.5	857	300.0	22.24	0.2024
4	Cruise	19.0	804.54	300.0	21.4	0.1798

Table 5.5: Take–off and cruise conditions simulated

5.8.3. Emission prediction of the operating combustor

These four cases are simulated and the results are compared with the reported predictions (obtained using a reactor network as well) in table 5.6. According to the model, the combustor would emit single–digit NO_x (in ppm) for both operating conditions simulated. Compared to the reported predictions, the take–off predictions are greatly underestimated (by one order of magnitude). On the contrary it could be considered that the cruise predictions and reported predictions are equivalent, both predicting very low NO_x emissions in the same order of magnitude (below $10\,ppm$). All these predictions cannot be verified with actual experimental data and are then purely speculative. They are however not surprising keeping in mind the main influencing parameters discussed in the previous sections. In all cases combustion occurs at very lean conditions ($\phi \approx 0.3 - 0.4$) and the inlet mass flows are huge: it contributes to very low levels of emissions. Only the air preheat temperature is quite high and would be pushing towards more NO_x production.

		EMISSION PREDICTIONS		REPORTED PREDICTIONS	
Case n°	ϕ_{comb}	$NO_x\ [ppmvw]$	$EINO_x\ [g/kg]$	$NO_x\ [ppm]$	$EINO_x\ [g/kg]$
1	0.401	6.70	0.992	74.7	xxx
2	0.373	4.10	0.649	xxx	4.5
3	0.365	3.76	0.608	8.88	xxx
4	0.337	1.67	0.290	xxx	0.7

Table 5.6: Emission predictions for the investigated take–off and cruise conditions

Additionally, the high pressure characteristic induces some changes in the NO_x formation processes. For all cases, the N_2O–intermediate pathway is clearly dominant, the other two pathways being completely negligible. The nitrous oxide formation route is favored at high pressures because of the three body reaction forming N_2O which initiates the mechanism. For the same equivalence ratios in the experimental setup (but lower inlet air temperature, meaning lower flame reactor temperature), the NNH pathway was either dominant, or at least a significant contribution to the total. Figure 5.18

displays the NO_x formation processes for case n°1 (take–off). A strong nitrous oxide pathway is depicted, as well as relatively weak thermal pathway. The NNH route is completely insignificant (not even represented in the figure because of the threshold settings).

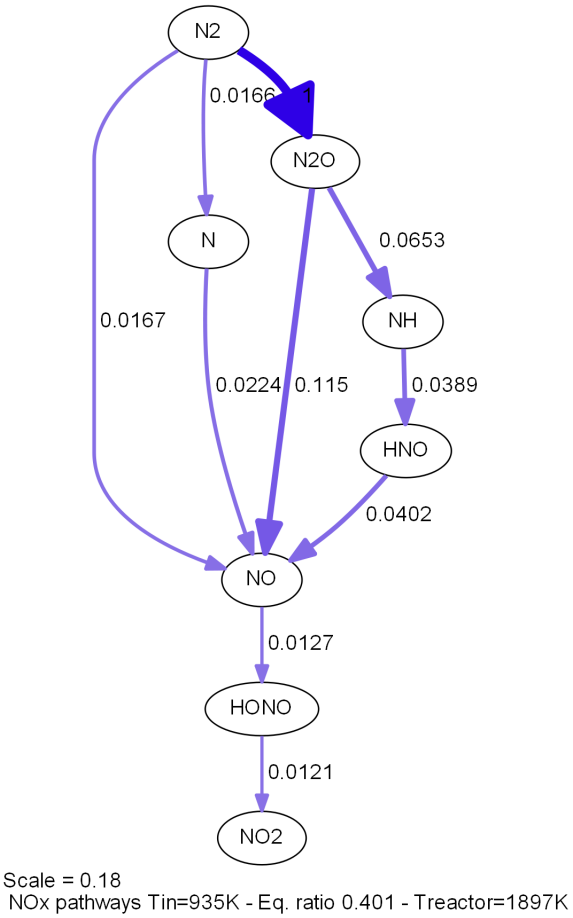

Figure 5.18: NO_x formation pathways for take–off conditions (case n°1)

5.9. Conclusion

The AHEAD europroject aims at designing an aircraft and its propulsion system able to meet the extremely stringent ACARE emission objectives. The proposed concept is a multi–fuel BWB aircraft powered by a revolutionary hybrid engine. One of the technologies used in the design of this aero engine is a hybrid dual combustion chamber combining the advantages of burning cryogenic fuel like LH2 and biogas while drastically reducing emissions of CO_2, CO, UHC, NO_x and soot compared to current existing technologies. Such abatement is allowed by the combustion modes chosen: the first combustor would burn cryogenic fuel in lean–premixed combustion, while the inter–turbine combustor would be fired with biogas/kerosene under flameless conditions.

A reactor network model of the first cryo combustor is built to investigate the major factors influencing its emissions. The predictions are compared with experimental data obtained using an installation emulating this combustor. Five influential parameters have been identified, all impacting a key characteristic in the network: the flame reactor temperature. This reactor is indeed where the bulk of the final NO_x emissions is produced. In parallel, the dominant NO_x formation processes for different conditions have been investigated. If the low emissions objective is to be met, a significant activation of the thermal pathway has to be prevented by a careful choice of the combustion conditions resulting from a synergy between air preheat temperature, combustion equivalence ratio and lean blowout limit.

The designed reactor network is adapted to model the same lean–premixed combustor integrated into a gas turbine. The potential emissions from this combustor in operation are simulated for two different flight conditions, take–off and cruise. For both conditions, the combustor is operated under high or very high pressures, with enormous inlet mass flows at very lean conditions. This leads to single–digit predictions of NO_x emissions (in ppm) for both take–off and cruise. The high operating pressure induces a change in the dominant NO formation route at the given equivalence ratios compared to the atmospheric installation: the N_2O–intermediate mechanism seems to be the most important NO_x source. However these predictions cannot be confirmed by experimental measurements.

The AHEAD cryo combustor has the potential to drastically reduce emissions in NO_x while eliminating any CO_2 or CO emission by burning hydrogen. Nevertheless, despite promising investigations of the safety limits on the designed combustor, the lean–premixed technology is not mature enough to be applied in aero engines immediately: the main criterion for a technology to be used in aviation is a proven safe operation, meeting extremely drastic safety standards.

6

Conclusion

The principal motivation inspiring the work performed during this master thesis is the need for fast and reliable emission estimators. A growing environmental concern stimulates research for new combustion systems, and such estimators could be put to good use during the design phase for instance. CFD is often the preferred modeling approach, leading to very acceptable results. However it has major drawbacks: a very high computational cost, preventing the use of detailed chemistry models. An alternative modeling method is Chemical Reactor Network (CRN) modeling. The force of this modeling method resides in the use of detailed chemistry while the required computational cost is much lower than for CFD. On the other hand, CRN modeling is not a perfect solution: methods exist to generate a reactor network from CFD results (obviously requiring a previous CFD study), and manually creating and calibrating a reactor network is very empirical. It often needs the contribution of experimental or numerical results. In this way, CFD and CRN modeling complement each other. Nonetheless, a nicely calibrated reactor network offers the possibility for fast and reliable emission predictions. The objective of this work was to apply CRN modeling to three different combustion systems:

1. A lifted jet flame in hot coflow.
2. A furnace with multiple regenerative flameless combustion burners: the 300kW furnace of the Process & Energy department of TU Delft (faculty of mechanical, maritime and materials engineering).
3. An innovative lean–premixed gas turbine combustion chamber burning cryogenic fuel: the high pressure combustor of the hybrid engine developed in the Advanced Hybrid Engines for Aircraft Development (AHEAD) project sponsored by the European Union, in which the Flight Performance & Propulsion department of TU Delft (faculty of aerospace engineering) is involved.

To generate and simulate the reactor networks, the open–source software Cantera [7] was used. Cantera is a suite of object-oriented software tools for problems involving chemical kinetics, thermodynamics and transport processes. It is a C++ based code, with interfaces for C++, Matlab® and Python. The Python interface was used. Another common software for reactor network modeling is CHEMKIN [25], which is licensed. In any case, using either software, a successful CRN modeling is in great part due to past experiences with this modeling technique. For this reason and in order to get familiar with both the software and CRN modeling in general, some results reported in the literature were reproduced prior to the work reported in this thesis.

6.1. Emission modeling of a lifted jet flame

A reactor network was first designed to model the specific NO_x emission behavior of a lifted jet flame in hot coflow reported by Fujimori et al. [59]: a decrease in the coflow temperature caused the liftoff height of the flame to increase and the NO_x production to suddenly drop under a certain temperature level. This reactor network is based on the combination of two models reported in the literature [55][60], adapted to the system of interest. This modeling was not successful, and several reasons were put forward to explain this failure:

- It is likely that the major physical phenomena involved change radically, causing the sudden drop in NO_x emissions. They may not have been identified or modeled correctly, and the modeling process adopted may not have been the most adapted: trying to model two potentially very different flames using a single reactor network architecture.
- CRN modeling may not be a suitable technique for such a system: the advantage of using reactor networks is important when the objective requires the use of detailed chemistry (like emission prediction), but it also does not model turbulence and uses a rough discretization of the flow field. It would appear that the interaction between flow field, turbulence and chemical reactions is too important for a lifted flame to be omitted in the modeling.

Finally, the experience gained with the subsequent modelings allowed to identify potential improvements for the reactor network concerning the complexity of the architecture and its simulation time.

6.2. Emission modeling of a flameless furnace

Lifted jet flames setups were created to emulate a relatively new combustion mode discovered in the 1990s (flameless combustion) in order to investigate the fundamental physics involved. In fact, flameless combustion had been already used in industrial applications before a thorough understanding of this combustion process was gained because of its incredible qualities: a very low emission combustion mode combined with a high thermal efficiency, displaying a uniform temperature field over large volumes, allowing the use of low calorific value fuels and providing excellent safety during operation. It was first applied to furnaces, most probably because the already existing installations could be used in flameless mode provided only a retro–fitting of their burners. The second combustion system proposed for CRN modeling was the experimental furnace of TU Delft, a multiple burner setup allowing for various firing configurations.

The inherent characteristics of flameless combustion make it very friendly as to CRN modeling. Moreover the physical phenomena behind the flameless burners design are well–defined: separate high velocity injection of fuel and oxidizer inside hot flue gases. However, a detailed experimental and numerical study by Danon [5] revealed a rather complex flow field as well as interactions due the various multiple burners arrangements: the TU Delft furnace is not a priori the perfect candidate for CRN modeling, even if it is operated under flameless conditions. A much simpler flameless furnace configuration was modeled by Mancini et al. [62] using a reactor network: the International Flame Research Institute (IFRF) furnace. Their reactor network was calibrated using experimental and numerical results obtained on the same setup. In parallel an extensive literature study on flameless combustion allowed to identify the keys to a good modeling of this combustion mode in furnaces:

1. An accurate combined prediction of the position at which the fuel and oxidizer jets mix and of the amount of hot flue gas they entrained in the meantime.
2. Heat losses to the surroundings are integral part of the overall decrease in temperature level displayed in flameless combustion systems.

A reactor network was then designed, based on the general architecture reported by Mancini, but modified to circumvent the use of the specific experimental and numerical data to calibrate it. Two analytical submodels were then developed to fulfill the first requirement for accurate modeling: the Bending Model predicts jets trajectories and their convergence point, while the Shielded Entrainment Model gives access to the amount of gas entrained by jets in a SJ/WJ configuration, typical of the flameless burners.

The resulting designed network has the potential to be adapted to any flameless furnace, provided simplifications in some complex cases. The performances of this network (emission prediction and simulation time) were tested on three very different flameless furnace installations: the semi–industrial IFRF furnace, the laboratory scale flameless furnace of the University of Mons studied at length by Lupant [20], and finally the TU Delft furnace. For all three setups, the reactor network predicted emissions for CO and NO_x of good quality, in the same order of magnitude as experimental measurements if not really close to them, and reproducing the correct trends. In addition the required simulation times were very reasonable compared to any CFD simulation, in average in the order of $4-5\,h$ on a seven–year–old laptop. These results are extremely promising: they confirm the versatility and adaptability of

the network which is not restricted to model a particular installation, and quality predictions could be obtained despite necessary approximations and assumptions as well as several identified weaknesses of the analytical sub–models. Improvements in the entrainment sub–model and a more advanced heat loss model would certainly be beneficial and increase both the network's accuracy and stability. Finally, one particular reactor was identified to be central to the emission modeling: the mixer reactor where fuel and oxidizer jets mix and ignite. Its temperature / residence time characteristics showed to influence both investigated pollutants.

6.3. Emission modeling of an innovative gas turbine combustor

The third and final part of this thesis' work deals with the CRN modeling of a lean–premixed combustor firing cryogenic fuel, designed as part of the AHEAD europroject. Experimental results have already been obtained on a real size setup. The aim of the modeling is twofold: first reproducing the experimental results accurately, but also investigating the major parameters of influence on the combustor emissions. Contrary to the previous network modeling flameless furnaces, this network is designed to be system specific. A rather simple architecture was used and once properly calibrated for heat loss, it yielded extremely satisfying results:

- The simulation time is extremely fast, only a couple minutes are needed to obtain a prediction.
- The trends and emission levels measured experimentally were reproduced.
- Five parameters were identified to be very influential on the amount of NO_x produced: the air preheat temperature, the combustion equivalence ratio, the magnitude of the inlet air mass flow and the heat loss intensity and distribution.

These parameters directly influence the key characteristic of the network: the flame reactor temperature, itself directly impacting the relative intensities of the NO_x formation processes. The results obtained provide a good insight on the physics controlling the designed combustor experimental installation.

As a concluding work, purely predictive simulations were launched on a modified network, modeling the same combustor integrated in a gas turbine. Take–off and cruise conditions were simulated and both resulted in very low levels of NO_x emission, under 10 ppm. It seems to be promising as to the potential future implementation of the technology, although the (thankfully) drastic safety standards of the aviation industry will make this a long and winding road.

A

Guide of good practices using Cantera

Cantera is a very powerful software provided one makes good use of it. During the modeling work of this thesis, some time–consuming software related problems were encountered. Although the online documentation was more than often of great help, certain important details are not mentioned there. In order to save the trouble to potential Cantera users reading this thesis they are listed in this chapter, along with the solution adopted to overcome them.

A.1. Miscellaneous

First of all, the online documentation is updated according to the latest *stable* release of Cantera. Making sure to work on the latest stable version ensures consistency with the documentation and allows one to use the newest implemented capabilities.

There are four types of Perfectly Stirred Reactors offered to use in Cantera: Reactor (constant volume), ConstPressureReactor, IdealGasReactor (constant volume) and IdealGasConstPressureReactor. The solver is more stable and reliable for the ideal gas reactors, constant volume or pressure. If the application allows it, they should be preferred.

One particularly treacherous error encountered is related to the valve coefficient. One way to maintain the pressure constant across a network of constant volumes reactors is to interconnect them with valves or pressure controllers. A common argument to these two flow controller types is the valve coefficient $K_v\ [kg/s/Pa]$. In order to keep the pressure drop between two consecutive reactors to a minimum, the valve coefficient should be set to a high value. But it also has to respect some boundaries because it impacts the stiffness of the system of equation to solve. The solver used by Cantera is of course able to handle stiff problems, but up to a limit. A too high value of K_v makes the system too stiff and the solver crashes without giving proper notice for it. A good rule of thumb to determine a value of K_v keeping a constant pressure across the network and keeping the solver from crashing is:

$$\frac{K_v}{\dot{m}_{network}} \sim 1\ Pa^{-1} \tag{A.1}$$

with $\dot{m}_{network}$ the main mass flow across the network.

Finally, to be sure not to run into misallocation problems, a good policy is to create a dedicated gas object for each created reactor. It may sometimes be constraining but it keeps away errors that may not be easy to debug after the fact.

A.2. The Plug–Flow Reactor in Cantera

Cantera does not have a Plug–Flow Reactor object. There are in total four ways to model a plug–flow region with Cantera:

1. Using a single PSR: it is a very rough approximation, but it might work in some cases, and heat loss is possible to implement using a Wall object. A PSR object is perfectly compatible and interacts with a Wall object.

2. Using the FlowReactor class: contrary to what is written just above, this object models a PFR but the development of this class is not really advanced and the capabilities of the FlowReactor are very limited, making its use marginal. It models a constant cross section adiabatic PFR, taking a gas object at the beginning and following its spatial evolution (1D only) by converting a time iteration into distance traveled. The FlowReactor is also a steady state model and cannot be integrated into a network: it has to be solved on its own. Related to this problem is that while the FlowReactor class is compatible with Walls, it does not interact with them. This means that one can specify a heat loss as high as one wants between a FlowReactor object and another reactor via a Wall object, nothing is going to happen and the FlowReactor will retain its adiabatic characteristic. Additionally no error will be raised since classes FlowReactor and Wall are compatible.

3. Using the Lagrangian particle simulation: it is the same approach as the FlowReactor class, but one has to code it by hand using a PSR. One drawback of using this method is the unknown spatial discretization prior to simulation: the reactor is iterated in time, converted in velocity, in turn converted in distance.

4. Using a series of PSRs: this method is the preferred (and recommended in the documentation) method to implement a PFR in Cantera. A plug–flow region is approximated by a multitude of PSRs in series, discretizing spatially the region to model: contrary to the previous method the spatial discretization is then known a priori. The PSRs are integrated one at a time until steady state, starting with the first in the chain. Once it is integrated from inlet composition to steady state, the second reactor is iterated from this new composition to steady state and etc... Because of this particular integration and because it is made of PSRs, a PFR implemented with this method can be fitted with heat loss or gain through its side wall: each PSR is coupled to a Wall object with which it can interact perfectly. This is the method used in this thesis.

B

Calibration of the lifted jet flame reactor network

The reactor network designed to model the lifted jet flame system needs to be calibrated regarding three parameters:

- $L_{pattern}$;
- n_{PSR}^{post} ;
- χ.

B.1. Calibration of $L_{pattern}$

An internal function of the model is used to determine the amount of core mass flow debited from the core reactor necessary to maintain a stoechiometric condition in the flame sheet (before ignition). A saturation is implemented so that a trial-and-error process can be used for each case to determine $L_{pattern}$ with a $1\ mm$ precision.

B.2. Calibration of n_{PSR}^{post}

n_{PSR}^{post} is calibrated using a reference case: case n°3. It results in a reactor density setting for the post–ignition region. The same density is used for all other cases, approximately, in order to have a round number of reactors.

The evolution of $EINO_x$ and CPU time with a varying number of reactors in the post–ignition region is displayed in figure B.1. Several comments are on the agenda:

1. The number of reactors in the post–ignition region is—as expected—affecting greatly the predicted emissions, especially in the lower range of reactor number. An increase from 2 to 5 reactors $(+150\%)$ results in tripling the predicted emission index $(+200\%)$. However increasing from 5 to 15 reactors $(+200\%)$ yields a smaller increase of 37% in $EINO_x$. Finally an evolution from 10 to 15 reactors $(+50\%)$ induces a marginal increase of 7% in predicted emission index.
2. This evolution has to be analyzed along with the simulation time. The CPU time only doubles between 10 and 15 PSRs but from $4h$ to $8h$, while it increases by more than 400% between 2 and 5 PSRs but keeping very acceptable simulation times $(1h)$.

Given these results, the best trade–off was decided to be at a value of $n_{PSR}^{post} = 10$ for case n°3, which gives a discretization length of $33\ mm$ or a corresponding reactor density in the post–ignition region.

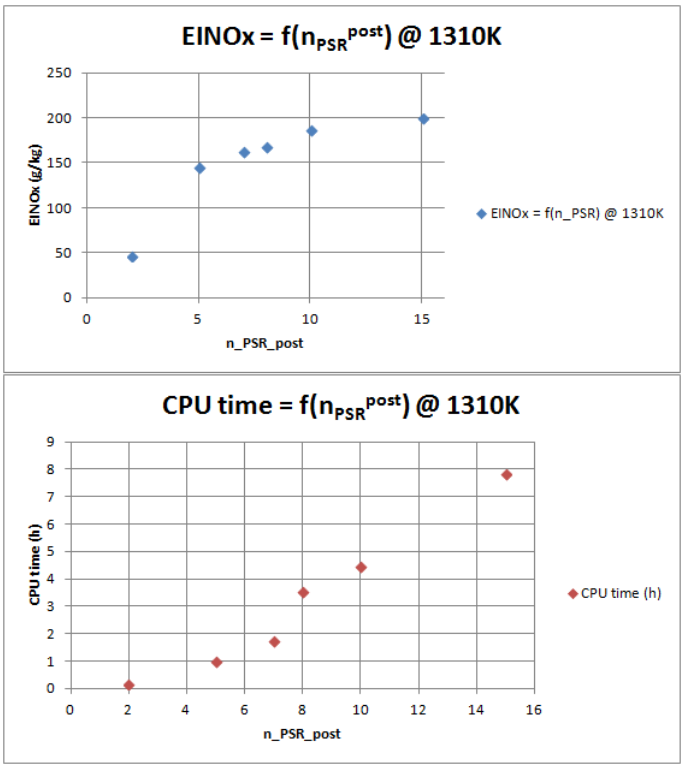

Figure B.1: Evolution of $EINO_x$ and CPU time against n_{PSR}^{post} for the reference case

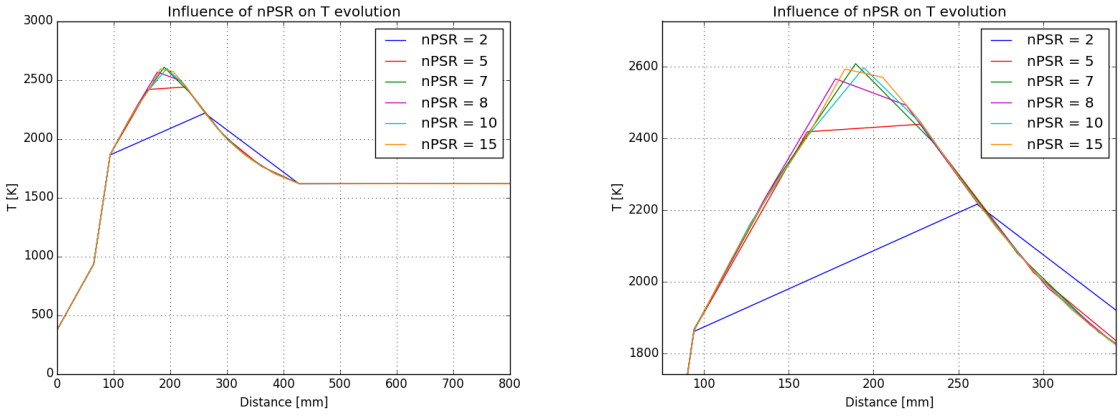

(a) Temperature profile along the duct (b) Detail of the peak region

Figure B.2: Influence of the post–ignition region discretization on the temperature profile

To illustrate the influence of the discretization of the post–ignition region on the predicted emissions, the evolution of the temperature profile along the combustion duct for an increasing n_{PSR}^{post} is displayed in figure B.2. A small number of PSRs does not capture the temperature profile accurately enough. Hence the high temperature regions, location of the bulk of the NO_x production, are not resolved. It can be seen indeed that the peak temperature is ”eroded” when the number of PSRs is not high enough. The temperature level in the peak region is consistent with thermal NO production, explaining the large discrepancies in $EINO_x$ once the peak starts to be captured.

B.3. Calibration of the radiant fraction

The radiant fraction is adjusted to match the predicted and experimental $EINO_x$ for the reference case. The same amount of heat loss is used for all other cases, adjusting automatically the average emissivity of the core gases. The radiant fraction is gradually increased and an optimized value is found to be $\chi = 32.25\ \%$ (see figure B.3). Not surprisingly since thermal NO dominates, the production of NO_x decreases when the amount of heat loss increases.

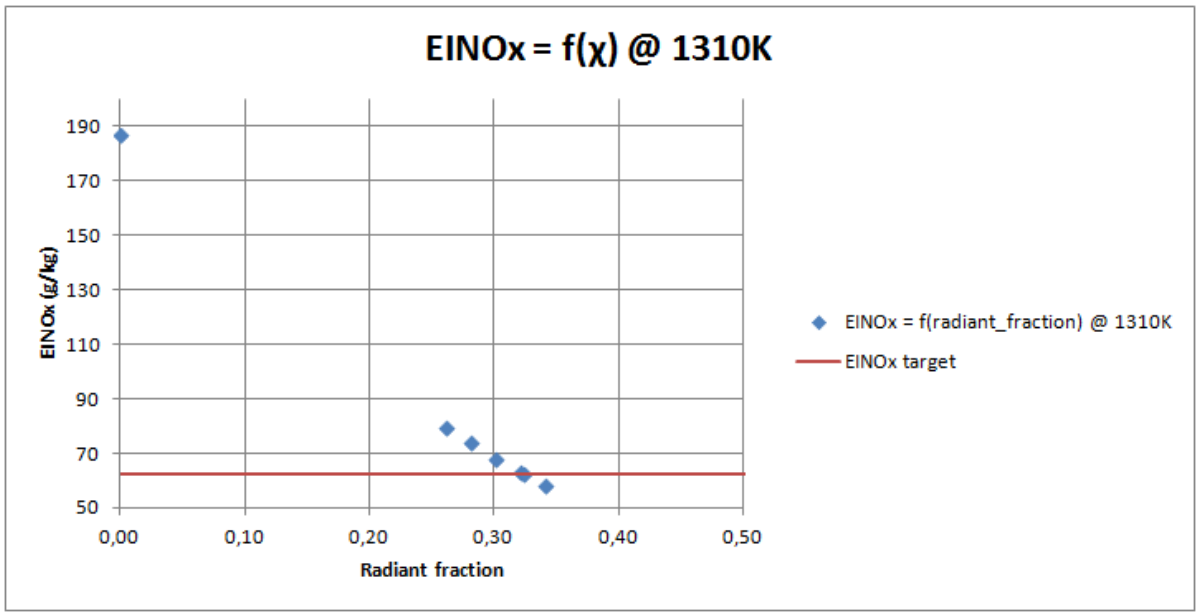

Figure B.3: Evolution of $EINO_x$ with an increasing radiant fraction for the reference case

This concludes the lifted jet flame reactor network calibration.

C

Bending Model development

C.1. The dual–hole configuration: 5 possible integration modes

C.1.1. The slope approximation

During the develompent of their Bending Model, Faghani and Rogak [71] assume local angles between the trajectory and the horizontal direction small enough to able to use Taylor series and the slope approximation:

$$\frac{dy_{cs}}{dx} = \tan(\theta) \approx \theta \tag{C.1}$$

However no precision is given on how the integration is performed. The method used in this thesis is to transform the system of two 2nd order ODEs into an equivalent system of 1st order ODEs, so that a built–in Python library can be used for the integration. However the variable change needed for the mathematical transformation raises interrogations about a further use of the slope approximation.

The original reported system of ODE is obtained using the slope approximation once (refer to section 4.3 for the notations):

$$\begin{cases} \dfrac{d^2y_{cs,1}}{dx^2} &= -\dfrac{y_s + R}{y_s}\dfrac{K_e^2}{2\pi y_s}\dfrac{\cos^2(\theta_1)}{\cos^2(\theta_{0,1})}\sqrt{\dfrac{\dot{G}_{0,2}}{\dot{G}_{0,1}}} \\ \dfrac{d^2y_{cs,2}}{dx^2} &= +\dfrac{y_s + R}{y_s}\dfrac{K_e^2}{2\pi y_s}\dfrac{\cos^2(\theta_2)}{\cos^2(\theta_{0,2})}\sqrt{\dfrac{\dot{G}_{0,1}}{\dot{G}_{0,2}}} \end{cases} \tag{C.2}$$

The variable change used for the mathematical transformation is:

$$Z = (z_0, z_1, z_2, z_3) = \left(y_{cs,1}\,;\ \frac{dy_{cs,1}}{dx}\ ;\ y_{cs,2}\,;\ \frac{dy_{cs,2}}{dx}\right) \tag{C.3}$$

From this point, two choices are possible:

- Either using the slope approximation a second time and replace θ_i in the trigonometric function directly by $z_{1/3} = \frac{dy_{cs,i}}{dx}$. The obtained system is termed **"model 2"** for using the slope approximation twice:

$$\begin{cases} \dfrac{dz_0}{dx} &= z_1 \\ \dfrac{dz_1}{dx} &= -\dfrac{z_0 - z_2 + R}{z_0 - z_2}\dfrac{K_e^2}{2\pi(z_0 - z_2)}\dfrac{\cos^2(z_1)}{\cos^2(\theta_{0,1})}\sqrt{\dfrac{\dot{G}_{0,2}}{\dot{G}_{0,1}}} \\ \dfrac{dz_2}{dx} &= z_3 \\ \dfrac{dz_3}{dx} &= +\dfrac{z_0 - z_2 + R}{z_0 - z_2}\dfrac{K_e^2}{2\pi(z_0 - z_2)}\dfrac{\cos^2(z_3)}{\cos^2(\theta_{0,2})}\sqrt{\dfrac{\dot{G}_{0,1}}{\dot{G}_{0,2}}} \end{cases} \tag{C.4}$$

- Or using a trigonometric transformation on the $\cos^2(x)$ function to make the slope definition appear:

$$\cos^2(\theta) = \frac{1}{1+\tan^2(\theta)} = \frac{1}{1+\left(\frac{dy_{cs}}{dx}\right)^2}$$

The obtained system is termed **"model 1"** for using the slope approximation only once:

$$\begin{cases} \dfrac{dz_0}{dx} &= z_1 \\ \dfrac{dz_1}{dx} &= -\dfrac{z_0 - z_2 + R}{z_0 - z_2}\dfrac{K_e^2}{2\pi(z_0 - z_2)}\dfrac{1}{\cos^2(\theta_{0,1})}\sqrt{\dfrac{\dot{G}_{0,2}}{\dot{G}_{0,1}}}\dfrac{1}{1+z_1^2} \\ \dfrac{dz_2}{dx} &= z_3 \\ \dfrac{dz_3}{dx} &= +\dfrac{z_0 - z_2 + R}{z_0 - z_2}\dfrac{K_e^2}{2\pi(z_0 - z_2)}\dfrac{1}{\cos^2(\theta_{0,2})}\sqrt{\dfrac{\dot{G}_{0,1}}{\dot{G}_{0,2}}}\dfrac{1}{1+z_1^3} \end{cases} \tag{C.5}$$

During this derivation process, it appeared that it was also possible to get rid of the first use of the slope approximation modifying slightly the reasoning of Faghani and Rogak. The system derived is termed **"model 0"** following the same idea as previously. Its structure is different than models 1 and 2: the modified reasoning led to a system of two 1st order ODEs governing the evolution of θ_1 and θ_2 involving 3 unknowns $(\theta_1\,;\,\theta_2\,;\,y_s)$. A third differential equation related to the local distance between the trajectories is added to the system using the very definition of y_s and the slope definition:

$$\frac{dy_s}{dx} = \frac{dy_{cs,1}}{dx} - \frac{dy_{cs,2}}{dx} = \tan(\theta_1) - \tan(\theta_2) \tag{C.6}$$

The final system is only composed of 1st order ODEs and no further mathematical transformation is needed. Using the notations $Z = (z_0, z_1, z_2) = (\theta_1\,;\,\theta_2\,;\,y_s)$, model 0 can be written:

$$\begin{cases} \dfrac{dz_0}{dx} &= -\dfrac{z_2 + R}{z_2}\dfrac{K_e^2}{2\pi z_2}\dfrac{\cos^2(z_0)}{\cos^2(\theta_{0,1})}\sqrt{\dfrac{\dot{G}_{0,2}}{\dot{G}_{0,1}}} \\ \dfrac{dz_1}{dx} &= +\dfrac{z_2 + R}{z_2}\dfrac{K_e^2}{2\pi z_2}\dfrac{\cos^2(z_1)}{\cos^2(\theta_{0,2})}\sqrt{\dfrac{\dot{G}_{0,1}}{\dot{G}_{0,2}}} \\ \dfrac{dz_2}{dx} &= \tan(z_0) - \tan(z_1) \end{cases} \tag{C.7}$$

C.1.2. Discussion on the initial conditions

Integrating a system of ODEs requires an associated set of initial conditions. For model 0 there is no discussion possible and the set of initial conditions is:

$$Z_0 = (\theta_{0,1}\,;\,\theta_{0,2}\,;\,S)$$

On the contrary, two sets of initial conditions can potentially be used for each model 1 or 2 whether the slope approximation is used again or not:

"tan": $Z_0 = \left(\frac{S}{2},\ \tan(\theta_{0,1}),\ -\frac{S}{2},\ \tan(\theta_{0,2})\right)$

and

"approx": $Z_0 = \left(\frac{S}{2},\ \theta_{0,1},\ -\frac{S}{2},\ \theta_{0,2}\right)$

C.1.3. Conclusion

Combining the models with the possible sets of initial conditions, it makes in total 5 integration modes to investigate:

- model 0 ;
- model 1 – approx ;
- model 1 – tan ;
- model 2 – approx ;
- model 2 – tan ;

Each one is implemented and their performances are compared against the trajectory predictions and experimental data reported by Faghani and Rogak, and against the trajectory predictions and convergence point predictions from the SJ/WJ model of Grandmaison et al. [64]

The criterion used by Faghani and Rogak to predict the convergence point (end of trajectories) is when the distance between the two centerlines is equal to 2 times the jet radius. It is different from the one used by Grandmaison et al. stating that the the convergence point axial position is the axial position at which the bending centerline hits the external jet envelope of the strong jet.

The ratio of initial momentum rate between the two jets is characterized by:

$$\psi = \frac{\dot{G}_{0,1}}{\dot{G}_{0,2}}$$

In a SJ/WJ configuration, $\psi \ll 1$.

C.2. Comparison with 10° diverging injection angle trajectories

The first set of comparison between all integration modes is performed against some experimental measurements and the trajectory predictions of the Bending Model for a 10° diverging injection angle reported by Faghani and Rogak (figure C.2). All integration modes perform well compared to the Bending Model of Faghani and Rogak: they all predict slightly more curved trajectories, regardless of the momentum rate ratio, but they stay in good agreement with both experimental points and the reported predictions. Additionally, no significant difference can be noticed between the different modes predictions. It is probable that the local angles induced by the initial injection angle are too small to question the validity of the slope approximation. In fact the error introduced by the slope approximation is plotted in figure C.1 for angles ranging from $0°$ up to $40°$. For instance for local angles up to $10°$, the slope approximation is verified with 99% confidence.

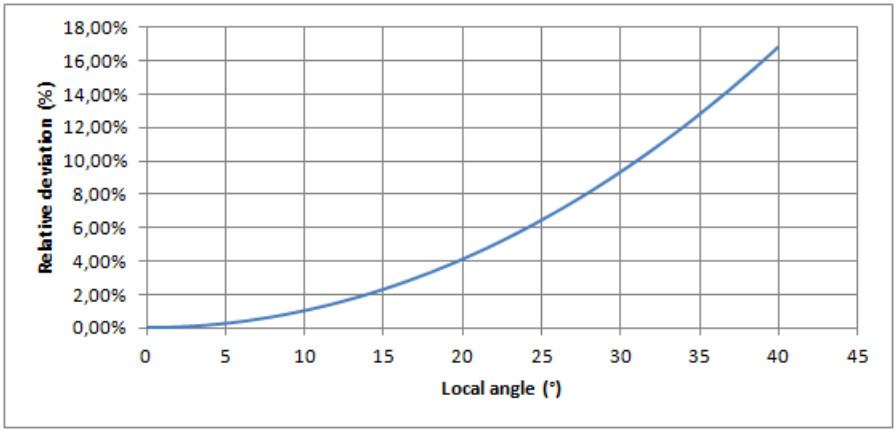

Figure C.1: Relative error introduced with the slope approximation

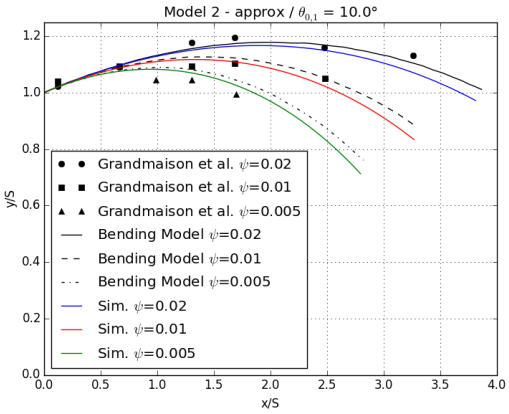

(a) model 2 – approx

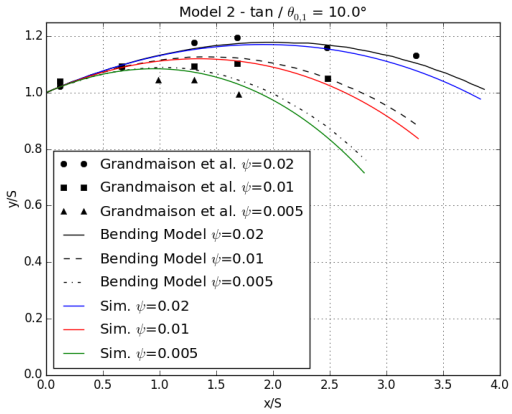

(b) model 2 – tan

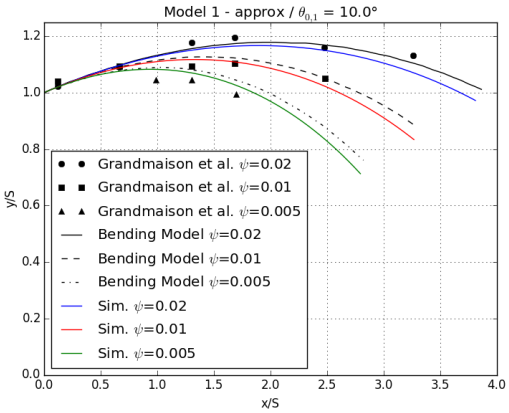

(c) model 1 – approx

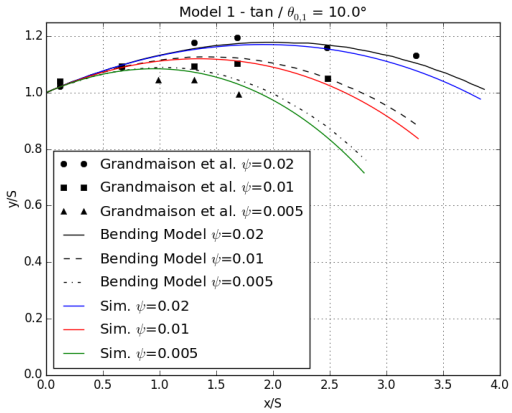

(d) model 1 – tan

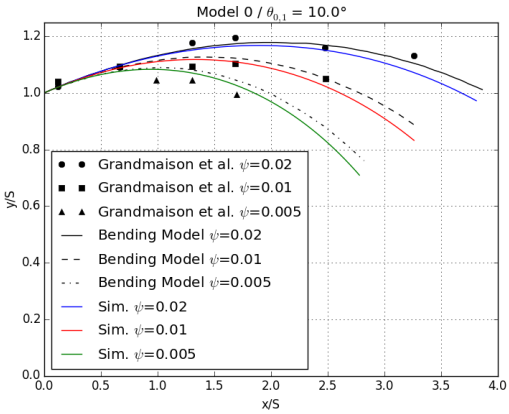

(e) model 0

Figure C.2: Comparison of trajectory predictions for all integration modes at 10° diverging injection angle

C.3. Comparison with 20° diverging injection angle trajectories

The injection angle is now increased to 20°. The results are displayed in figure C.3. The trajectory predictions stay in good agreement with the Bending Model predictions, except for models 0, 1 – approx and 2 – approx at $\psi = 0.05$. This momentum rate ratio corresponds to the most curved trajectory where the slope approximation starts to introduce significant error. All integration modes are however in good agreement with the experimental results. Furthermore, there are now noticeable deviations between the predictions from all integration modes despite the overall quality of all modes predictions.

These two sets of comparisons do not allow to conclude as to a preferred integration mode.

C.4. Trajectory prediction comparison with the SJ/WJ model

Additional simulations are carried out in order to compare the trajectory predictions of each integration mode with the predictions from what is considered a benchmark model: the SJ/WJ model. For a consistent comparison, both the jet spreading constant and the convergence criterion of the original Bending Model are modified. Dimensionless coordinates are also defined:

$$\xi = \frac{x}{S} \text{ and } \eta = \frac{y}{S}$$

The trajectory predictions were performed for $\psi = 0.02$.

The predictions from all integration modes are plotted against the SJ/WJ predictions in figure C.4. The black lines are the SJ/WJ predictions, the color lines the Bending Model predictions. Each mode consistently predicts more curved trajectories than the SJ/WJ model for injection angles from 0° to 20° diverging. If this case is any indication of a trend, the convergence point streamwise position would likely be underpredicted for theses angles at different ψ. Once again, at larger angles, significant deviations between integration modes and with the SJ/WJ predictions can be noticed. Models 1–approx and 2–approx show the most important discrepancies at large angles.

C.5. Convergence point prediction comparison with the SJ/WJ model

Because the ultimate goal of using such a predictive model is to predict the jets convergence point in a SJ/WJ configuration, the convergence point behavior of the different implementations of the Bending Model are compared with the SJ/WJ behavior. It may bring sufficient information to eventually select a preferred integration mode. Figure C.5 gathers all results. ξ_c is the dimensionless axial position of convergence.

For the window investigated ($\psi = 0.004 - 0.1$ and weak jet injection angle 0° – 40° diverging), all integration modes convergence point predictions are very close to the SJ/WJ predictions at small angles (0° and 10°). Insignificant deviations are displayed. For all modes at 20°, the deviation from the SJ/WJ prediction is small at small ψ, but is rapidly growing with an increasing injection momentum ratio. At 30° and 40°, the behavior of models 0, 1–approx and 2–approx is not satisfactory if the SJ/WJ model were to be taken as reference. To the contrary, models 1–tan and 2–tan perform better.

C.6. Conclusion: selection of the preferred integration mode

From the preceding results, model 1–tan is selected as preferred integration mode: it performs very well for both trajectory prediction and convergence point prediction against experimental data and the SJ/WJ model predictions. Model 2–tan also has a good behavior, but knowingly introducing further approximation into a model does not feel right. The behavior at high diverging injection angles is the determining argument, but the Bending Model still needs to be used with caution in this range.

This analysis does not constitute a validation of using the Bending Model as predictive model in the reactor network. In view of these results it is certainly expected that it could be integrated with success though. The final validation is done at the end of section 4.3, on the 3 jets configuration of the Bending Model, implemented according to the guidelines of model 1–tan.

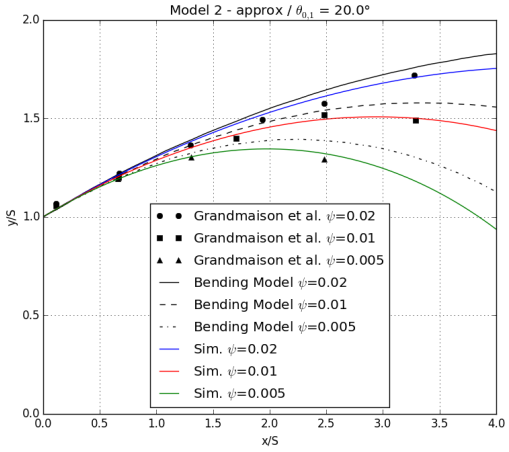

(a) model 2 – approx

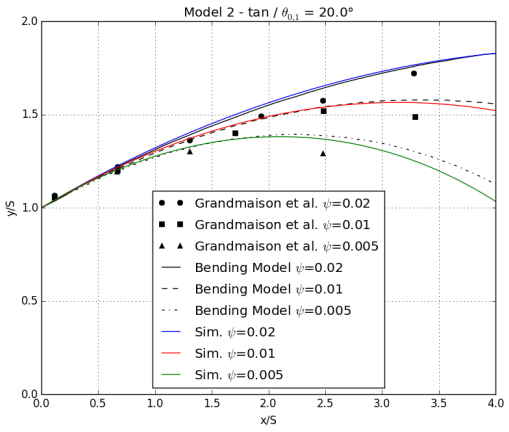

(b) model 2 – tan

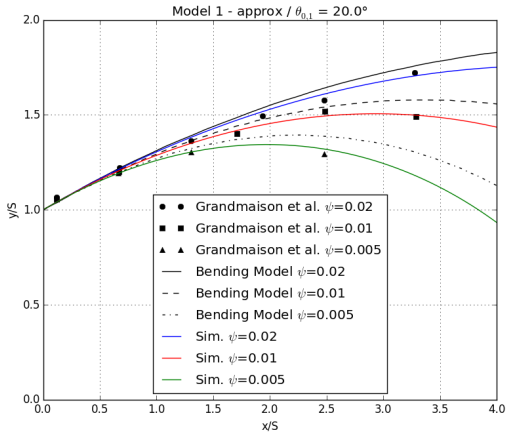

(c) model 1 – approx

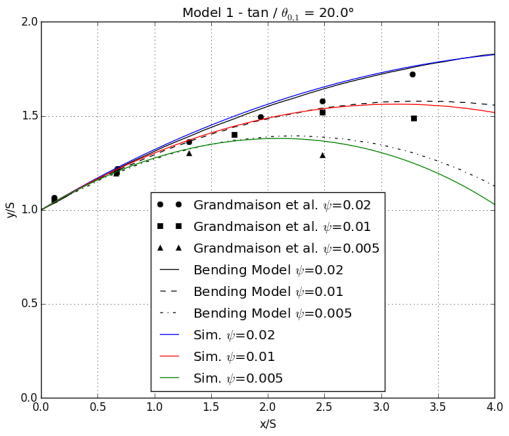

(d) model 1 – tan

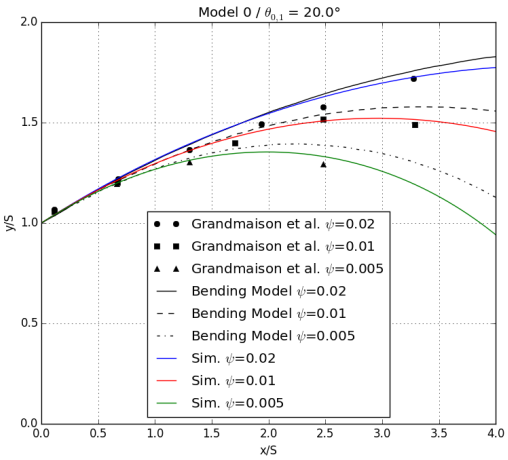

(e) model 0

Figure C.3: Comparison of trajectory predictions for all integration modes at 20° diverging injection angle

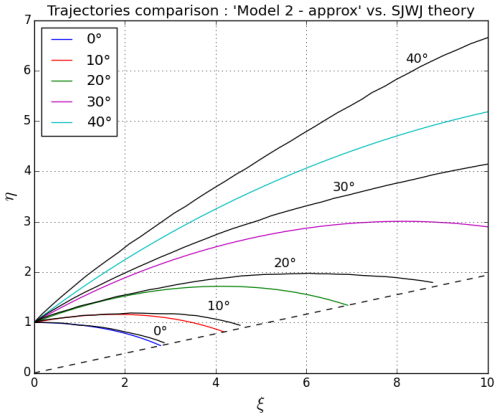

(a) model 2 – approx

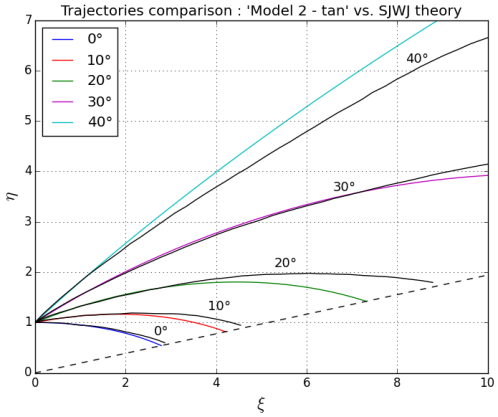

(b) model 2 – tan

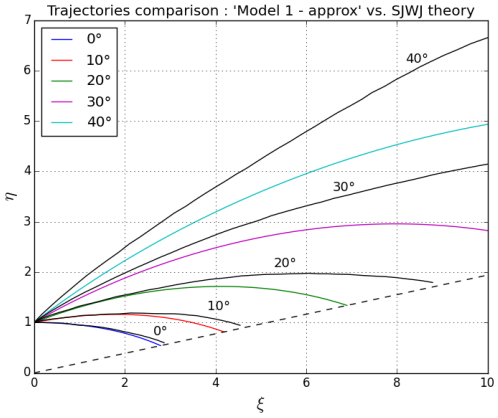

(c) model 1 – approx

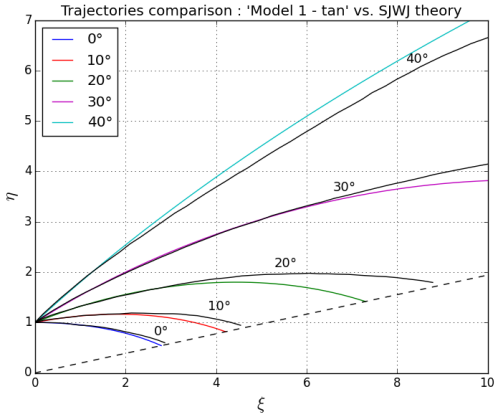

(d) model 1 – tan

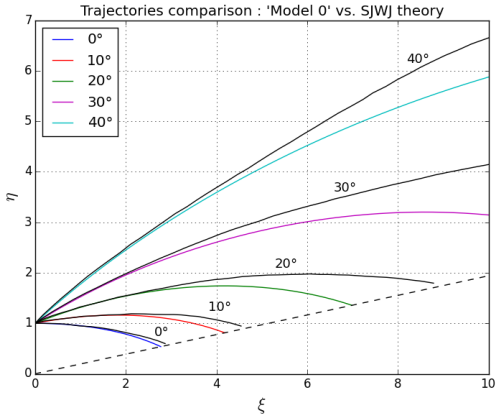

(e) model 0

Figure C.4: Comparison of trajectory predictions with the SJ/WJ model

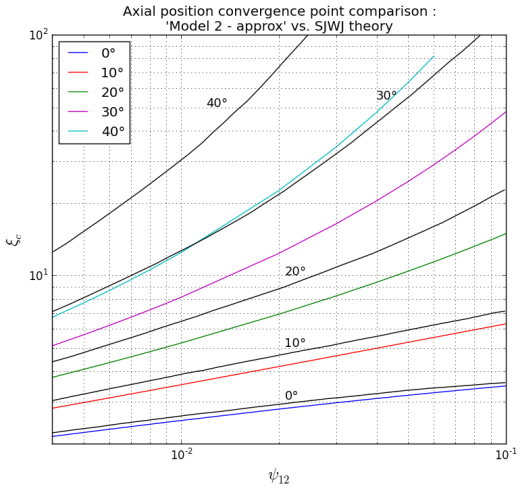

(a) model 2 – approx

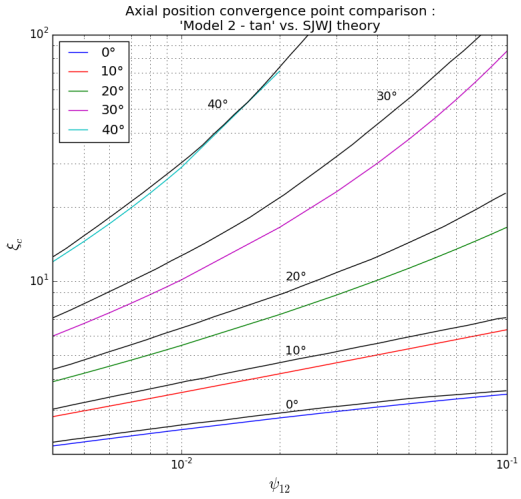

(b) model 2 – tan

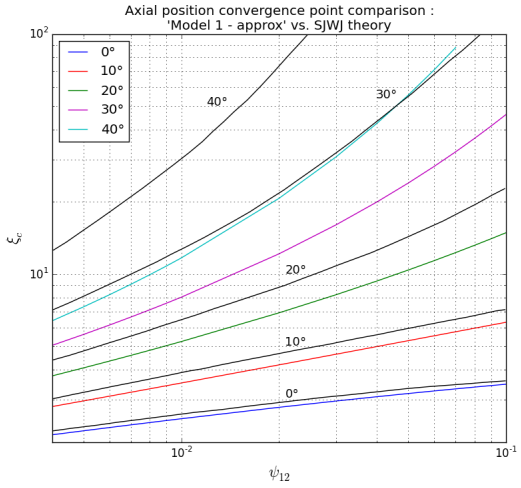

(c) model 1 – approx

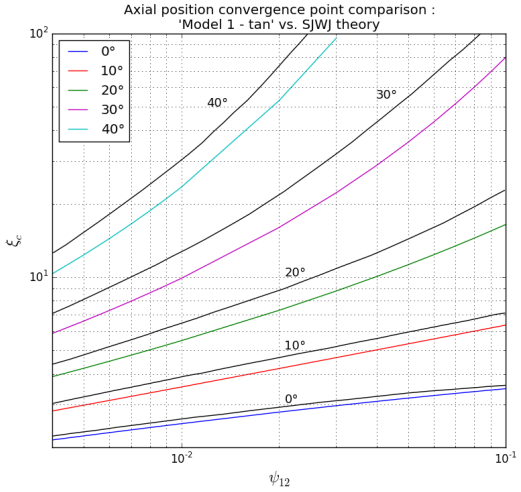

(d) model 1 – tan

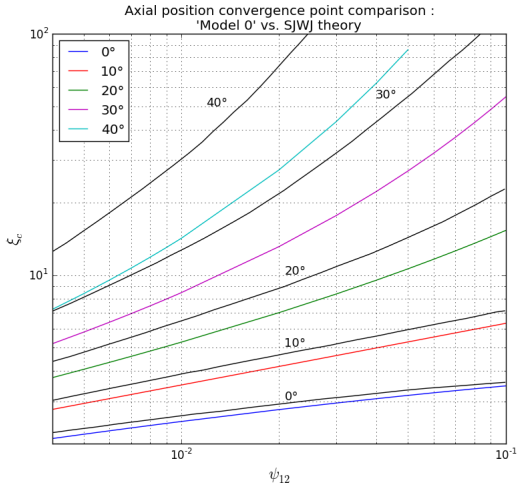

(e) model 0

Figure C.5: Comparison of convergence point predictions with the SJ/WJ model

D

Shielded Entrainment Model development

A comparison between experimentally determined jet entrainment data and the prediction from the Ricou & Spalding model highlighted a mutual shielding between the jets in a SJ/WJ configuration. In order to model this phenomenon, jet structure data obtained with the Bending Model is used to build a shielding factor. This factor would then be combined with the Ricou & Spalding model to create a customized entrainment model, adapted to SJ/WJ configurations. Two different geometrical arguments have been considered to define the shielding factor and are presented in this appendix.

D.1. Shielding factor: method A

The first geometrical argument consists in considering that shielding occurs only as soon as the jets envelopes start to intersect. As the SJ attracts the WJ, both of them expand, and inevitably their respective envelopes intersect at some point. Both jets cross sections are considered to be circular and the jet entrainment is assumed to be uniform around this circumference. The angular section of each jet that is shielded is determined according to figure D.1. Finally the SJ and WJ shielding factors SF_i are defined by:

$$SF_i^A = 1 - \frac{\beta_{shielded,i}^A}{2\pi} \tag{D.1}$$

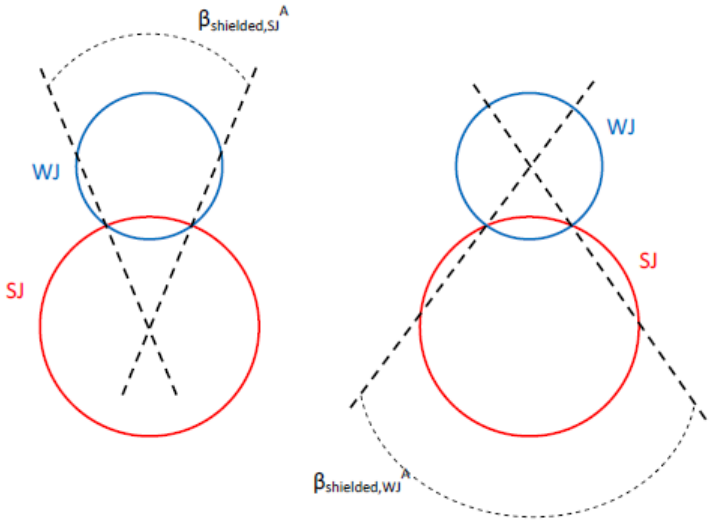

Figure D.1: Determination of the shielded angular portion of the SJ (left) and the WJ (right) with method A

The jet structure data calculated in the Bending Model allows to obtain the streamwise evolution of the shielding factors. The result of their application on the Ricou & Spalding jet entrainment model is displayed in figure D.2. As expected the shielding starts only at a given location downstream which introduces a big discontinuity in the entrainment law. For the SJ, this criterion yields a good prediction for the intersecting region. For the WJ, the corrected entrainment is still within the reported experimental error but the accuracy is not as good as for the SJ. In the region where jets don't intersect, the original Ricou & Spalding law gives a reasonable estimation for both jets.

All in all, this method gives acceptable predictions if the regions were taken separately. But the discontinuity introduced by the sudden start of the mutual shielding is a feature that needs to be improved: a new criterion is needed

D.2. Shielding factor: method B

Method B has been designed to provide a continuous shielding all along the jets length to overcome the discontinuity problem. The entrainment field of each jet is now assumed to be impacted by the presence of the other jet as soon as they are ejected. The shielded angular portion of each jet is defined according to figure D.3: the arc between the green crosses is considered to be shielded. Similarly to method A, the shielding factors are defined by:

$$SF_i^B = 1 - \frac{\beta^B_{shielded,i}}{2\pi} \tag{D.2}$$

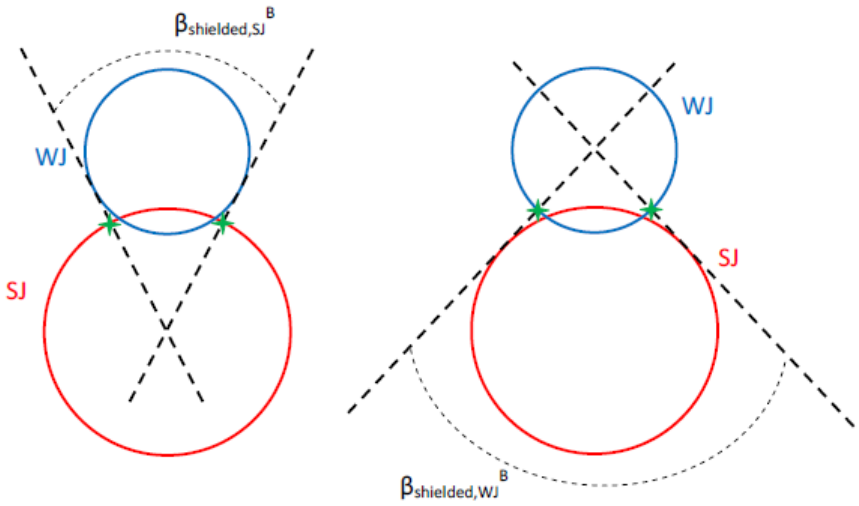

Figure D.3: Determination of the shielded angular portion of the SJ (left) and the WJ (right) with method B

Figure D.4 shows the results of the application of method B. No discontinuity appears in this customized entrainment law: method B yields a smooth and continuous correction, except:

- for the SJ, in the region 70-80 cm where the shielding suddenly spikes and the entrainment starts to drop.
- for the WJ, the same phenomenon appears but sooner, around 50-60 cm. Furthermore, although the entrainment was computed up to 75 cm downstream, the shielding is not defined in the last part of the jet, from 60 cm on, preventing to compute the entrainment. This is due to the mathematical method adopted, which uses the arc sinus function. This function is defined on a specific interval, and the geometry of the jets causes the function to be applied on values outside its definition interval before 75 cm downstream.

The shielded entrainment predicted for the SJ is of very good quality in the first part of the jet while for the WJ, it tends to increasingly underestimate the entrainment. The last region of the simulated jets is clearly badly predicted with method B, which in addition to the mathematical limit encountered in the WJ, prevents to use it on its own to define the final shielding factor.

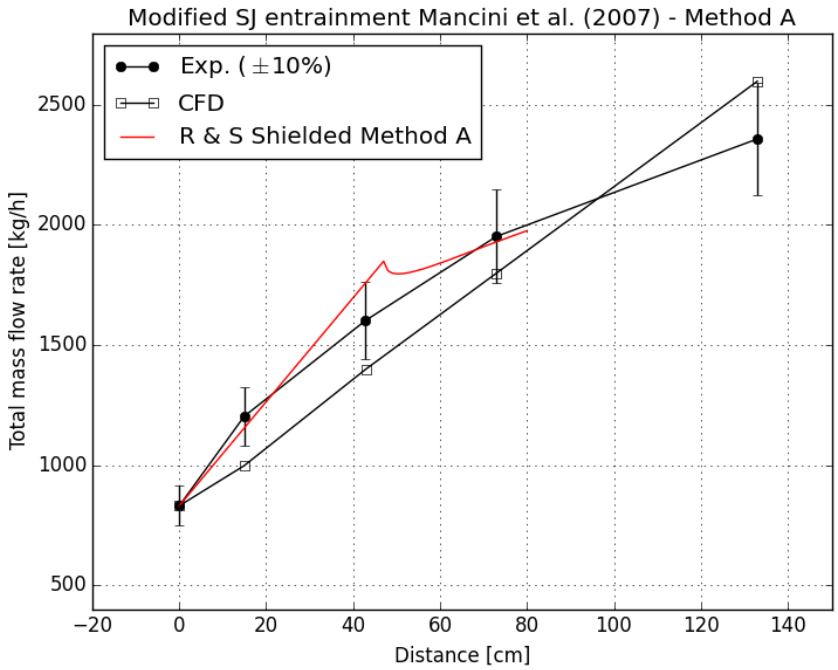

(a) SJ entrainment evolution

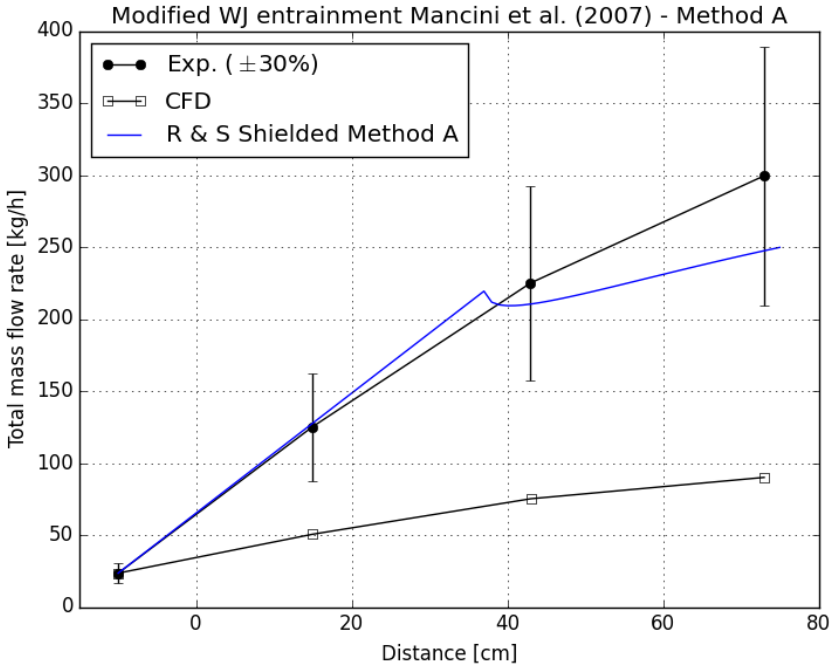

(b) WJ entrainment evolution

Figure D.2: Application of method A and comparison with entrainment data (adapted from [62])

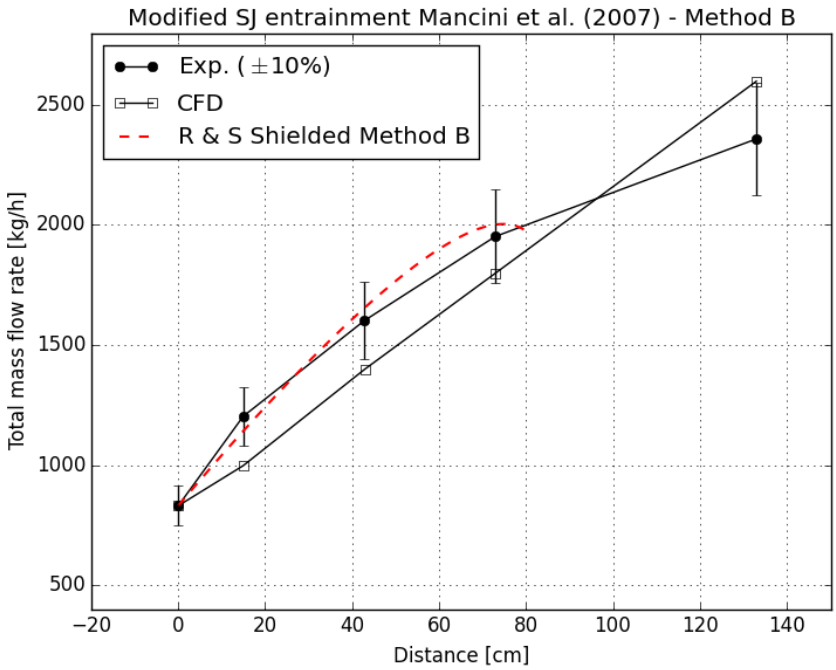

(a) SJ entrainment evolution

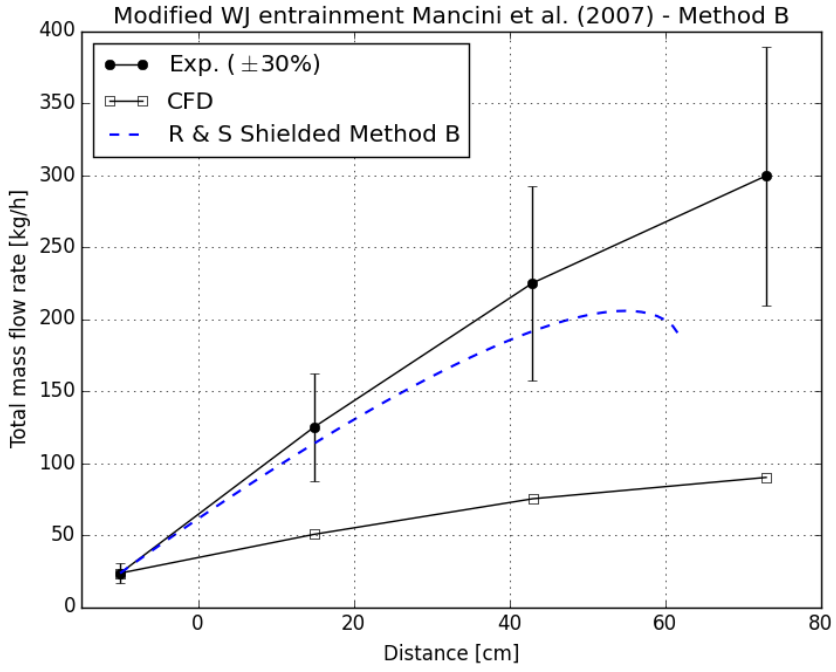

(b) WJ entrainment evolution

Figure D.4: Application of method B and comparison with entrainment data (adapted from [62])

D.3. Adoption of a combined criteria

The results obtained with either method or not satisfying on their own along the whole length of the jets. They are however yielding good predictions in different regions of the jet and combining them may result in a smooth and accurate enough entrainment prediction. The study of the combined criteria is tackled in section 4.4, and eventually leads to its adoption for the SJ, while no shielding will be applied on the WJ in the simulations.

D.4. One weakness of the Shielded Entrainment Model

During preliminary simulations on the IFRF furnace setup, one weakness of the adopted shielding criteria for the SJ is highlighted for a certain combination of the parameters $x\%$ and n_{PSR}. At a given mixer length fraction ($x\% = 10\ \%$), the number of PSRs discretizing the jets is gradually reduced from 10 to 5 to 3 (figure D.5): in the last case, the mass flow supposed to exit the mixer is smaller than the mass flow supposed to enter. This non–physical behavior does not trigger an error in Cantera because of the way the mass flow controllers are defined. This phenomenon must be a consequence of the mixer entrainment determination process.

To go around this problem a conditional loop was implemented in the model that prevents it to be simulated if the mixer ”leak” is present. The user then needs to tune the constants $x\%$ and n_{PSR} to obtain a proper combination. A more physically appropriate solution would be to improve the calculation of the mixing region entrainment in the Shielded Entrainment Model (see appendix E):

- the definition of the mixing region extent and volume can be developed further.
- a more accurate process to define the entrainment of the mixing region can be imagined, for instance the asymptotic entrainment coefficient for reacting flows proposed by Han & Mungal (subsection 2.4.2) could be tested.

Improving the Shielded Entrainment Model would benefit both the stability of the program, but also its accuracy: it impacts the temperature level in the mixing region and hence the pollutant production.

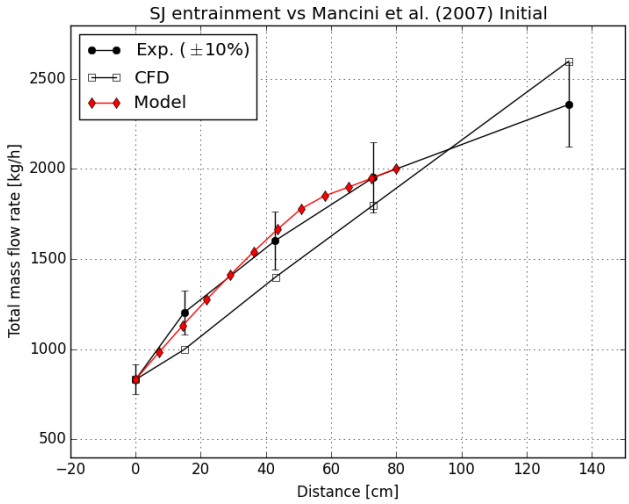

(a) $x\% = 10\ \%$ / $n_{PSR} = 10$

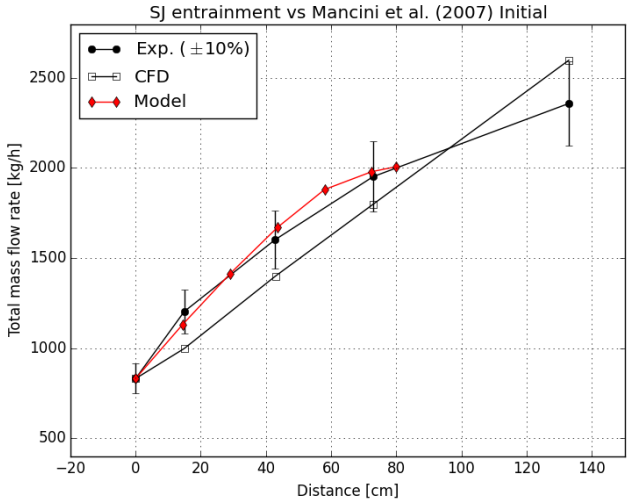

(b) $x\% = 10\ \%$ / $n_{PSR} = 5$

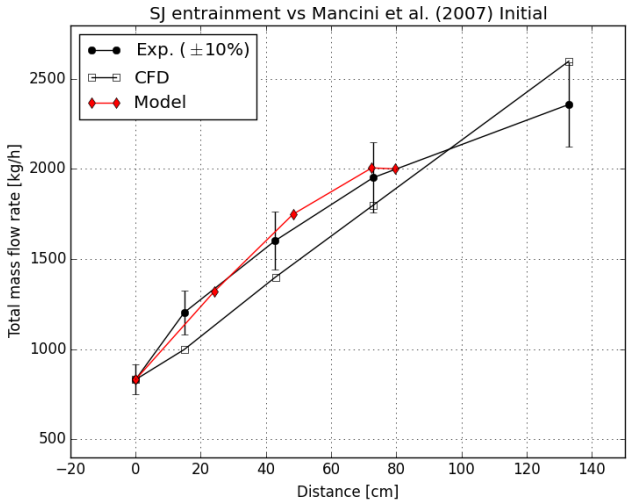

(c) $x\% = 10\ \%$ / $n_{PSR} = 3$

Figure D.5: Illustration of the mixer ”leak” phenomenon, a weakness of the Shielded Entrainment Model

E

Details on the development of Mancini's reactor network and additional simulations

Additional details as to the development of the reference reactor network used to design the analytical emission estimator for flameless furnaces could only be obtained after the modeling work was done. They are reported in the PhD dissertation of Mancini [72].

E.1. Differences with the designed analytical estimator

In addition to use experimental measurements or CFD simulations to obtain the amount of gases re-circulated along the jet and mixing regions, three different design choices are reported by Mancini:

1. A radiation source/sink term is implemented into each reactor, calibrated using the CFD results. This particularity has already been mentioned in subsection 4.6.3.

2. The reactors volumes are calculated iteratively along the simulation using:

$$V = \int_{x_1}^{x_2} \pi R(\xi)^2 d\xi \tag{E.1}$$

   with the radius law derived from the continuity equation:

$$R(x) = \frac{D_0 \rho_0}{2} \sqrt{\frac{1}{1.26 \rho_\infty \rho(x)}} (ax + 1) \tag{E.2}$$

   where D_0 is the nozzle diameter, ρ_0 the gas density at injection, ρ_∞ the density of the surrounding entrained gas and a the slope of the entrainment function. This definition accounts for the amount of entrained gas in the jet expansion. It is expected to yield smaller volumes than the geometrical method used by the Bending Model.

3. Finally a similar criterion to define the extent and volume of the mixing region is reported: it is assumed to be a volume element of the strong central jet developing further, over a distance also defined as a fraction of the merging/convergence length. However, Mancini used the results of Yimer et al. [65] to obtain a very different order of magnitude of the mixing region extent. The extent of the region is assumed to be equal to the convergence length, which translated to the notations of this work means $x\% = 100.0\%$. The volume of this region is also calculated using the above formulas.

E.2. Additional simulations: impact of the mixer entrainment definition

In view of these precisions, it becomes clear that the mixer length parameter influence was not investigated in a large enough window. Additional simulations are then performed on the IFRF furnace operating point, using $n_{PSR} = 3$ but with $x\% = 20.0\ \%$, $x\% = 100.0\ \%$ and $x\% = 200.0\ \%$, and keeping the geometrical volume definition from the Bending Model. The results are gathered in table E.1. $C_{e,SJ}^{mixer}$ and $C_{e,WJ}^{mixer}$ are respectively the slope of the entrainment functions used to obtain the SJ and WJ contributions to the mixer entrainment.

ADDITIONAL SIMULATIONS RESULTS						
$x\%$	$T_{peak}\ [K]$	$NO\ exit\ [ppmvd]$	$CO\ exit\ [ppmvd]$	$C_{e,SJ}^{mixer}$	$C_{e,WJ}^{mixer}$	$C_p^{mixer}\ [J/kg/K]$
20	1879	169	24	0.107	0.32	1599.5
100	1803	142	16	0.127	0.32	1588.4
200	1732	123	14	0.137	0.32	1577
NETWORK PREDICTION [62]						
100	1840	135	13	0.101	0	xxx
MEASUREMENTS [42]						
xxx	1808	140	0	xxx	xxx	xxx

Table E.1: Results from additional simulations of the IFRF furnace

Several features are worth noticing:

- When $x\%$ is varied to this extent, the SJ entrainment intensity calculated by the Shielded Entrainment Model increases.
- It impacts the energy balance in the mixer: the same amount of heat is released over more mass, while the mixture calorific capacity shows a mild decrease due to the temperature dependence. All in all it causes a decrease of the mixer temperature by $70 - 80\ K$ between each case, and a consequent decrease in NO at the furnace exhaust of $30 ppmvd$ and $20 ppmvd$.
- It is striking to notice that the measurements peak temperature and exhaust NO concentration are reproduced using the analytical network with $x\% = 100\ \%$. When comparing this case to Mancini's network, it can be seen that the additional mass flow introduced in the mixer by the analytical entrainment model compensates the potential radiation losses occuring in the mixer which are not accounted for.
- Finally, the calculated value of the SJ entrainment slope in this case is very close to 0.13, the asymptotic value of the entrainment coefficient proposed by Han & Mungal for a reacting jet without coflow (subsection 2.4.2).

This offers a potential development of the Shielded Entrainment Model, improving the method to obtain the mixing region entrainment. Instead of adding the contributions of the SJ and the WJ calculated over the mixer length, this asymptotic entrainment coefficient could be used for the mixer reactor, considered an extension of the central strong jet evolution. It is physically more accurate since the WJ does not exist anymore after complete merging with the central SJ. Further investigation would be needed to validate this modification. In parallel, one may also consider to use Mancini's equations to define the mixer volume as well.

As an illustration, the SJ mass flow evolution up to the mixer outlet is plotted for the parameters $x\% = 100\ \%$ and $n_{PSR} = 3$ in figure E.1. One can see that the mixer entrainment is overpredicted, but within experimental measurement error. Using a slope of 0.13 instead of the calculated 0.127 would yield a slightly higher entrainment, but still coherent with the measured entrainment.

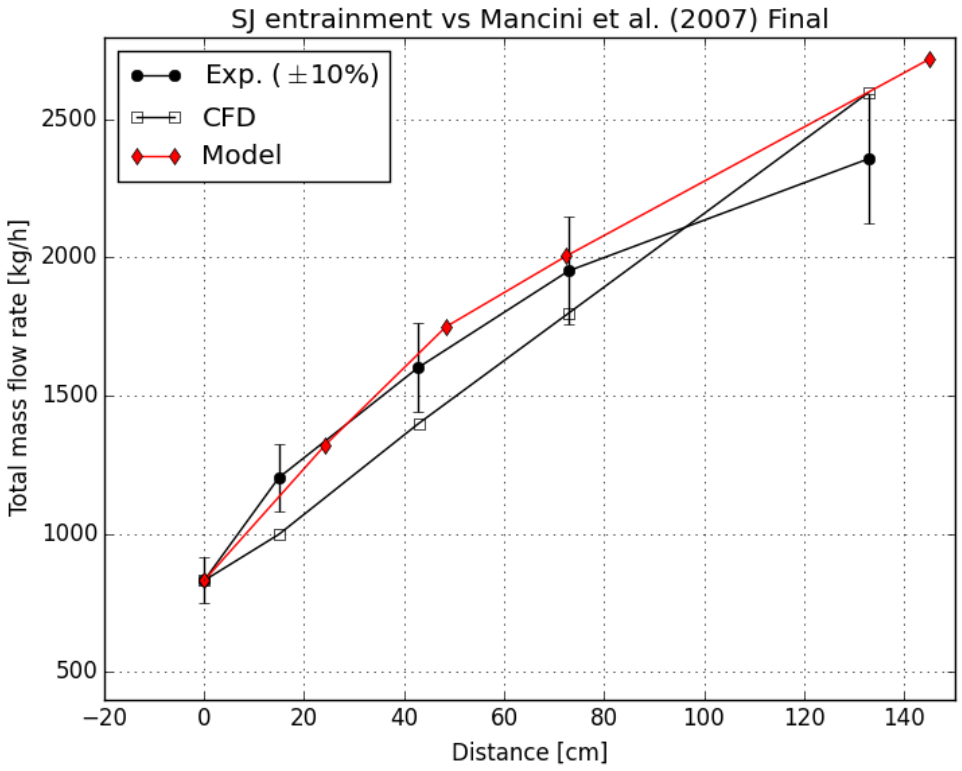

Figure E.1: Evolution of the SJ mass flow for $x\% = 100\ \%$ and $n_{PSR} = 3$

E.3. Sensitivity analysis results

Mancini also performed a sensitivity analysis on several variables of his network [72]: the number of reactors discretizing the jets (n_{PSR}), the radial discretization of the jets (3 reactors instead of 1), the number of reactors discretizing the mixing region (15 instead of 1, 3 radially and 5 in the streamwise direction) and finally the volume of the mixing region ($x\%$).

1. Varying n_{PSR} from 5 to 10 to 20 results in negligible deviations in NO at the exhaust. This is in line with the investigation conducted in this work.
2. With $n_{PSR} = 10$, discretizing radially with 3 reactors (so a total of 30 reactors per jet) also causes negligible differences.
3. The mixing region subdivision results in only marginal differences.
4. Finally the mixer volume is varied accordingly to the values $x\% = 50,\ 100,\ 200\ \%$. Small differences of the order of $1ppm$ were predicted.

The sensitivity of the analytical network, fitted with the mixer entrainment and volume corrections, could be analyzed and compared to this last result.

E.4. Conclusion

The specific design criteria reported by Mancini may allow to improve the stability and accuracy of the analytical reactor network, mainly by improving the mixer reactor characteristics, which was identified as key to the network predictions.

F

Alternative heat loss implementation in the cryogenic combustor network

In chapter 5 a reactor network modeling a lean–premixed combustor experimental installation is designed. Measurements showed that a substantial amount of heat is lost to the surroundings during operation. The general architecture implemented is composed of:

- A PSR cluster of 3 interconnected PSRs representing three distinct regions of the flow pattern visualized in experiments: first a non–reacting region just after the mixing tube exit, followed by an ignition/flame region for the lean mixture and a recirculation region modeling the central/inner recirculation of the flow pattern which is the key feature for flame stabilization in this combustor.
- A plug–flow region modeled using a PFR, starting after the flame and recirculation regions. The combustor flow is averaged and considered uniform in a cross section of the combustor.
- Heat losses to the environment from the hot regions of the flow. In the presented architecture, heat loss was implemented using a constant heat flux through the flame reactor and PFR walls. It is reasonable to consider that applying heat loss on the flame reactor or on the recirculation reactor is equivalent given the network architecture. This assumption is verified in this appendix.

The architecture considered is depicted in figure F.1. It is similar in all respects to the architecture optimized in chapter 5 except for the region losing heat in the PSR cluster.

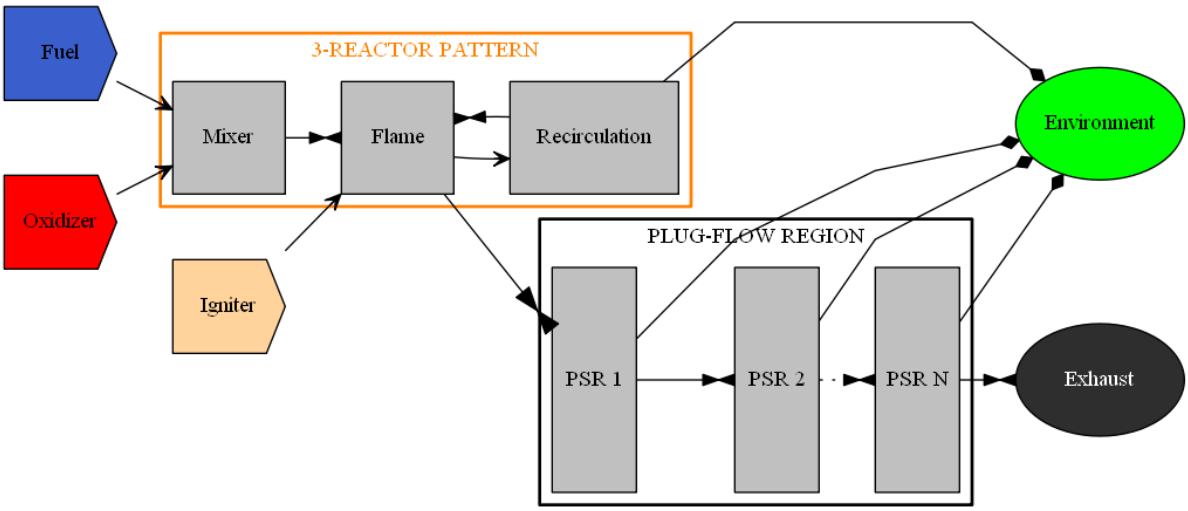

Figure F.1: Basic architecture modeling the cryo combustor of the AHEAD engine with modified heat loss implementation

In order to make a consistent comparison with the original heat loss implementation, the heat lost by the recirculation reactor should be equal to the amount of heat lost by the flame reactor in the same conditions. This way the influence of the location of heat loss can be analyzed. Only the critical ϕ cases for each air preheat temperature setting are simulated, for an inlet air mass flow of $\dot{m}_{air} = 130\ kg/s$. The results are compared with the predictions from the original network architecture (heat loss along flame and PFR reactors) in table F.1: it is completely equivalent in terms of emissions for the heat to be lost in the flame reactor or in the recirculation reactor, for the parameters window investigated. Since the flame reactor is the one physically along the combustor wall losing heat to the surroundings, the development is carried out on the original network architecture.

INFLUENCE OF HEAT LOSS LOCATION			
		Flame	**Recirculation**
$T_{air,preheat}\ [K]$	ϕ	$NO_x\ [ppmv@15\%O_2, dry]$	$NO_x\ [ppmv@15\%O_2, dry]$
313	0.8	23.73	22.95
453	0.8	43.58	41.36
623	0.7	43.60	40.77
703	0.6	25.81	24.28

Table F.1: Investigation of the influence of heat loss location

If a closer look is given to these results, it appears that for the cases in which the thermal pathway intensity starts to be dominant in the flame and recirculation reactors ($453K - 0.8$, $623K - 0.7$), applying heat loss to the recirculation reactor lowers the predictions, and it is likely that at higher equivalence ratio and/or lower inlet air mass flow the gap would increase further. This phenomenon is due to a further reduction of the recirculation reactor temperature, by twice the amount it would be if the heat loss was applied on the flame reactor (from $80K$ to $167K$ for both cases). The flame reactor temperature keeps a constant value in the meantime. This difference is significant enough when the thermal pathway dominates to induce noticeable NO_x production changes. Indeed the NO_x production in the recirculation reactor is approximately reduced by $50\,\%$ in both cases. The decrease of NO_x emission at the exhaust is only due to this reduction of NO_x creation in the recirculation reactor: the PFR production stays constant ($+22\ ppmvw$ and $+16\ ppmvw$ respectively). The reactors characteristics for both cases are gathered in tables F.2 and F.3:

- AD. : heat loss is applied only along the PFR (adiabatic PSR cluster) ;
- FL. : heat loss is applied along the flame and PFR reactors ;
- REC. : heat loss is applied along the recirculation and PFR reactors.

In the parameters window investigated during the experiments, the induced decrease in NO_x exhaust concentration is insignificant when simulating the operating conditions with the reactor network. The heat loss can then equivalently be implemented on the flame or on the recirculation reactor.

$T_{air,preheat} = 453\,K$ / $\phi = 0.8$ / $\zeta = 35\,\%$					
Heat loss mode	$T_{fl}\,[K]$	$T_{rec}\,[K]$	$NO_x^{fl}\,[ppmvw]$	$NO_x^{rec}\,[ppmvw]$	$NO_x^{exhaust}\,[ppmvw]$
AD.	2140	2219	xxx	xxx	xxx
FL.	2062	2139	61.08	70.04	82.68
REC.	2062	2052	56.90	61.72	78.45

Table F.2: Reactors characteristics under different heat loss modes for $T_{air,preheat} = 453\,K$, $\phi = 0.8$, $\zeta = 35\,\%$

$T_{air,preheat} = 623\,K$ / $\phi = 0.7$ / $\zeta = 35\,\%$					
Heat loss mode	$T_{fl}\,[K]$	$T_{rec}\,[K]$	$NO_x^{fl}\,[ppmvw]$	$NO_x^{rec}\,[ppmvw]$	$NO_x^{exhaust}\,[ppmvw]$
AD.	2112	2189	xxx	xxx	xxx
FL.	2034	2108	57.50	67.16	73.69
REC.	2034	2022	52.75	57.75	68.92

Table F.3: Reactors characteristics under different heat loss modes for $T_{air,preheat} = 623\,K$, $\phi = 0.7$, $\zeta = 35\,\%$

G

User guide: flameless furnace emissions estimator

The emissions estimator designed for flameless furnaces in chapter 4 is a stable and usable program. It is nonetheless a first version and can be improved. This appendix provides a description of the program structure and points out some peculiarities the potential user should look out for when using it. They are linked to potential developments that could improve the simulation of a new furnace, making it easier to adapt the model.

G.1. Program structure

The general structure of the program is a follows:

1. Definition of some functions called in the program.
2. Model inputs: burner geometry, inlet mass flows and temperatures, internal model constants.
3. Fuel and oxidizer compositions, definition of the initial mixer and furnace compositions.
4. Bending Model: jets trajectories and development, convergence point determination.
5. Set up of the reactor network (part 1):
    - Determination of the reactors volumes: SJ and WJ reactors, mixer, and furnace.
    - Creation of the reservoirs and the reactors, each with their dedicated gas object, and initialization of their volumes.
6. Shielded Entrainment Model: determination of the initial recirculation mass flows.
7. Set up of the reactor network (part 2):
    - Definition and initialization of the mass flow controllers and valves.
    - Implementation of the heat loss on the furnace reactor.
8. Iteration of the network:
    - Definition and initialization of the lists where the networks characteristics will be stored each iteration.
    - Iteration loops: iteration of the network over the time step dt_i, writing of the reactors characteristics in the lists, update of the recirculation mass flows, exit conditions.
    - Partial data deletion: only the last t_{data} seconds are kept.
9. Plot of the results.

G.2. Modeling a new flameless furnace installation

When using this program to predict the emissions of a furnace installation, the user should keep the following remarks in mind.

First the burner geometry of the furnace considered for modeling should be reduced as closely as possible to the geometry implemented: one central SJ and two symmetrically located WJ, keeping in mind that only half this configuration is modeled. For instance, for one central jet surrounded by four jets, symmetries of the system allow to consider only one of the four surrounding jets and the corresponding $^1/_4{}^{th}$ of the central jet. In this case, modifications of the program are necessary:

- the central jet entrainment should be divided by 4 instead of only by 2 ;
- the central jet volumes have to be similarly modified.

If the burner displays a central weak jet surrounded by multiple stronger jets, this program still works thanks to the adaptability of the Bending Model. However all the variables labeled SJ in the program represents in reality the central jet and will be used to describe the real central WJ. The furnace on which the design was based led to this choice of variable name, lacking generality.

Second, the chemical mechanism used in the design is the GRI 3.0 mechanism, chosen because natural gas is burned. If another fuel is used, another mechanism is likely to be used as well. In this case the calls related to species concentrations need to be modified: the calls are not automated to search for a certain species, but a position in the list of species, which should be expected to be different between two mechanisms.

The model internal parameters are related to the iteration loops or the physical characteristics of the model inherently constant (jet spreading, jet entrainment coefficient). Among this set of parameters, the value of the valve coefficient K_v should be set with caution according to the guideline provided in appendix A. Additionally, the pair of parameters (n_{PSR} ; $x\%$) needs to be adapted to keep the simulation time minimum but to prevent the mixer ”leak” (appendix D).

Finally the inputs related to the geometry of the furnace and the burner need to be modified, as well as the inlet mass flows, temperatures and compositions. For the latter, several manipulations are necessary in addition to manually specifying the compositions. The mixer composition needs to be manually updated: it is important for the initialization of both mixer and furnace reactors. Initializing the compositions as close as possible to what is expected after convergence is beneficial for the simulation time and prevents the furnace volume to change significantly along the simulation, keeping its value close to the real initial value. This last feature is an unnecessary complexity introduced by the pressure closure method adopted. It would be suppressed if the pressure closure is implemented using a constant volume PSR for the furnace reactor, linked to the exhaust reservoir using a valve. Furthermore the initial value of the jet structure plots is not automated and needs to be modified accordingly.

Following these guidelines will allow a potential user to simulate correctly the desired furnace, or to help him/her develop the program further.

H

User guide: gas turbine combustor emissions estimator

The emissions estimator designed and calibrated in chapter 5 allowed to investigate the main sensitivities of the AHEAD engine cryogenic combustor, and was able to predict quickly and accurately the NO_x emissions measured using an atmospheric experimental installation. Ultimately, the goal is to build a comprehensive model of the whole hybrid combustor, integrated in a gas turbine, to predict the level of emissions this revolutionary design would produce in operation. To this end, the current reactor network (modeling the experimental setup) was modified to emulate the operation of the cryogenic combustor under high pressures and coupled with a dilution/cooling stream. In order to make it easier to use the developed network as component of the comprehensive model, this appendix presents the general architecture of the program as well as the particularities to pay attention to for a proper use.

H.1. Program structure

The program structure is similar for both networks, either modeling the experimental installation or the integrated combustor into a gas turbine. The main program script works in synergy with a file gathering auxiliary functions the main program calls during execution ('flibrary', for functions library). These functions are used for various aspects: volumes determination, automatic selection of the valve coefficient value, emission concentration correction or tuning of the mass flows from the dilution stream entering the combustion stream along the PFR.

1. Model inputs: combustor geometry, inlet conditions, heat loss parameters, internal model constants.

2. Interface with the user to select the chemical mechanism to use.

3. Fuel, oxidizer and igniter compositions.

4. Creation of the reservoirs: fuel, oxidizer, igniter, exhaust and environment.

5. Set up of the reactor network (part 1): the PSR cluster. Determination of the volumes, creation and initialization of the reactors and their dedicated gas objects, creation and initialization of the mass flow controllers and valves, implementation of the heat loss flux on the flame reactor.

6. Iteration of the PSR cluster:

    - Definition and initialization of the lists where the reactors characteristics will be stored each iteration.
    - Iteration loop.
    - Creation of the plots related to the PSR cluster.

7. Set up of the reactor network (part 2): the PFR. Determination of unit PSR volume, creation and initialization of upstream and downstream reservoirs with their dedicated gas objects, creation and initialization of the unit PSR reactor (and the corresponding PSR of the dilution stream if present), creation and initialization of the flow controllers, implementation of the equally distributed heat loss flux along the PFR length.
8. Iteration of the PFR:
    - Definition and initialization of the lists where the PFR streamwise characteristics will be stored.
    - Iteration loop: each unit PSR (or coupled unit PSRs if a dilution stream is present) is simulated to steady state.
    - Creation of the plots related to the PFR region.
9. Plot of the results
10. NO_x pathway analysis (optional)

H.2. Guidelines for a proper use of the reactor networks

The combustor emissions estimator is a program more accomplished than the one designed for the flameless furnaces. For a potential user, only two points need to receive a particular attention.

The first one is the heat differential parameter Δ_{heat}. It is potentially variable between $0\,\%$ (constant heat flux along the PFR and flame reactor lateral areas) and $100\,\%$ (constant heat flux along the PFR lateral area only), but the implementation prevents from using the rounded $100\,\%$ setting because of a division by zero. Consequently, in order to simulate the network with heat loss only along the PFR length, the value $\Delta_{heat} = 99.99999\,\%$ should be used. Only an insignificant amount of heat will be lost in the flame reactor, while circumventing the mathematical problem.

The second point is the customization of the dilution stream injection, in the network modeling the integrated combustor. In this model the PFR is discretized with 100 PSRs, and two additional inputs are available: the portion of dilution stream (equally) injected in PSR 1 and PSR 51, and the portion of dilution stream equally injected among PSRs 2 to 50 and PSRs 52 to 100. This particular injection pattern is defined in an auxiliary function present in the functions library file, and can be modified there. Finally the dilution stream does not need to be injected completely in the combustion stream: a potential remainder is mixed with the combustion stream in a ”collector” reactor, after the PFR region. This would constitute the inlet gas of the second flameless combustor of the hybrid combustion chamber.

Bibliography

[1] Enerdata intelligence & consulting. Global energy statistical yearbook, Accessed : 03/11/2015 . URL https://yearbook.enerdata.net/.

[2] H. Tsuji, A. K. Gupta, T. Hasegawa, M. Katsuki, K. Kishimoto, and M. Morita. *High Temperature Air Combustion : from energy conservation to pollution reduction*. CRC Press LLC, 2003.

[3] OECD / IEA. *CO2 emissions from fuel combustion - Highlights*. IEA Statistics. 2014 edition.

[4] Greenhouse Gas Protocol. Global warming potentials, Accessed : 03/11/2015 2015. URL http://ghgprotocol.org/sites/default/files/ghgp/Global-Warming-Potential-Values.pdf.

[5] Danon B. *Furnaces with multiple flameless combustion burners*. Phd thesis, 2011.

[6] AHEAD Europroject. URL http://www.ahead-euproject.eu/home/.

[7] David G. Goodwin Speth, Harry K. Moffat, and Raymond L. Cantera: An object-oriented software toolkit for chemical kinetics, thermodynamics and transport processes, 2015. URL http://www.cantera.org.

[8] G. G. Szegö. *Experimental and Numerical Investigation of a Parallel Jet MILD Combustion Burner System in a Laboratory-scale Furnace*. Phd thesis, 2010.

[9] J. Raub. Carbon monoxide (second edition). Report, World Health Organization (WHO), 1999.

[10] Working Group I IPCC. Climate change 2007 - the physical science basis. Report, Intergovernmental Panel on Climate Change (IPCC), 2007.

[11] R. C. Flagan and J. H. Seifeld. *Fundamentals of Air Pollution Engineering*. Prentice - Hall, 1988.

[12] S. R. Turns. *An Introduction to Combustion - Concepts and Application*. McGraw-Hill, 2000.

[13] Clean Air Technology Center US Environmental Protection Agency (EPA). Nitrogen oxides (NOx): Why and how they are controlled. Report, 1999.

[14] C. T. Bowman. Control of combustion generated nitrogen oxide emissions : Technology driven by regulation, 1992.

[15] Office of Air Quality Planning Agency and Standards US Environmental Protection. NOx: How nitrogen oxides affect the way we live and breathe. Report, 1998.

[16] J. A. Miller and C. T. Bowman. Mechanism and modeling of nitrogen chemistry in combustion. *Progress in Energy and Combustion Science*, 15:287–338, 1989.

[17] Y. B. Zeldovich, D. Frank-Kamenetskii, and P. Sadovnikov. Oxidation of nitrogne in combustion. *Academy of Sciences of the USSR*, 1947.

[18] ANSYS. *ANSYS Fluent Theory Guide*, volume 15.0. ANSYS Inc., 2013.

[19] C. P. Fenimore. Formation of nitric oxide in premixed hydrocarbon flames. *Symposium (International) on Combustion*, pages 373–380, 1971.

[20] D. Lupant. *Caraterisation expérimentale détaillée et modélisation numérique de la combustion diluée du gaz naturel sur une installation de laboratoire de 30kW*. Phd thesis, 2011.

[21] P. C. Malte and D. T. Pratt. Measurement of atomic oxygen and nitrogen oxides in jet-stirred combustion. *Symposium (International) on Combustion*, pages 1061–1070, 1975.

[22] J. W. Bozzelli and Dean A. M. O + NNH: A possible new route for NOx formation in flames. *International Journal of Chemical Kinetics*, 27(11):1097–1109, 1995.

[23] J. E. Harrington, G. P. Smith, P. A. Berg, A. R. Noble, J. B. Jeffries, and D. R. Crosley. Evidence for a new no production mechanism in flames. *26th Symposium (International) on Combustion/The Combustion Institute*, pages 2133–2138, 1996.

[24] A. N. Hayhurst and E. M. Hutchinson. Evidence for a new way of producing no via nnh in fuel-rich flames at atmospheric pressure. *Combustion and Flame*, 114:274–279, 1998.

[25] Reaction Design. CHEMKIN. URL `http://www.reactiondesign.com/products/chemkin/`.

[26] Reaction Design CHEMKIN. Chemical mechanisms data, Accessed: 09/11/2015 . URL `http://www.reactiondesign.com/support/chemical-mechanisms-data/`.

[27] Gas Research Institute. GRI-Mech 3.0, . URL `http://combustion.berkeley.edu/gri-mech/`.

[28] Gas Research Institute. Optimization targets GRI-3.0 mechanism, . URL `http://combustion.berkeley.edu/gri-mech/version30/text30.html#targets`.

[29] Reaction Design. CHEMKIN Tutorials Manual - 10112/15112. 2011.

[30] D. R. Hardesty and F. J. Weinberg. Burners producing large excess enthalpies. *Combustion Science and Technology*, 8:201–214, 1974.

[31] F. J. Weinberg. Heat-recirculating burners: Principles and some recent developments. *Combustion Science and Technology*, 121:3–22, 1996.

[32] J. A. Wünning and J. G. Wünning. Flameless oxidation to reduce thermal NO-formation. *Progress in Energy and Combustion Science*, 23:81–94, 1997.

[33] J. G. Wünning. Flox - Flameless Combustion. *ThermProcess Symposium*, 2003.

[34] A. Cavaliere and M. de Joannon. Mild combustion. *Progress in Energy and Combustion Science*, 30:329–366, 2004.

[35] A. Milani and A. Saponaro. Diluted combustion technologies. *IFRF Combustion Journal - Article number 200101*, 2001.

[36] S. H. Keizer. *Flameless Combustion in a 2x100 kWth furnace: A comparison of experiments with CFD-type simulations*. MSc thesis, 2014.

[37] H. Rodrigues. *Spray combustion in moderate and intense low-oxygen conditions - An experimental study*. Phd thesis, 2015.

[38] S. Kumar, P. J. Paul, and H. S. Mukunda. Studies on a new high-intensity low-emission burner. *Proceedings of the Combustion Institute*, 29:1131–1137, 2002.

[39] M. Lackner, F. Winter, and A. K. Agarwal. *Handbook of Combustion, 5 volumes set*, volume 5 - chap. 13. Wiley Inc., 2010.

[40] T. Plessing, N. Peters, and J. G. Wünning. Laseroptical investigation of highly preheated combustion with strong exhaust gas recirculation. *27th Symposium (I*.

[41] A. A. A. Abuelnor, M. A. Wahid, H. A. Mohammed, and A. Saat. Flameless combustion role in the mitigation of nox emission: a review. *International Journal of Energy Research*, 38(7):827–846, 2014.

[42] R. Weber, A. L. Verlaan, S. Orsino, and N. Lallement. On emerging furnace design methodology that provides substantial energy savings and drastic reductions in CO2, CO and NOx emissions. *Journal of the Institute of Energy*, 72:77–83, 1999.

[43] R. Weber, S. Orsino, N. Lallement, and A. Verlaan. Combustion of natural gas with high-temperature air and large quantities of flue gas. *Proceedings of the Combustion Institute*, 28 (1):1315–1321, 2000.

[44] M. Lackner, F. Winter, and A. K. Agarwal. *Handbook of Combustion, 5 volumes set*, volume 5 - chap. 10. Wiley Inc., 2010.

[45] M. de Joannon, A. Saponaro, and A. Cavaliere. Zero-dimensional analysis of diluted oxidation of methane in rich conditions. *Proceedings of the Combustion Institute*, 28:1639–1646, 2000.

[46] A. F. Colorado, B. A. Herrera, and A. A. Amell. Performance of a flameless combustion furnace using biogas and natural gas. *Bioresource Technology*, 101:2443–2449, 2010.

[47] A. Milani and J. Wünning. What is flameless combustion? *IFRF Combustion File n°171*, 2002.

[48] A. G. Rao and Y. Levy. A new combustion methodology for low emission gas turbine engines. *8th HiTACG Conference - Poznan*, 2010.

[49] Y. He. *Flameless Combustion of Natural Gas in the SJ/WJ Furnace*. Phd thesis, 2008.

[50] S. B. Pope. *Turbulent Flows*. Cambridge University Press, 2000.

[51] H. A. Becker, H. C. Hottel, and G. C. Williams. The nozzle-fluid concentration field of the round, turbulent, free jet. *Journal of Fluid Mechanics*, 30:285–303, 1967.

[52] E. W. Grandmaison, D. E. Rathgeber, and H. A. Becker. Some characteristics of concentration fluctuations in free turbulent jets. *The Canadian Journal of Chemical Engineering*, 60:212–219, 1982.

[53] F. P. Ricou and D. B. Spalding. Measurements of entrainment by axisymmetrical turbulent jets. *Journal of Fluid Mechanics*, 11:21–32, 1961.

[54] B. J. Hill. Measurement of local entrainment rate in the initial region of axisymmetric turbulent air jets. *Journal of Fluid Mechanics*, 51:773–779, 1972.

[55] D. Han and M. G. Mungal. Direct measurements of entrainment in reacting/nonreacting turbulent jets. *Combustion and Flame*, 124:370–386, 2001.

[56] M. Ayoub. *Etude de l'Extension du Régime de Combustion Sans Flamme aux Mélanges Méthane/Hydrogène et aux Environnements à Basse Température*. Phd thesis dissertation, 2013.

[57] E. Oldenhof. *Autoignition and flame stabilisation processes in turbulent non-premixed hot coflow flames*. Phd thesis, 2012.

[58] B. B. Dally, A. N. Karpetis, and R. S. Barlow. Structure of turbulent non-premixed jet flames in a diluted hot coflow. *Proceedings of the Combustion Institute*, 29:1147–1154, 2002.

[59] T. Fujimori, D. Riechelmann, and J. Sato. Effect of liftoff on nox emission of turbulent jet flame in high-temperature coflowing air. *27th Symposium (International) on Combustion/The Combustion Institute*, pages 1149–1155, 1998.

[60] J. E. Broadwell and A. E. Lutz. A turbulent jet chemical reaction model: NOx production in jet flames. *Combustion and Flame*, 114:319–335, 1998.

[61] M. Lackner, F. Winter, and A. K. Agarwal. *Handbook of Combustion, 5 volumes set*, volume 3 - chap. 5. Wiley Inc., 2010.

[62] M. Mancini, P. Schwöppe, R. Weber, and S. Orsino. On mathematical modelling of flameless combustion. *Combustion and Flame*, 150:54–59, 2007.

[63] M. Mancini, R. Weber, and U. Bollettini. Predicting nox emissions of a burner operated in flameless oxidation mode. *Proceedings of the Combustion Institute*, 29:1155–1163, 2002.

[64] E. W. Grandmaison, I. Yimer, H. A. Becker, and A. Sobiesiak. The strong-jet/weak-jet problem and aerodynamic modeling of the cgri burner. *Combustion and Flame*, 114:381–396, 1998.

[65] I. Yimer, H. A. Becker, and E. W. Grandmaison. The strong-jet/weak-jet problem: New experiments and cfd. *Combustion and Flame*, 124:481–502, 2001.

[66] J. Mi, P. Li, and C. Zheng. Impact of injection conditions on flame characteristics from a parallel multi-jet burner. *Energy*, 36:6583–6595, 2011.

[67] J. Mi, F. Wang, P. Li, and B. B. Dally. Modified vitiation in a moderate or intense low-oxygen dilution (mild) combustion furnace. *Energy and Fuels*, 26:265–277, 2012.

[68] G. G. Szegö, B. B. Dally, and G. J. Nathan. Scaling of nox emissions from a laboratory-scale mild combustion furnace. *Combustion and Flame*, 154:281–295, 2008.

[69] G. G. Szegö, B. B. Dally, and G. J. Nathan. Operational characteristics of a parallel jet mild combustion burner system. *Combustion and Flame*, 156:429–438, 2009.

[70] Y. J. Lee. *Mathematical modeling of nonpremixed turbulent methane-air flameless combustion in a strong-jet/weak-jet burner*. Phd thesis, 2010.

[71] E. Faghani and S. N. Rogak. A phenomenological model of two circular turbulent jets. *International Journal of Engine Research*, 14(3):293–304, 2012.

[72] M. Mancini. *Analysis of mild combustion of Natural Gas with preheated air*. Phd thesis, 2006.

[73] I. Yimer, H. A. Becker, and E. W. Grandmaison. Develoment of flow from multiple-jet burners. *The Canadian Journal of Chemical Engineering*, 74:840–851, 1996.

[74] A. G. Rao and A. Bhat. Hybrid combustion system for future aero engines. In *Proceedings of the 2nd National Propulsion Conference*.

[75] A. G. Rao, F. Yin, and J. P. van Buijtenen. A novel hybrid engine concept for aircraft propulsion. *Proceedings of the XXth International Symposium on Air Breathing Engines (ISABE)*, 2011.

[76] T. G. Reichel, S. Terhaar, and C. O. Paschereit. Flow field manipulation by axial air injection to achieve flashback resistance and its impact on mixing quality. *43rd Fluid Dynamics Conference*, 2013.

[77] T. G. Reichel, K. Goeckeler, and C. O. Paschereit. Investigation of lean premixed swirl-stabilized hydrogen burner with axial air injection using oh-plif imaging. *Proceedings of the ASME Turbo Expo 2015: Turbine Technical Conference and Exposition*, 2015.

[78] S. Terhaar, T. G. Reichel, C. Schrödinger, L. Rukes, C. O. Paschereit, and K. Oberleithner. Vortex breakdown types and global modes in swirling combustor flows with axial injection. *Journal of Propulsion and Power*, 31(1):219–229, 2014.

[79] AHEAD consortium. Presentation of the AHEAD project at the ILA Berlin Air Show, 2014. URL `http://www.ahead-euproject.eu/dissemination/category/presentations-4/`.

[80] A. Bhat and A. G. Rao. Prediction of emissions from AHEAD engine variants using detailed chemistry and reaction models. *AHEAD Deliverable 2.1 - Annex*, 2012.

[81] T. G. Reichel and S. Göke. Presentation - AHEAD WP2: Dual-hybrid combustion system, hydrogen combustion. 2012.

[82] A. A. Konnov, G. Colson, and J. De Ruyck. NO formation rates for hydrogen combustion in stirred reactors. *Fuel*, 80:49–65, 2001.